

In-situ Micro-Spectroscopy on Coke Formation Processes in Zeolites

Vorming van coke in zeolieten gevisualiseerd met tijds- en
plaatsafhankelijke micro-spectroscopie tijdens reactie

(met een samenvatting in het Nederlands)

Proefschrift

ter verkrijging van de graad van doctor aan de Universiteit Utrecht op gezag
van de rector magnificus, prof. dr. G.J. van der Zwaan, ingevolge het besluit
van het college voor promoties in het openbaar te verdedigen op woensdag
14 december 2011 des ochtends te 10.30 uur

door

Davide Mores

geboren op 25 april 1982 te Pordenone, Italië.

Promotor: Prof. dr. ir. B.M. Weckhuysen

This PhD thesis was accomplished with financial support from de Nederlandse Organisatie voor Wetenschappelijk Onderzoek (NWO) in the form of a TOP-CW grant.

A mio padre

I cui insegnamenti, forza ed incoraggiamenti mi hanno formato

A mia madre

Le cui preghiere ed amore mi hanno confortato

A i miei fratelli e sorelle

Per il loro affetto e sostegno

ISBN: 978-90-8891-333-4

Published by: Uitgeverij BOXPress BV, Oisterwijk

Printed by: Proefschriftmaken.nl

Table of Contents

Chapter 1	General Introduction	7
Chapter 2	Coke Formation during the Methanol-to-Olefin Conversion over H-ZSM-5 and H-SAPO-34 Molecular Sieves: Influence of the Framework Topology	17
Chapter 3	Coke Formation during the Methanol-to-Olefin Conversion over H-ZSM-5 Molecular Sieves: Influence of the Silicon-to-Aluminum Ratio	37
Chapter 4	Catalytic Performance of Micron-sized H-ZSM-5 Zeolite Crystals during Methanol-to-Olefin Conversion: Bridging the Gap between Single Particle Examination and Bulk Catalyst Analysis	61
Chapter 5	Coke Formation during Paraffin and Olefin Aromatization over H-ZSM-5 Molecular Sieves: Spatial and Temporal Mapping of Coke within Individual Zeolite Crystals	77
Chapter 6	Catalyst Deactivation of Core-Shell H-ZSM-5/Silicalite-1 Composites as studied at the Individual Particle Level	97
Chapter 7	Etherification of Biomass-Based Polyols with Alkenes over H-Beta Zeolites: Spatial and Temporal Mapping of Coke within Individual Zeolite Catalysts	119
Chapter 8	A: Summary and Future Perspectives B: Samenvatting in het Nederlands	137 143
List of Publications		149
Acknowledgements		153
About the Author		157

Chapter 1

General Introduction

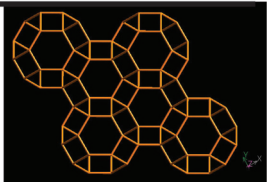
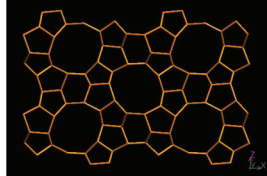
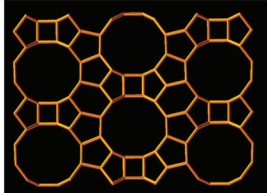
Catalysis dates back to the dawn of civilization when mankind began to produce wine and beer by fermentation, although little effort was made to explain the events taking place. In 1835, Jöns Jacob Berzelius coined the name catalysis with the statement that a “catalytic force” was operative.^[1-3] Since then, catalysts have taken an ever increasing role in the production of food, pharmaceuticals, chemicals and fuels. Presently, around 85% of all chemical processes require a catalyst. The role of a catalyst is to facilitate a chemical conversion by lowering the activation energy barrier of the reaction. By doing so, an increase in efficiency and selectivity can be achieved. Today, three catalyst types are distinguished: heterogeneous, homogeneous and biocatalysts. Heterogeneous catalysts are the most widely applied industrially and with the ever growing demand of chemicals, diminishing fossil resources and tightening environmental legislation, the demand for novel and improved catalysts is expected to steadily increase.^[4]

1.1 Molecular Sieves

Within the group of heterogeneous catalysts, zeolites play an important role. These solid materials mainly consist of silicon, aluminum, oxygen and charge compensating cations. Most zeolite structures contain AlO_4 and SiO_4 tetrahedral primary building units. These entities can connect into secondary structural components through the linkage with a common oxygen ion. Assemblage of these secondary units composes the final zeolite framework architecture. Depending on the synthesis characteristics, distinct highly ordered framework topologies can be achieved in which four main pore groups are distinguished: small pores (eight-ring pores with 3-4.5 Å free diameter), medium pores (ten-ring pores with 4.5-6 Å free diameter), large pores (twelve-ring pores with 6-8 Å free diameter) and ultra large pores (> twelve-ring pores). This well-defined porous architecture allows unique molecular size and shape selectivity.^[4-6] Furthermore, the charge difference between Si (4+) and Al (3+), results in a net negative charge of the overall pore-network. This difference is neutralized by exchangeable cations that result in Brønsted acidity when the compensating charge is provided by a proton.^[7] The presence of acid sites, the noted molecular size and shape selectivity, high surface area and thermal stability make these materials highly suited for acid catalyzed reactions, which is mirrored in their widespread industrial application.^[4, 7, 8]

Nowadays, approximately 200 different zeolite types are known. The zeolite materials discussed in this PhD thesis are SAPO-34 (CHA), ZSM-5 (MFI) and zeolite Beta (BEA). Their properties are summarized in Table 1.1.

Table 1.1: Properties of the zeolite materials studied in this PhD thesis.^[9]

Zeolite	Channels (Å)	Pore System	Framework
SAPO-34	4.2 x 3.7 (8-ring) 6.5 x 11 (cage)	CHA (3D)	
ZSM-5	5.1 x 5.5 (10-ring) 5.3 x 5.6 (10-ring) 9.4 (intersection)	MFI (2D)	
Beta	7.6 x 6.4 (12-ring) 5.5 x 5.5 (10-ring) 10 (intersection)	BEA (3D)	

1.2 Zeolite Catalysts: Towards Oil-alternative Feedstocks

Zeolites are extensively applied in petrochemical conversions. The production of oil-based products however poses challenges as growing economic activity, stringent environmental legislation and finite availability of the crude are conflicting. As a consequence, emerging technologies that utilize oil-alternative feedstocks are gaining interest with a noted role for zeolite catalysts.^[10-13] One rising technology is the so-called Gas-to-Liquids (GTL) process. GTL refers to technologies that are designed to convert small gaseous hydrocarbons into long-chain hydrocarbons, as alternative to the traditional oil refining. Biomass, natural gas and coal are carbon-containing resources and therefore potential substitutes of crude oil. These feedstocks can, for example, be converted into synthesis gas, a mixture of carbon monoxide and hydrogen. From this mixture, a variety of short- and long-chain hydrocarbons can be synthesized.^[14-16]

The conversion of synthesis gas into methanol is well-known and the easy-to-handle compound is a conventional chemical that can be further transformed into valuable hydrocarbons.^[12, 14, 15] The Methanol-to-Hydrocarbon (MTH) process occurs over zeolite catalysts and depending on catalyst choice and applied reaction conditions one can alter the product selectivity. Part of this PhD thesis deals with this GTL-branch and investigates more in particular

the promising Methanol-to-Olefin (MTO) conversion. The pre-conversions of the oil-alternative feedstocks towards synthesis gas and methanol, prior to the actual desired chemical transformation, offers exceptional flexibility as both feedstock and final product can be varied. The intermediate steps can however suppress the overall process efficiency. Circumvention of these pre-conversions by the direct transformation of the novel feedstock into desired products is consequently attractive. Biomass in particular can serve as a more direct carbon source.^[17-19] However, compared to previous mentioned routes, this material contains a larger variety of functional groups. This change in the chemical nature of the feedstock may give rise to new requirements on the applied zeolite catalyst and this topic is also explored in this PhD thesis. The development of novel analytical tools can furthermore be applied on existing technologies, thereby offering new insights that can lead to the improvement of current processes.^[20-22]

1.3 Zeolite Deactivation Induced by Coke Formation

Requirements for a good catalyst are high activity, excellent selectivity and extended stability. These properties can change during the course of reaction. Particularly in hydrocarbon processing, the formation of undesired coke deposits is usually inevitable. These coke residues can affect the catalyst performance, thereby provoking variations in activity and/or selectivity. Coke is generally defined as “*carbonaceous deposits that are mainly deficient in hydrogen compared to the coke-forming reactant molecules and responsible for catalyst deactivation*”.^[5, 23, 24] The nature of coke deposits varies from olefinic or paraffinic hydrocarbons up to graphite-like matter.

Both the formation and the chemical nature of these side-products strongly depend on parameters, such as reactant composition, reaction conditions, catalyst properties, location of the carbonaceous deposition and coke build-up rate. The steric constraints that are imposed by the well-defined zeolite framework architecture, provide a spatial confinement that can influence the deposition of undesired coke material. Here, large carbonaceous by-products can cause pore blockage, thereby physically preventing the access of reactants and the exit of formed reaction products. Additionally, these retained hydrocarbons can occupy the catalytic active sites, thereby poisoning the catalyst and restricting reactant transformation.^[25-27] Mild reaction conditions generally produce coke type I, which consists of low-molecular hydrogen-rich molecules. Large poly-cyclic hydrogen-deficient aromatics (coke type II) on the other hand, usually form under more severe reaction conditions. The determination of the H/C ratio of carbonaceous deposits is therefore a first

analytical indicator. Besides an increasing reaction temperature, a decline of the H/C ratio also occurs with progressing reaction time. This phenomenon is known as “aging of coke” and is illustrative of the dynamic process of coke formation.^[26-35]

The number of studies that investigate the nature of coke deposits and their formation mechanisms has greatly expanded in the past decades. Their purpose is to find efficient methods to prevent or alleviate the unfavorable catalyst deactivation and a variety of analytical tools is thereby utilized. Among these techniques, infrared (IR), ultraviolet-visible (UV-Vis), electron spin resonance (ESR), nuclear magnetic resonance (NMR), gravimetric (TEOM, TGA) and X-ray photoelectron spectroscopy (XPS) have been applied.^[36-39] The number of methods that allows the investigation of the coke formation under realistic reaction conditions is however limited and even further diminishes when non-invasive methods or spatial resolution criteria are requested. For this, in-situ characterization techniques have drawn the attention with the expectation to obtain new insights into the coke growth mechanisms in a working catalyst.^[40-42]

1.4 Chemical Imaging of Catalytic Events

In order to develop new and improved catalysts, a detailed understanding of the catalytic system is essential. To reach this goal, many efforts are made to unravel the nature of the catalytic active sites, elucidate reaction mechanisms and correlate the structure-function relationship of a catalytic material. The use of spectroscopic characterization techniques has thereby become an important tool.^[40-42] Conventional spectroscopic studies generally focus on an ensemble of sample, thereby averaging information. These techniques are normally applied in a static mode where the sample is analyzed outside the chemical environment. Valuable information can be obtained from these efforts. However, as catalytic processes occur under dynamic conditions, intrinsic knowledge on the behavior of a catalyst during the course of the reaction is desirable. For this, the use of in-situ spectroscopic techniques can be of assistance.^[40-42]

In-situ analytical tools allow real-time monitoring of a catalytic process under realistic working conditions, such as elevated temperature and pressure. In the past decade, the development of in-situ spectroscopic instrumentation has furthermore been directed towards the combined use of different spectroscopic techniques on one catalytic system. With this approach, a more comprehensive understanding of the catalyst at work can be provided. As in the case of conventional spectroscopy however, the majority of these

techniques are used on bulk systems, thereby assuming a somewhat homogeneous catalytic event. In catalysis, spatial gradients are generally a rule rather than an exception. Variations occur on many different length scales, from an industrial reactor down to the atomic scale of a catalytic active site.^[43-45] Therefore, further progress resulted in the development of in-situ micro-spectroscopic techniques that allow an additional spatial dimension to the measurements.^[40] The majority of the work described in this PhD thesis uses spatiotemporal characterization techniques with micrometer resolution. The main techniques employed are UV-Vis micro-spectroscopy and confocal fluorescence microscopy. Both experimental set-ups are schematically illustrated in Figure 1.1.

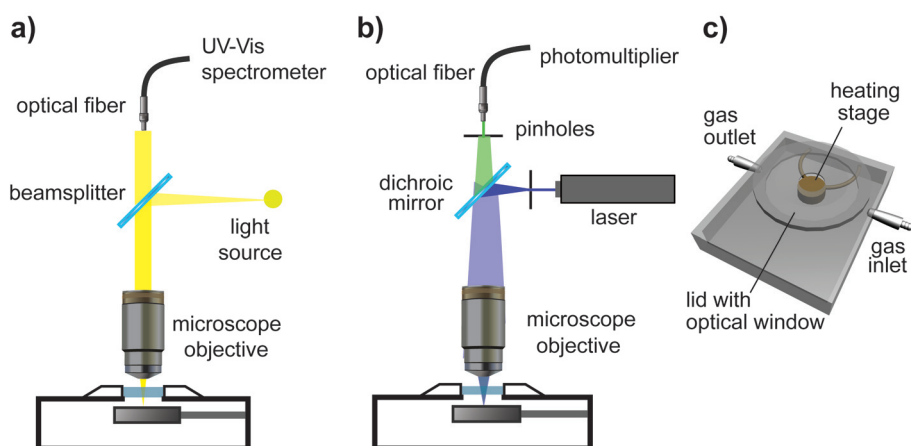


Figure 1.1: Schematic representation of (a) a UV-Vis micro-spectroscopy set-up, (b) a confocal fluorescence microscopy set-up and (c) an in-situ reactor cell.^[46]

The catalytic events under investigation take place in the in-situ cell (Figure 1.1c), that consists of a closed reactor cell equipped with a heating stage. The catalyst sample is placed on this heating element that allows carrying out the reaction at a desired reaction temperature, while an optical window permits the temporal track of the catalytic event. The construction of the cell allows the use of gaseous and fluid reactants and the cell can be placed under both the UV-Vis as well as the fluorescence microscope systems, which are in an upright configuration.^[46]

In the case of the optical microscopic set-up (Figure 1.1a), light is focused on the sample using a high numerical aperture objective lens and the reflected light is collected back by the objective lens where it is directed to the CCD-camera and/or to the CCD UV-Vis spectrometer connected with an optical fiber. The introduction of a rotatable polarizer between the objective lens and

the detector allows the separation of a desirable light polarization, and the system permits time- and space-resolved optical absorption measurements with micrometer dimension resolution. Light emission can accordingly be monitored by means of fluorescence microscopy (Figure 1.1b). Placement of a pinhole in the optical pathway eliminates out of focus light. This allows the additional detection in the vertical axis of the sample and permits examination of the spatial distribution of fluorescent species in three-dimensions.^[46-58]

1.5 Scope and Outline of the PhD Thesis

The work described in this PhD thesis applies micro-spectroscopic techniques to study the formation of carbonaceous deposits in a spatiotemporal manner at the individual catalyst particle level. The use of micron-sized crystalline zeolites as model catalysts, enables featuring heterogeneities that are larger than the diffraction limit of the applied detection techniques.

Chapter 2 examines the influence of the zeolite framework topology on the coke formation process that occurs during the Methanol-to-Olefin (MTO) conversion. The combination of UV-Vis and confocal fluorescence microscopy indicates differences in the nature and formation-mode of carbonaceous deposits between the MFI and CHA structure. Further elaboration of this work is described in **Chapter 3**, where the influence of the Brønsted acid site density on the coke growth process is investigated. The application of separate excitation wavelengths in confocal fluorescence microscopy combined with the use of polarization dependent UV-Vis micro-spectroscopy allows denoting how coke deposits, differing in their molecular dimensions, are located within H-ZSM-5 zeolite crystals. **Chapter 4** outlines the activity and selectivity characteristics of large micron-sized H-ZSM-5 zeolites during the MTO conversion. The in-situ examination at the individual particle level is hereby compared with bulk analysis in a fixed-bed reactor. The retained coke material as well as the regeneration properties of these large molecular sieves is analyzed by means of UV-Vis and GC-MS. **Chapter 5** expands the use of the micro-spectroscopic analytical tools to study the coke formation that occurs during the conversion of Light-Cracked-Naphtha (LNA) derivatives. The location and nature of these carbonaceous deposits is investigated in a comparative study between olefinic and paraffinic hydrocarbon reactants. The influence of reactant chain length and methyl branching is visualized within individual H-ZSM-5 zeolite crystals. **Chapter 6** examines the effect of an external crystalline silicalite-1 shell that covers the catalytically active H-ZSM-5 zeolite. The coke formation process that occurs during both the MTO and the LNA conversions is thereby explored. **Chapter 7** applies the

micro-spectroscopic techniques to the field of biomass conversion. The etherification of biomass-based polyols with long linear alkenes is imaged on micron-sized zeolite Beta crystals at the individual particle level and indicates how the physicochemical properties of the reactants influence the formation of coke products. Finally, **Chapter 8** summarizes the conclusions described in this PhD thesis and finishes with some thoughts for future research.

References

- [1] J.J. Berzelius, *Årsberättelsen om framsteg i fysic och kemi*, Royal Swedisch Academy of Sciences, **1835**.
- [2] J.J. Berzelius, *Reseantechningar*, P.A. Norstedt & Söner, Stockholm, **1903**.
- [3] B. Lindstrom, *Cattech*. **2003**, 7, 130-138.
- [4] R.A. van Santen, P.W.N.M. van Leeuwen, J.A. Moulijn, B.A. Averil (Eds.), *Catalysis an Integrated Approach*, Elsevier, Amsterdam, **2000**.
- [5] H. van Bekkum, E.M. Flanigen, P.A. Jacobs, J.C. Jansen (Eds.), *Introduction to Zeolite Science and Practice*, Elsevier, Amsterdam, **2001**.
- [6] C. Baerlocher, W.M. Meier, D.H. Olson (Eds.), *Atlas of Zeolite Framework Types*, Elsevier, Amsterdam, **2001**.
- [7] G. Busca, *Chem. Rev.* **2007**, 107, 5366-5410.
- [8] A. Corma, *Chem. Rev.* **1995**, 95, 559-614.
- [9] www.iza-structure.org/database.
- [10] T. P. Vispute, H. Y. Zhang, A. Sanna, R. Xiao, G. W. Huber, *Science* **2010**, 330, 1222-1227.
- [11] M. Stöcker, *Microporous Mesoporous Mater.* **1999**, 29, 3-48.
- [12] G. A. Olah, *Angew. Chem. Int. Ed.* **2005**, 44, 2636-2639.
- [13] G. E. Keller, M. M. Bhasin, *J. Catal.* **1982**, 73, 9-19.
- [14] T. Mokrani, M. Scurrrell, *Catal. Rev. Sci. Eng.* **2009**, 51, 1-145.
- [15] C. Okkerse, H. van Bekkum, *Green Chem.* **1999**, 1, 107-114.
- [16] O. L. Eliseev, *Russian J. Gen. Chem.* **2009**, 79, 2509-2519.
- [17] J. N. Chheda, J. A. Dumesic, *Catal. Today* **2007**, 123, 59-70.
- [18] J. N. Chheda, G. W. Huber, J. A. Dumesic, *Angew. Chem. Int. Ed.* **2007**, 46, 7164-7183
- [19] J. N. Chheda, Y. Roman-Leshkov, J. A. Dumesic, *Green Chem.* **2007**, 9, 342-350.
- [20] H. Y. Long, X. S. Wang, W. F. Sun, *Microporous Mesoporous Mater.* **2009**, 119, 18-22.
- [21] Z. Musilova, N. Zilkova, S. E. Park, J. Cejka, *Top. Catal.* **2010**, 53, 1457-1469.
- [22] R. J. J. Nel, A. de Klerk, *Ind. Eng. Chem. Res.* **2007**, 46, 2902-2906.
- [23] H. van Bekkum, F. Bauer (Eds.), *Molecular Sieves*, Springer-Verlag, Berlin Heidelberg, **2007**.
- [24] G. F. Froment, J. Demeyer, E. G. Derouane, *J. Catal.* **1990**, 124, 391-400.
- [25] R.K. Graselli, A.W. Sleight (Eds.), *Structure-Activity and Selectivity Relationships in Heterogeneous Catalysis*, Elsevier, Amsterdam, **1990**.

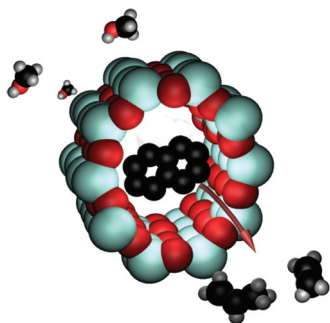
- [26] L. D. Rollmann, D. E. Walsh, *J. Catal.* **1979**, *56*, 139-140.
- [27] M. A. Uguina, D. P. Serrano, R. Vangrieken, S. Venes, *Appl. Catal. A* **1993**, *99*, 97-113.
- [28] H. Schulz, *Catal. Today* **2010**, *154*, 183-194.
- [29] H. Schulz, K. Lau, M. Claeys, *Appl. Catal. A* **1995**, *132*, 29-40.
- [30] G. F. Froment, *Appl. Catal. A* **2001**, *212*, 117-128.
- [31] G. F. Froment, *Catal. Rev. Sci. Eng.* **2008**, *50*, 1-18.
- [32] P. Magnoux, H. S. Cerqueira, M. Guisnet, *Appl. Catal. A* **2002**, *235*, 93-99.
- [33] M. Guisnet, P. Magnoux, *Appl. Catal.* **1989**, *54*, 1-27.
- [34] I. Kiricsi, H. Forster, G. Tasi, J. B. Nagy, *Chem. Rev.* **1999**, *99*, 2085-2114.
- [35] J. M. Lopes, F. Lemos, F. R. Ribeiro, E. G. Derouane, P. Magnoux, M. Guisnet, *Appl. Catal. A* **1994**, *114*, 161-172.
- [36] E. E. Wolf, F. Alfani, *Catal. Rev. Sci. Eng.* **1982**, *24*, 329-371.
- [37] S. Bhatia, J. Beltramini, D. D. Do, *Catal. Rev. Sci. Eng.* **1989**, *31*, 431-480.
- [38] M. Guisnet, P. Magnoux, *Appl. Catal. A* **2001**, *212*, 83-96.
- [39] M. Guisnet, L. Costa, F. R. Ribeiro, *J. Mol. Catal. A* **2009**, *305*, 69-83.
- [40] B. M. Weckhuysen, *Angew. Chem. Int. Ed.* **2009**, *48*, 4910-4943.
- [41] B.M. Weckhuysen (Ed.), *In-Situ Spectroscopy of Catalysts*, American Scientific Publishers, Stevenson Ranch, **2004**.
- [42] J.W. Niemantsverdriet (Ed.), *Spectroscopy in Catalysis: An Introduction*, VCH, Weinheim, **2007**.
- [43] C. Coperet, R. van Santen, *Dalton Trans.* **2010**, *39*, 8354-8354.
- [44] C. J. Dittrich, S. M. P. Mutsers, *Chem. Eng. Sci.* **2007**, *62*, 5777-5793.
- [45] W. F. Paxton, S. Sundararajan, T. E. Mallouk, A. Sen, *Angew. Chem. Int. Ed.* **2006**, *45*, 5420-5429.
- [46] E. Stavitski, M. H. F. Kox, B. M. Weckhuysen, *Chem. Eur. J.* **2007**, *13*, 7057-7065.
- [47] E. Stavitski, M. H. F. Kox, I. Swart, F. M. F. de Groot, B. M. Weckhuysen, *Angew. Chem. Int. Ed.* **2008**, *47*, 3543-3547.
- [48] E. Stavitski, M. R. Drury, D. A. M. de Winter, M. H. F. Kox, B. M. Weckhuysen, *Angew. Chem. Int. Ed.* **2008**, *47*, 5637-5640.
- [49] G. Spoto, F. Geobaldo, S. Bordiga, C. Lamberti, D. Scarano, A. Zecchina, *Top. Catal.* **1999**, *8*, 279-292.
- [50] M. H. F. Kox, E. Stavitski, B. M. Weckhuysen, *Angew. Chem. Int. Ed.* **2007**, *46*, 3652-3655.
- [51] M. H. F. Kox, E. Stavitski, J. C. Groen, J. Perez-Ramirez, F. Kapteijn, B. M. Weckhuysen, *Chem. Eur. J.* **2008**, *14*, 1718-1725.
- [52] M. H. F. Kox, A. Mijovilovich, J. J. H. B. Sattler, E. Stavitski, B. M. Weckhuysen, *ChemCatChem.* **2010**, *2*, 564-571.
- [53] F. Marlow, K. Hoffmann, G. G. Lindner, I. Girnus, G. van de Goor, J. Kornatowski, J. Caro, *Micropor. Mater.* **1996**, *6*, 43-49.
- [54] I. Kiricsi, G. Tasi, H. Forster, P. Fejes, *J. Mol. Struct.* **1990**, *218*, 369-374.
- [55] L. Karwacki, E. Stavitski, M. H. F. Kox, J. Kornatowski, B. M. Weckhuysen, *Angew. Chem. Int. Ed.* **2007**, *46*, 7228-7231.

- [56] L. Karwacki, M. H. F. Kox, D. A. M. de Winter, M. R. Drury, J. D. Meeldijk, E. Stavitski, W. Schmidt, M. Mertens, P. Cubillas, N. John, A. Chan, N. Kahn, S. R. Bare, M. Anderson, J. Kornatowski, B. M. Weckhuysen, *Nature Mater.* **2009**, *8*, 959-965.
- [57] L. Karwacki, H. E. van der Bij, J. Kornatowski, P. Cubillas, M. R. Drury, D. A. M. de Winter, M. W. Anderson, B. M. Weckhuysen, *Angew. Chem. Int. Ed.* **2010**, *49*, 6790-6794.
- [58] G. De Cremer, B. F. Sels, D. E. De Vos, J. Hofkens, M. B. J. Roefsaers, *Chem. Soc. Rev.* **2010**, *39*, 4703-4717.

Chapter 2

Coke Formation during the Methanol-to-Olefin Conversion over H-ZSM-5 and H-SAPO-34 Molecular Sieves

Influence of the Framework Topology



The formation of carbonaceous species during the Methanol-to-Olefin conversion is investigated with in-situ optical and confocal fluorescence micro-spectroscopy. Spatial and temporal differences are observed in a comparative study between H-ZSM-5 and H-SAPO-34 zeolite crystals. These variations indicate the influence of the catalyst framework topology.

2.1 Introduction

Olefins are important petrochemical intermediates. Today, most light olefins are obtained from the thermal cracking of naphtha, which is a costly and energy consuming process.^[1-3] The increasing demand for oil-based products and the finite availability of crude oil, demand for alternative production routes that utilize other feedstocks. Methanol is regarded as such alternative raw material as it can be produced from synthesis gas, a mixture of CO and H₂, which in turn, can be made from biomass, natural gas or coal.^[4-6]

The transformation of methanol into hydrocarbons (MTH) was discovered in the 1970s and initially regarded as a powerful way to convert coal into high-octane gasoline.^[7, 8] Succeeding research activities indicated that catalyst choice and applied process conditions alter product selectivity and a variety of hydrocarbons could be obtained from methanol. Today, the MTH process is branched into two main groups (Figure 2.1). These are the Methanol-to-Gasoline (MTG) and Methanol-to-Olefin (MTO) process, where light olefins are the main formed products.^[4, 9-12]

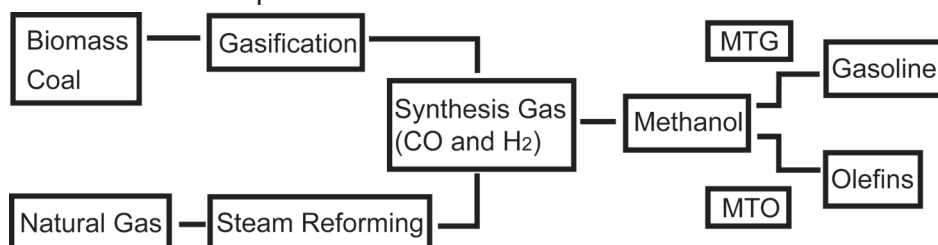


Figure 2.1: Schematic Illustration of the production scheme for the fabrication of olefins from oil alternative feedstocks.^[4]

The MTG reaction was first commercialized by Mobil Oil in 1986 using MFI catalysts.^[4, 8] Improvement of this conversion followed shortly thereafter with the Topsøe integrated gasoline synthesis (TIGAS) process. Here, methanol synthesis and gasoline production were integrated in one loop.^[12] Up to now, two additional technologies have been developed. One is the Norsk Hydro/UOP MTO process that, based on CHA catalysts, yields a flexible mixture of ethene and propene. The second is the Lurgi's process which, based on MFI catalysts, mainly produces propene with some additional gasoline as by-product.^[9, 13]

The MTO reaction has been intensively investigated over the past three decades and the precise reaction mechanism was thereby a strongly debated issue. A major breakthrough came in 1993 with the proposal that an indirect reaction cycle, commonly known as hydrocarbon pool mechanism (HCP), was responsible for the hydrocarbon transformation.^[14-32] This HCP

process involves a series of steps in which the so-called hydrocarbon pool scaffold, a catalytic intermediate constituted of methylated aromatics, closely interacts with the zeolite framework. To these organic-inorganic hybrids, methanol is added. The confined aromatics are alkylated and in a series of rearrangements, the elimination of alkyl side chains produces the desired light alkenes while the remaining lower alkyl substituted aromatics rapidly re-methylate in a closed catalytic cycle. The HCP mechanism is schematically illustrated in Figure 2.2.

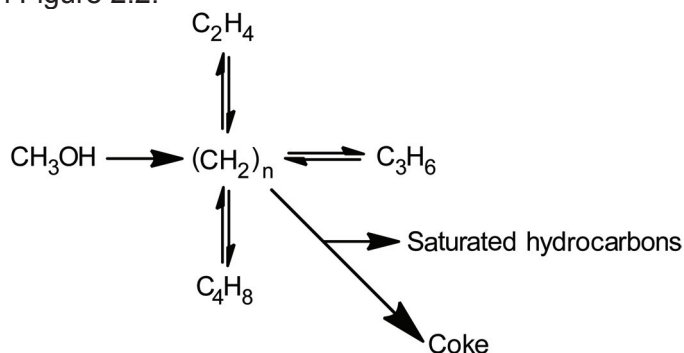


Figure 2.2: Schematic illustration of the hydrocarbon pool mechanism.^[33]

The most promising catalysts for the MTO reaction are H-SAPO-34 and H-ZSM-5 zeolite.^[4] The acidic centres of these materials are responsible for the chemical transformation of methanol into valuable hydrocarbons, while their pore architecture offers well defined confined spaces that provide the desired product shape selectivity.^[34-38] The zeolite framework architecture also influences the size and shape of the HCP scaffold. As described in Chapter 1, H-ZSM-5 has the MFI type structure composed of straight channels (0.51 nm × 0.54 nm) and intersecting smaller sinusoidal pores (0.54 nm × 0.56 nm). H-SAPO-34 molecular sieves on the other hand have a CHA type structure, containing large cavities (0.65 nm × 1.1 nm) connected through narrow windows (0.42 nm × 0.37 nm).^[39, 40] In H-SAPO-34, the alkenes are reckoned to mainly split off from highly methyl-substituted aromatics, such as hexamethylbenzene (hexaMB) and heptamethylbenzene (heptaMB⁺). In H-ZSM-5, lower methylbenzenes, such as xylenes and trimethylbenzenes (TMB), are the main active intermediates.^[14, 24, 28, 31, 41-44]

Figure 2.2 illustrates how besides splitting-off the desired olefins, these organic intermediates can also react further and secondary reactions generate undesired hydrocarbons.^[45-48] These compounds are undesired as they may adsorb on the zeolite acid sites, thereby poisoning the catalyst active centres. The growth of large coke molecules can additionally lead

to pore blocking, which physically restricts the access of reactants towards the catalytic scaffold and the exit of formed products.^[49-52] Pore blocking in H-ZSM-5 zeolites has been related to the formation of poly-aromatic compounds that can be retained both inside the zeolite as well as on the outer surface. In H-SAPO-34, pore blockage predominantly arises from poly-aromatic molecules located in the large cages of the crystal.^[52-56] Both poisoning and pore blocking eventually lead to catalyst deactivation and affect the potential application of these catalysts on an industrial scale.^[57-61] This Chapter examines the coke formation process during the MTO reaction between H-ZSM-5 and H-SAPO-34 molecular sieves. Large zeolite crystals are employed as model systems to image differences in a space- and time-resolved manner.

2.2 Experimental

2.2.1 Methods

UV-Vis micro-spectroscopy

In-situ optical absorption measurements are performed on an Olympus BX41 upright research microscope, as described in Chapter 1.^[62] The device is equipped with a 50x0.5 NA-high working distance objective and a 75 W tungsten lamp provides the illumination. The set-up additionally contains a 50/50 double viewport tube that accommodates a CCD video camera (ColorView Illu, Soft Imaging System GmbH) and an optical fiber mount. A 200 μm -core fiber connects the microscope to a CCD UV/Vis spectrometer (AvaSpec-2048TEC, Avantes).

Confocal fluorescence microscopy

In-situ confocal fluorescence experiments are performed on a Nikon Eclipse LV150 upright microscope equipped with a 50x0.55 NA dry objective.^[62] The images were collected with the use of a Nikon D-Eclipse C1 head connected to laser light sources at 488 and 561 nm. The emission was detected with two photomultiplier tubes in the 510-550 and 575-635 nm range.

In-situ cell

All experiments were performed in an in-situ cell (Linkam FTIR 600) equipped with a temperature controller (Linkam TMS 93).^[62] The crystals were heated to 773 K at the rate of 10 $\text{K}\cdot\text{min}^{-1}$ and kept at this temperature for 1 h under inert atmosphere in order to remove retained water. Subsequently, the temperature was brought to the required reaction temperature, in the range of 530-745 K, at the rate of 10 $\text{K}\cdot\text{min}^{-1}$ after which the N_2 flow was diverted through a bubbler containing methanol, thereby acting as carrier gas.

Gas chromatography – mass spectrometry

Analysis of the retained hydrocarbons was performed on an Agilent 6890 N Gas Chromatograph connected to an Agilent 5793 Mass Selective Detector equipped with an HP-5MS column (60 m, 0.25 mm i.d. stationary phase thickness 0.25 μm). The zeolite sample was dissolved in 15% HF for 30 min. Then CH_2Cl_2 containing C_2Cl_6 internal standard was added to the solution in order to extract the released hydrocarbons. The water phase is separated from the organic phase and the organic extract was consequently analyzed.^[63, 64]

2.2.2 Materials

The formation of carbonaceous deposits during the MTO reaction has been investigated, in a comparative study, between micron-sized H-ZSM-5 and H-SAPO-34 zeolites at the individual particle level. The scanning electron microscopy (SEM) images of these crystals are given in Figures 2.3a and b.

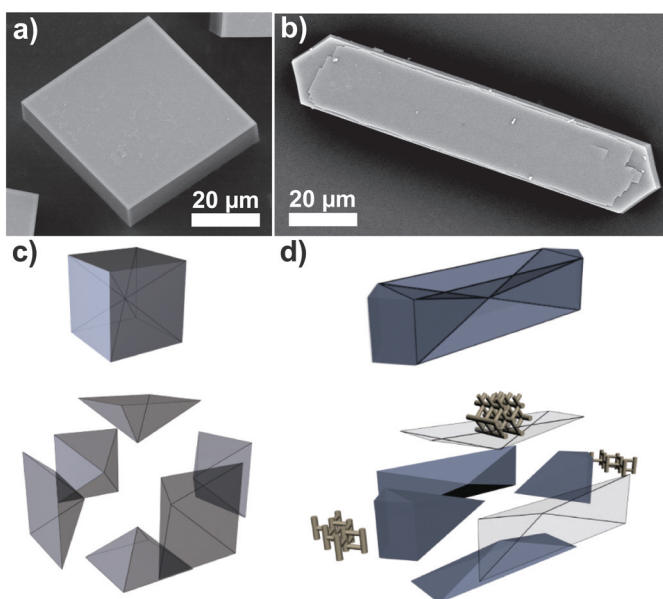


Figure 2.3: Scanning electron microphotograph (SEM) pictures of the micron-sized H-SAPO-34 (a and c) and H-ZSM-5 and (b and d) crystals under study together with the proposed intergrowth structure and the exploded representation thereof with pore orientation.

These crystals are not single crystals, but rather consist of several intergrowth subunits that are illustrated in Figures 2.3c and d and described in detail in literature.^[65-67] The H-SAPO-34 crystals are synthesized following procedures

elaborated for growing large crystals and provided by the Max-Planck-Institute, Mülheim an der Ruhr, Germany.^[68, 69] The H-SAPO-34 crystals have dimensions of 50 x 50 x 50 μm and a Si/Al ratio of ~ 0.4 as determined by SEM-EDX and XRF measurements. The H-ZSM-5 zeolites, with dimensions of 100 x 20 x 20 μm and a Si/Al ratio of ~ 17 were provided by ExxonMobil, Machelen, Belgium.

Prior to measurements, the crystals were detemplated in oxygen for 12 h at 923 K and 823 K for H-SAPO-34 and H-ZSM-5, respectively. After template removal, the crystals were converted in their acid form by triple ion-exchange with a 10 wt% ammonium nitrate (99+%, Acros Organics) solution and subsequent calcination at 823 K. Methanol (99%, Antonides-Interchema) was used as received. During reaction, the crystals were monitored using UV-Vis micro-spectroscopy and confocal fluorescence microscopy. In what follows, we will discuss the in-situ spectroscopy results separately for the H-ZSM-5 and H-SAPO-34 crystals.

2.3 Results and discussion

2.3.1 In-situ micro-spectroscopy over H-ZSM-5 crystals

Upon exposure of methanol vapour, the translucent H-ZSM-5 crystals undergo darkening due to the formation of carbonaceous deposits. Optical microphotographs of the H-ZSM-5 crystals are taken during the MTO reaction as a function of time-on-stream. A selection of these images is shown in Figure 2.4 for the reaction temperatures of 530 and 745 K.

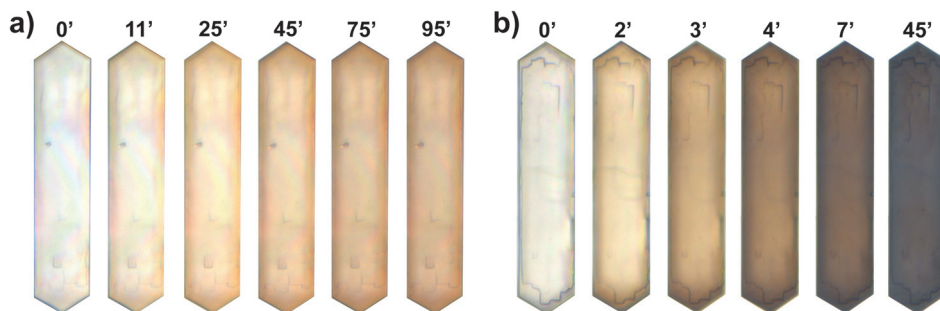


Figure 2.4: Optical microphotographs of H-ZSM-5 crystals taken during the MTO reaction at (a) 530 K and (b) 745 K. The corresponding time is indicated in min.

Inspection of Figure 2.4 reveals that the color of the crystal varies depending on the reaction temperature. Moderate reaction conditions generate a mild yellow-brown darkening, whereas increasing reaction temperature, results

in intense crystal coloration that ends in a gray-black tint. The darkening process starts at the zeolite surface and with time-on-stream, the coloration gradually spreads throughout the entire H-ZSM-5 crystal. Moreover, during the early stages of the MTO reaction, the coke deposition is observed to be faster in the triangular areas at the crystal ends. The pore architecture of the H-ZSM-5 crystal, as shown in Figure 2.3, reveals that in this region the large straight pores are in open contact to the external surface.^[62, 69, 70]

The time-resolved optical absorption measurements, taken during the MTO reaction from a 2 μm spot in the central region of the H-ZSM-5 crystal, fully reflect the optically observed temperature dependent color variations. The results are shown in Figure 2.5.

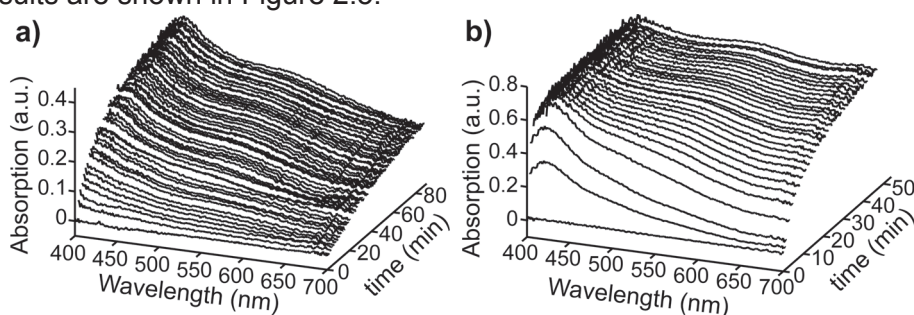


Figure 2.5: Optical absorption spectra of H-ZSM-5 crystals during the MTO reaction taken at (a) 530 K and (b) 745 K. The spectra are taken from a spot in the crystal centre.

The growth of carbonaceous deposits results in the formation of two broad absorption bands located around 415 nm and 550 nm. The 415 nm absorption band is formed first and the progressive growth of both bands occurs with further methanol conversion. The intensity of these bands directly correlates to the applied reaction conditions and with increasing reaction temperature, an additional broad background absorption, stretching across the whole visible region, becomes apparent.

The absorption band located around 415 nm has been previously assigned to the π - π^* transitions that originate from methyl-substituted benzenium cations.^[71-80] These species play an important role in the hydrocarbon pool mechanism, as the interaction of these organic intermediates with the acidic zeolite centers constitute the catalytic engine for the alkene formation.^[4, 41, 81] The band at 550 nm starts as a shoulder of the prior discussed 415 nm band. Its higher wavelength with apparent red shift indicates the growth of extended conjugated aromatic species. The observation that the formation of the 550 nm absorption band lags behind the 415 nm band furthermore suggests that these compounds originate from the former mentioned benzenium species.^[52, 54, 58, 82, 83]

Similar measurements are performed at various temperatures. The temporal evolution of the thereby obtained absorption bands that are located at 415 nm is shown in Figure 2.6a. From Figure 2.6a, two distinct temperature regions can be identified. Below 615 K, the profiles remain identical within the experimental error, whereas above that point higher temperatures result in faster kinetics. This finding is elaborated further with the corresponding Arrhenius plot shown in Figure 2.6b. The graph illustrates the effective reaction rate vs. the reaction temperature. Here, the time-resolved evolution profiles of the band absorption were fitted with first order kinetics after which extraction of the effective reaction rates occurred.

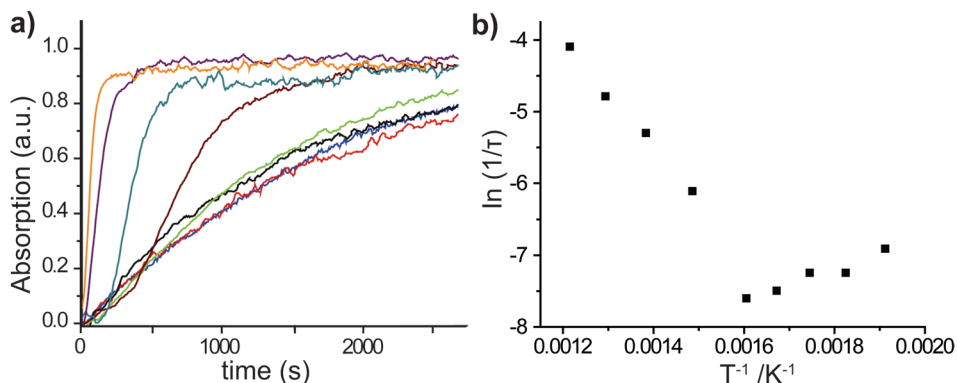


Figure 2.6: a) Temporal evolution of the absorption band located at 415 nm. The UV-Vis bands are taken from a spot in the H-ZSM-5 crystal centre as a function of time-on-stream for different reaction temperatures: 530 K (red); 550 K (black); 573 K (blue); 615 K (green); 660 K (cyan); 700 K (wine); 745 K (purple); 773 K (orange). The corresponding Arrhenius plot of the fitted curves is shown in (b).

The above-mentioned findings can be rationalized by considering the production of two different types of carbonaceous species. Previous studies showed that for H-ZSM-5 catalysts, poly-methylated benzenes are formed within the zeolite channels, whereas larger graphite-like compounds can deposit on the external surface of the zeolite crystal.^[29, 84-87] Along these lines, it is reasonable to assume that mono-aromatic compounds are responsible for the absorption band at 415 nm. More extended derivatives thereof constitute the absorption band around 550 nm and external graphite-like species absorb all wavelengths across the optical region. At 530-615 K, aromatic compounds retained within the zeolite channels are predominantly formed. This process appears to be nearly activation-less, as evidenced in the low temperature region of the Arrhenius plot. It is plausible that at those temperatures, the formation of aromatic compounds mainly depends on the mass transport to the bulk of the H-ZSM-5 crystals. Above 615 K, the formation of larger

conjugated species and graphite-like compounds becomes more significant, as reflected by the appearance of the structure-less absorption spectrum. In H-ZSM-5, an increasing reaction temperature not only raises the formation rate of large carbonaceous species, but additionally facilitates cracking of hydrocarbons. This leads to the formation of extended graphite-like residues that appears to have positive activation energy, as supported by the high temperature region of the Arrhenius plot.

In-situ UV-Vis micro-spectroscopy gives valuable insights into the coke deposition on zeolite crystals. However, the thickness of the layer probed with this method varies depending on the optical properties of the sample. Carbonaceous species within a zeolite confinement can exhibit fluorescence.^[65, 88] Confocal fluorescence microscopy therefore allows monitoring the spatial distribution of hydrocarbon species within an individual catalyst particle. Figure 2.7 shows the confocal images of the H-ZSM-5 crystal taken during the MTO reaction. The two excitation wavelengths used are 488 and 561 nm with fluorescence detection windows at 510-550 and 575-635 nm, respectively.

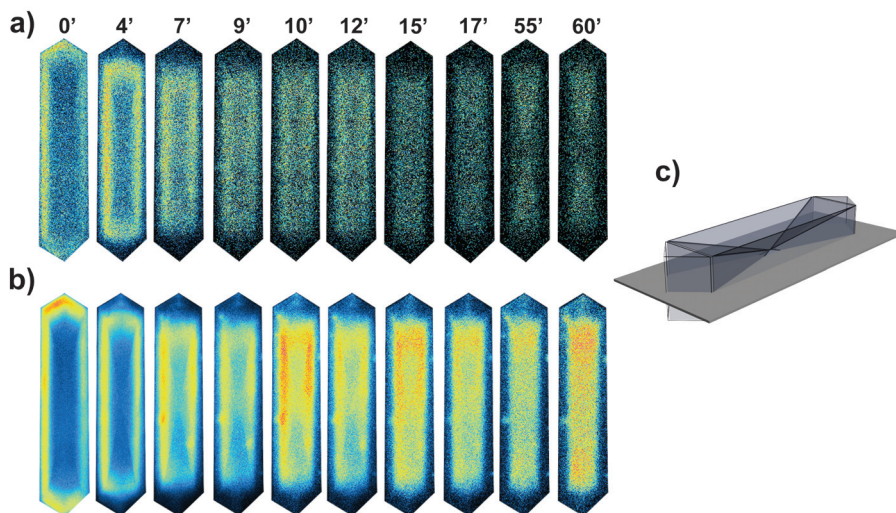


Figure 2.7: a) Confocal fluorescence microscopy images of H-ZSM-5 crystal during MTO reaction at 660 K depicted with time-on-stream at laser excitation (a) 488 nm (detection at 510-550 nm) and (b) 561 nm (detection at 565-635 nm). The images are shown in false color (intensity profile) and the corresponding time is indicated in min. A schematic representation of the slice where the confocal fluorescence measurement has been performed is illustrated in (c).

Upon exposure to methanol, intense fluorescence is immediately detected at the near-surface region of the H-ZSM-5 zeolite. With time-on-stream, both wavelengths exhibit a front of fluorescent molecules that gradually moves from the crystal surface inwards. After ~ 8 min of reaction time, intra-crystalline diffusion boundaries arise. Figure 2.7 shows that fluorescent species photo-excited with 488 nm readily penetrate towards the inner core of the crystal, whereas compounds excited at 561 nm, undergo more diffusion limitations. These are most pronounced at the crystal subunits interfaces, where channel mismatch allows the observation of the characteristic hourglass pattern. The different patterns obtained with separate excitation wavelengths point out that they correspond to distinct fluorescent species. These compounds most likely differ in their molecular dimensions and the red shift in the excitation wavelength corresponds to a growing molecular size.^[70, 89, 90] In the present case, it can be due to a different degree of benzene ring methylation or a larger conjugated system that might exist within the 10-ring channels. The observation that the species exhibiting fluorescence at lower wavelengths penetrate the intra-crystalline boundaries faster thereby supports this assumption. It is furthermore observed that after ~ 5 min of reaction, the zeolite boundary region lacks fluorescent intensity, whereas curiously optical examination showed higher coloration intensity in this region. The preferential accumulation of coke at the triangular edges of the crystals can in principle originate from intra-crystalline hydrocarbon species or from surface graphite-like depositions. The scarce fluorescence detection supports the suggestion that coke species located in this region are likely of graphitic nature. These findings imply that the straight channels of H-ZSM-5 are more prone to pore blocking. The areas where the external surface is connected via zigzag pores segments give reactant and product molecules more ways to diffuse inside and outside the crystal. Straight pore openings, on the other hand, appear to block faster, forcing the formation of the surface coke.

2.3.2 In-situ micro-spectroscopy over H-SAPO-34 crystals

Micron-sized H-SAPO-34 crystals have been investigated in a set of experiments similar to those described previously for large H-ZSM-5 crystals. In Figure 2.8, a selection of the optical microphotographs taken during the MTO reaction on H-SAPO-34 is shown. The images are depicted as a function of time-on-stream at two different reaction temperatures; i.e. 530 and 745 K.

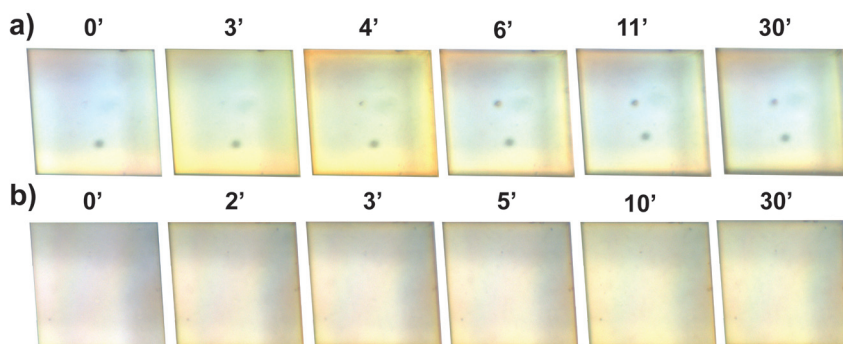


Figure 2.8: Optical microphotographs of H-SAPO-34 crystals taken during the MTO reaction at (a) 530 K and (b) 745 K. The corresponding time is indicated in min.

Comparison between Figures 2.4 and 2.8 reveals clear differences between the coke formation on H-ZSM-5 and H-SAPO-34 crystals. The MTO conversion performed on H-SAPO-34 at 530 K generates a strong yellow coloration that is primarily observed along the edges of the crystals. Surprisingly, during the experiments the color intensity first strongly increases and later on decreases as illustrated by the image taken after 4 min in Figure 2.8a. However, such a drop is not observed above 573 K where instead the crystals darkening gradually progresses with time-on-stream.

The time-resolved UV-Vis spectra of a H-SAPO-34 crystal taken at a reaction temperature of 530 K are shown in Figure 2.9a. Similar to the case of the H-ZSM-5 crystals, the most prominent feature in the spectra is a strong absorption band at 400 nm, assigned to methyl-substituted benzene cations.^[71-80] After reaching the intensity maximum, the absorption band decreases in intensity which is in line with the optical observations.

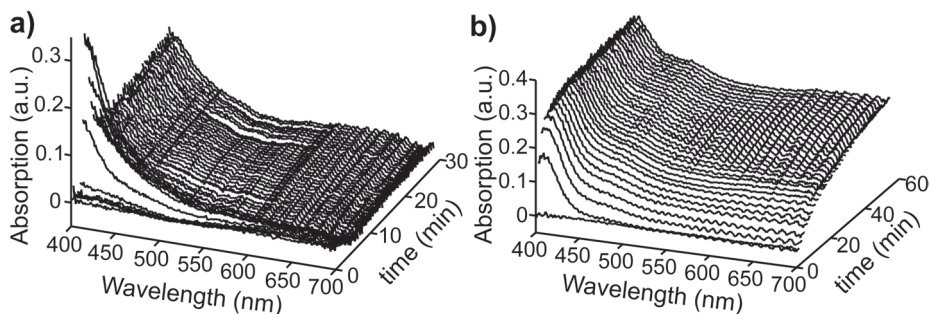


Figure 2.9: Optical absorption spectra of H-SAPO-34 crystals during the MTO reaction as a function of time-on-stream at (a) 530 K and (b) 745 K. The spectra were taken from a spot in the middle of the crystal.

The time-resolved UV-Vis absorption measurements performed at 745 K, as summarized in Figure 2.9b, also show the formation of an absorption band around 400 nm. The intensity of this absorption band does not decrease with time-on-stream and in addition, a second absorption band located at 480 nm is observed. It should be noticed that, as in the case of H-ZSM-5, the rise of this additional band does not occur at the expense of the 400 nm band. Furthermore, a rise of the overall background absorption is observed which is indicative for the formation of extended carbonaceous deposits with possible graphite nature. In contrast to H-ZSM-5 however, no pronounced blackening was observed in the analysis of the optical microphotographs, suggesting that the carbonaceous deposits are confined in size and mainly retained inside the H-SAPO-34 crystal. At 530 K, the formation of a strong absorption band that, with progressing reaction time, diminishes in intensity suggests the occurrence of an induction period that, in this case, mainly takes place near the zeolite surface.

Details on the elemental composition of these species is provided by dissolving the zeolite crystals in HF, extracting the retained material with dichloromethane and analyzing the organic phase by means of GC-MS.^[22, 64, 91] The results are shown in Figure 2.10.

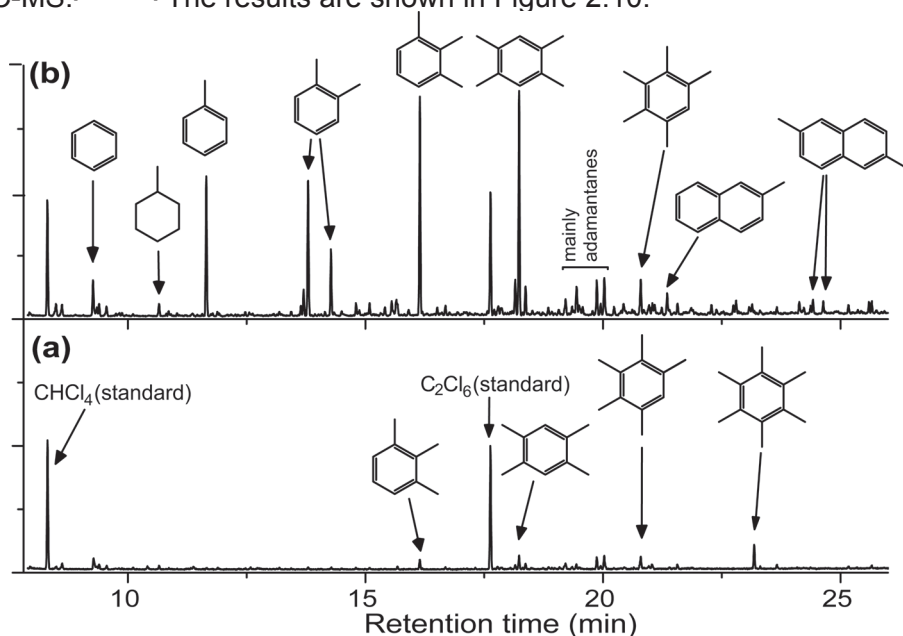


Figure 2.10: Gas chromatograms of coke species retained in H-SAPO-34 after (a) 3 min and (b) 60 min of reaction at 530 K.

From Figure 2.10a it is clear that the observed intense yellow coloration of the H-SAPO-34 zeolite is largely caused by highly methyl substituted benzenes, whereas crystals exposed to a methanol stream for a longer period of time contain a larger variety of hydrocarbons including methylated polyaromatic species (Figure 2.10b).

Figure 2.11 shows the time evolution of the absorption band at around 400 nm at different reaction temperatures. Similar to H-ZSM-5, two temperature regions can be discriminated. Below 573 K, the band intensity passes through a maximum and subsequently drops to about 20% of its peak intensity. At higher temperatures, the band intensity grows steadily and remains constant after reaching its maximum value. Remarkably, analysis of the kinetic profiles indicates that the build-up of the 400 nm band, above 700 K, is slower compared to those in the 600-700 K range.

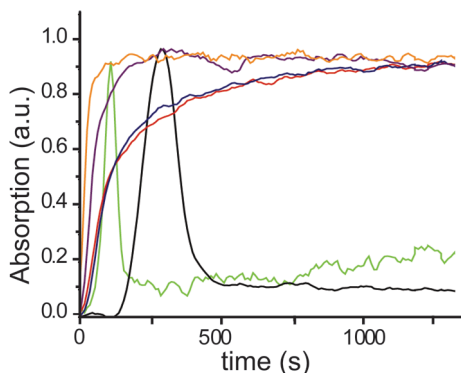


Figure 2.11: Time evolution of the optical absorption at 400 nm taken from a spot in the centre of the H-SAPO-34 crystal as a function of time-on-stream at different reaction temperatures: 530 K (black); 573 K (green); 615 K (purple); 660 K (orange); 700 K (red); and 745 K (blue).

The reaction intermediates that form during the MTO conversion in H-SAPO-34 are not limited to mono-aromatic compounds.^[25, 43, 51, 92-94] This is mainly due to the CHA framework topology, as the large cages can accommodate relatively large molecules. The appearance of the 400 nm band is associated with poly-methylated benzenes, while more extended conjugated compounds contribute to the optical absorption around 480 nm with an additional broad absorption background. The kinetic slow down above 660 K is in agreement with previous findings that report of a shift from hydrocarbon accumulation towards cracking into olefins with increasing temperatures.^[95, 96]

Confocal fluorescence microscopy measurements, similar to those performed with H-ZSM-5, have been carried out with the H-SAPO-34 crystals. A selection of the confocal fluorescence images is shown in Figure 2.12a, where the resulting fluorescence intensity profiles are recorded at 660 K using the 561 nm laser excitation wavelength. The fluorescent compounds initially form at the crystal corners. In these regions, the flux of reactants and products leads to the fastest formation of fluorescent coke species and their precursor molecules. Further on, the formation of fluorescent compounds extends and eventually, the fluorescent molecules form a front that slowly moves towards the centre of the crystal. However, the majority of the fluorescent compounds remain located near the crystal edge. This observation differs to previous findings made with the H-ZSM-5 crystals. The coke formation process in H-SAPO-34 catalysts mainly consists of poly-aromatic compounds that grow in the zeolite cavities. These species form initially at the near surface area and hinder the further migration of molecules through the crystal, making the internal region of the crystal less accessible.

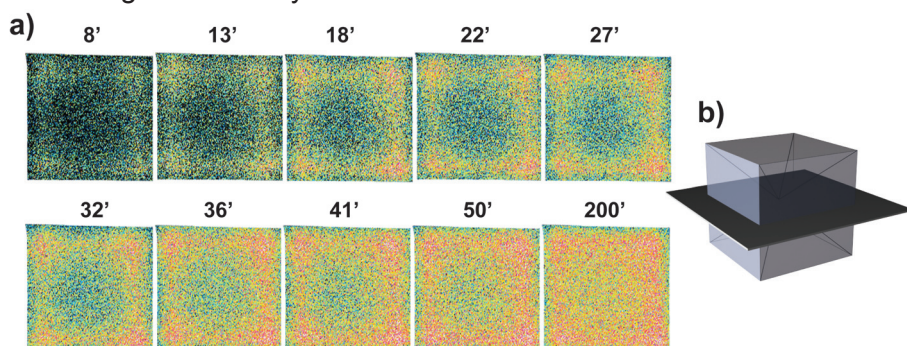


Figure 2.12: a) Confocal fluorescence microscopy images of H-SAPO-34 crystal during the MTO reaction at 660 K, depicted with time-on-stream at 561 nm laser excitation (detection at 565-635 nm). The images are shown in false color (intensity profile) and the corresponding time is indicated in min. A schematic representation of the slice where the confocal fluorescence measurement is performed is illustrated in (b).

2.4 Conclusions

The combination of in-situ UV-Vis micro-spectroscopy and confocal fluorescence microscopy is a valuable tool to probe coke deposits and their precursors during a catalytic reaction. The use of a high-temperature in-situ gas-flow cell allows to monitor the coke formation process during the methanol-to-olefin (MTO) reaction and large micron-sized zeolite crystals permit to visualize the carbonaceous deposition in a time- and space-

resolved manner. The versatile methodology illustrates that the formation of coke species during the MTO reaction on H-ZSM-5 crystals differs from that on H-SAPO-34 crystals. Coke on H-ZSM-5 crystals is initially formed at the crystal edges, where straight pores are in contact with the crystal outer surface and the crystal coloration intensifies with increasing reaction temperature. Two separate temperature regions suggest the formation of two distinct coke systems i.e. methylated aromatics and graphite-like coke compounds. The pore architecture of H-ZSM-5 explains these findings: hydrocarbon compounds within the zeolite pores contribute to the internal coke formation as well as olefin production while large graphite-like compounds block the pore openings at the zeolite external surface. Confocal fluorescence experiments confirm the preferred accumulation of large coke deposits near the crystal surface area while coke, composed of (poly) methylated aromatic species, moves towards the centre of the zeolite crystal and intra-crystalline boundaries slow down the internal diffusion process. The H-SAPO-34 crystals show a fast formation of methyl-substituted aromatic compounds at the corners and edges of the catalyst crystal. With increasing temperature larger delocalized conjugated systems form as well. Confocal fluorescence microscopy measurements confirm the formation of fluorescent coke compounds starting at the corners of the H-SAPO-34 crystals and illustrates that the majority of these species remain located at the edges of the crystal, thereby frustrating further coke formation within the crystal core. These findings are also explained by the architecture of the crystal: large carbonaceous deposits, formed in the cages at the edge of the crystal, prevent the reaction front to move towards the centre of the crystal leading to fast catalyst deactivation.

Acknowledgements

Dr. Machteld Mertens (ExxonMobil, Belgium) is acknowledged for providing the H-ZSM-5 crystals, while Dr. Jan Kornatowski (Max Planck Institute, Germany) is thanked for providing the H-SAPO-34 crystals. Prof. Unni Olsbye and Francesca Bleken (Oslo University, Norway) are thanked for the GC-MS measurements as well as fruitful discussions. Marjan Versluijs-Helder is acknowledged for performing the SEM-EDX and XRF measurements. Dr. Eli Stavitski and Dr. Marianne Kox are thanked for productive consultations and knowledge transmission regarding the micro-spectroscopic equipment.

References

- [1] H. van Bekkum, E.M. Flanigen, P.A. Jacobs, J.C. Jansen (Eds.), *Introduction to Zeolite Science and Practice*, Elsevier, Amsterdam, **2001**.
- [2] G. Busca, *Chem. Rev.* **2007**, 107, 5366-5410.
- [3] R.A. van Santen, P.W.N.M. van Leeuwen, J.A. Moulijn, B.A. Averil (Eds.), *Catalysis an Integrated Approach*, Elsevier, Amsterdam, **2000**.
- [4] M. Stöcker, *Microporous Mesoporous Mater.* **1999**, 29, 3-48.
- [5] G. A. Olah, *Angew. Chem. Int. Ed.* **2005**, 44, 2636-2639.
- [6] C. Okkerse, H. van Bekkum, *Green Chem.* **1999**, 1, 107-114.
- [7] T. Mokrani, M. Scurrall, *Catal. Rev. Sci. Eng.* **2009**, 51, 1-45.
- [8] C. D. Chang, A. J. Silvestri, *J. Catal.* **1977**, 47, 249-259.
- [9] J. Q. Chen, A. Bozzano, B. Glover, T. Fuglerud, S. Kvisle, *Catal. Today* **2005**, 106, 103-107.
- [10] J. Grootjans, V. Vanrysselberghe, W. Vermeiren, *Catal. Today* **2005**, 106, 57-61.
- [11] K. R. Hall, *Catal. Today* **2005**, 106, 243-246.
- [12] J. Topp-Jørgensen, *Stud. Surf. Sci. Catal.* **1988**, 36, 293.
- [13] H. Koempel, W. Liebner, *Stud. Surf. Sci. Catal.* **2007**, 167, 261-267.
- [14] I. M. Dahl, S. Kolboe, *Catal. Lett.* **1993**, 20, 329-336.
- [15] I. M. Dahl, S. Kolboe, *J. Catal.* **1994**, 149, 458-464.
- [16] I. M. Dahl, S. Kolboe, *J. Catal.* **1996**, 161, 304-309.
- [17] B. Arstad, S. Kolboe, O. Swang, *J. Phys. Chem. B* **2002**, 106, 12722-12726.
- [18] B. Arstad, J. B. Nicholas, J. F. Haw, *J. Am. Chem. Soc.* **2004**, 126, 2991-3001.
- [19] B. Arstad, S. Kolboe, O. Swang, *J. Phys. Chem. A* **2005**, 109, 8914-8922.
- [20] M. Bjorgen, U. Olsbye, S. Svelle, S. Kolboe, *Catal. Lett.* **2004**, 93, 37-40.
- [21] M. Bjorgen, U. Olsbye, D. Petersen, S. Kolboe, *J. Catal.* **2004**, 221, 1-10.
- [22] M. Bjorgen, S. Svelle, F. Joensen, J. Nerlov, S. Kolboe, F. Bonino, L. Palumbo, S. Bordiga, U. Olsbye, *J. Catal.* **2007**, 249, 195-207.
- [23] M. Bjorgen, F. Joensen, K. P. Lillerud, U. Olsbye, S. Svelle, *Catal. Today* **2009**, 142, 90-97.
- [24] H. S. Cerqueira, P. C. Mihindou-Koumba, P. Magnoux, M. Guisnet, *Ind. Eng. Chem. Res.* **2001**, 40, 1032-1041.
- [25] J. F. Haw, W. G. Song, D. M. Marcus, J. B. Nicholas, *Acc. Chem. Res.* **2003**, 36, 317-326.
- [26] D. Lesthaeghe, V. Van Speybroeck, G. B. Marin, M. Waroquier, *Ind. Eng. Chem. Res.* **2007**, 46, 8832-8838.
- [27] D. Lesthaeghe, A. Horre, M. Waroquier, G. B. Marin, V. Van Speybroeck, *Chem. Eur. J.* **2009**, 15, 10803-10808.
- [28] D. Lesthaeghe, J. Van der Mynsbrugge, M. Vandichel, M. Waroquier, V. Van Speybroeck, *ChemCatChem.* **2011**, 3, 208-212.
- [29] U. Olsbye, M. Bjorgen, S. Svelle, K. P. Lillerud, S. Kolboe, *Catal. Today* **2005**, 106, 108-111.

- [30] S. Svelle, F. Joensen, J. Nerlov, U. Olsbye, K. P. Lillerud, S. Kolboe, M. Bjorgen, *J. Am. Chem. Soc.* **2006**, 128, 14770-14771.
- [31] S. Svelle, M. Bjorgen, S. Kolboe, D. Kuck, M. Letzel, U. Olsbye, O. Sekiguchi, E. Uggerud, *Catal. Lett.* **2006**, 109, 25-35.
- [32] W. G. Song, D. M. Marcus, H. Fu, J. O. Ehresmann, J. F. Haw, *J. Am. Chem. Soc.* **2002**, 124, 3844-3845.
- [33] M. Stöcker, *Microporous Mesoporous Mater.* **1999**, 29, 3-48.
- [34] A. T. Aguayo, A. G. Gayubo, R. Vivanco, M. Olazar, J. Bilbao, *Appl. Catal. A* **2005**, 283, 197-207.
- [35] A. Corma, *Chem. Rev.* **1995**, 95, 559-614.
- [36] A. G. Gayubo, P. L. Benito, A. T. Aguayo, M. Olazar, J. Bilbao, *J. Chem. Technol. Biotechnol.* **1996**, 65, 186-192.
- [37] B. P. C. Hereijgers, F. Bleken, M. H. Nilsen, S. Svelle, K. P. Lillerud, M. Bjorgen, B. M. Weckhuysen, U. Olsbye, *J. Catal.* **2009**, 264, 77-87.
- [38] J. W. Park, S. J. Kim, M. Seo, S. Y. Kim, G. Seo, *Appl. Catal. A* **2008**, 349, 76-85.
- [39] C. Baerlocher, W.M. Meier, D.H. Olson (Eds.), *Atlas of Zeolite Framework Types*, Elsevier, Amsterdam, **2001**.
- [40] H. van Bekkum, F. Bauer (Eds.), *Molecular Sieves*, Springer-Verlag, Berlin Heidelberg, **2007**.
- [41] M. Bjorgen, S. Akyalcin, U. Olsbye, S. Benard, S. Kolboe, S. Svelle, *J. Catal.* **2010**, 275, 170-180.
- [42] X. J. Cheng, X. S. Wang, H. Y. Long, *Microporous Mesoporous Mater.* **2009**, 119, 171-175.
- [43] W. G. Song, H. Fu, J. F. Haw, *J. Phys. Chem. B* **2001**, 105, 12839-12843.
- [44] S. Teketel, U. Olsbye, K. P. Lillerud, P. Beato, S. Svelle, *Microporous Mesoporous Mater.* **2010**, 136, 33-41.
- [45] P. L. Benito, A. G. Gayubo, A. T. Aguayo, M. Olazar, J. Bilbao, *Ind. Eng. Chem. Res.* **1996**, 35, 3991-3998.
- [46] S. Bhatia, J. Beltramini, D. D. Do, *Catal. Rev. Sci. Eng.* **1989**, 31, 431-480.
- [47] M. Bjorgen, U. Olsbye, S. Kolboe, *J. Catal.* **2003**, 215, 30-44.
- [48] G. F. Froment, J. Demeyer, E. G. Derouane, *J. Catal.* **1990**, 124, 391-400.
- [49] M. Guisnet, P. Magnoux, *Appl. Catal. A* **2001**, 212, 83-96.
- [50] M. Guisnet, P. Magnoux, *Appl. Catal.* **1989**, 54, 1-27.
- [51] J. F. Haw, D. M. Marcus, *Top. Catal.* **2005**, 34, 41-48.
- [52] K. Hemelsoet, A. Nollet, M. Vandichel, D. Lesthaeghe, V. Van Speybroeck, M. Waroquier, *ChemCatChem.* **2009**, 1, 373-378.
- [53] M. Hureau, A. Moissette, S. Marquis, C. Bremard, H. Vezin, *Phys. Chem. Chem. Phys.* **2009**, 11, 6299-6307.
- [54] D. Lesthaeghe, V. Van Speybroeck, M. Waroquier, *Phys. Chem. Chem. Phys.* **2009**, 11, 5222-5226.
- [55] J. Li, G. Xiong, Z. Feng, Z. Liu, Q. Xin, C. Li, *Microporous Mesoporous Mater.* **2000**, 39, 275-280.

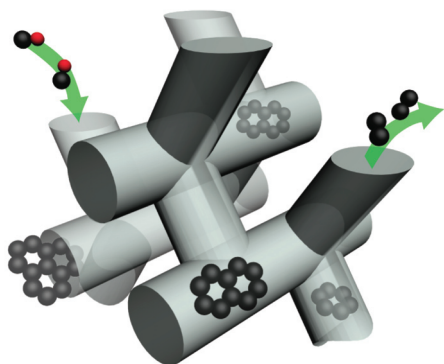
- [56] P. Magnoux, H. S. Cerqueira, M. Guisnet, *Appl. Catal. A* **2002**, 235, 93-99.
- [57] J. Liang, H. Y. Li, S. Zhao, W. G. Guo, R. H. Wang, M. L. Ying, *Appl. Catal.* **1990**, 64, 31-40.
- [58] H. Schulz, *Catal. Today* **2010**, 154, 183-194.
- [59] H. Schulz, K. Lau, M. Claeys, *Appl. Catal. A* **1995**, 132, 29-40.
- [60] L. Travalloni, A. C. L. Gornes, A. B. Gaspar, M. A. P. da Silva, *Catal. Today* **2008**, 133, 406-412.
- [61] D. Chen, H. Rebo, K. Moljord, A. Holmen, *Ind. Eng. Chem. Res.* **1999**, 38, 4241-4249.
- [62] E. Stavitski, M. H. F. Kox, B. M. Weckhuysen, *Chem. Eur. J.* **2007**, 13, 7057-7065.
- [63] F. Bleken, M. Bjorgen, L. Palumbo, S. Bordiga, S. Svelle, K. P. Lillerud, U. Olsbye, *Top. Catal.* **2009**, 52, 218-228.
- [64] S. Teketel, S. Svelle, K. P. Lillerud, U. Olsbye, *ChemCatChem.* **2009**, 1, 78-81.
- [65] L. Karwacki, E. Stavitski, M. H. F. Kox, J. Kornatowski, B. M. Weckhuysen, *Angew. Chem. Int. Ed.* **2007**, 46, 7228-7231.
- [66] L. Karwacki, M. H. F. Kox, D. A. M. de Winter, M. R. Drury, J. D. Meeldijk, E. Stavitski, W. Schmidt, M. Mertens, P. Cubillas, N. John, A. Chan, N. Kahn, S. R. Bare, M. Anderson, J. Kornatowski, B. M. Weckhuysen, *Nature Mater.* **2009**, 8, 959-965.
- [67] L. Karwacki, H. E. van der Bij, J. Kornatowski, P. Cubillas, M. R. Drury, D. A. M. de Winter, M. W. Anderson, B. M. Weckhuysen, *Angew. Chem. Int. Ed.* **2010**, 49, 6790-6794.
- [68] J. Kornatowski, *Zeolites* **1988**, 8, 77-78.
- [69] M. H. F. Kox, E. Stavitski, B. M. Weckhuysen, *Angew. Chem. Int. Ed.* **2007**, 46, 3652-3655.
- [70] M. H. F. Kox, E. Stavitski, J. C. Groen, J. Perez-Ramirez, F. Kapteijn, B. M. Weckhuysen, *Chem. Eur. J.* **2008**, 14, 1718-1725.
- [71] I. Kiricsi, G. Tasi, H. Forster, P. Fejes, *J. Mol. Struct.* **1990**, 218, 369-374.
- [72] I. Kiricsi, H. Forster, G. Tasi, J. B. Nagy, *Chem. Rev.* **1999**, 99, 2085-2114.
- [73] J. Melsheimer, D. Ziegler, *J. Chem. Soc. Faraday Trans.* **1992**, 88, 2101-2108.
- [74] M. Bjorgen, F. Bonino, S. Kolboe, K. P. Lillerud, A. Zecchina, S. Bordiga, *J. Am. Chem. Soc.* **2003**, 125, 15863-15868.
- [75] W. Wang, Y. J. Jiang, M. Hunger, *Catal. Today* **2006**, 113, 102-114.
- [76] C. Paze, B. Sazak, A. Zecchina, J. Dwyer, *J. Phys. Chem. B* **1999**, 103, 9978-9986.
- [77] R. H. Meinhold, D. M. Bibby, *Zeolites* **1990**, 10, 121-130.
- [78] R. H. Meinhold, D. M. Bibby, *Zeolites* **1990**, 10, 146-150.
- [79] L. Palumbo, F. Bonino, P. Beato, M. Bjorgen, A. Zecchina, S. Bordiga, *J. Phys. Chem. C* **2008**, 112, 9710-9716.
- [80] J. W. Park, G. Seo, *Appl. Catal. A* **2009**, 356, 180-188.
- [81] W. J. H. Dehertog, G. F. Froment, *Appl. Catal.* **1991**, 71, 153-165.
- [82] A. Sassi, M. A. Wildman, H. J. Ahn, P. Prasad, J. B. Nicholas, J. F. Haw, *J. Phys. Chem. B* **2002**, 106, 2294-2303.
- [83] L. Jansen van Rensburg, R. Hunter, G. J. Hutchings, *Appl. Catal.* **1988**, 42, 29-34.

- [84] D. M. McCann, D. Lesthaeghe, P. W. Kletnieks, D. R. Guenther, M. J. Hayman, V. Van Speybroeck, M. Waroquier, J. F. Haw, *Angew. Chem. Int. Ed.* **2008**, 47, 5179-5182.
- [85] D. Chen, A. Gronvold, H. P. Rebo, K. Moljord, A. Holmen, *Appl. Catal. A. Gen.* **1996**, 137, 1-8.
- [86] F. F. Madeira, N. S. Gnep, P. Magnoux, H. Vezin, S. Maury, N. Cadranl, *Chem. Eng. J.* **2010**, 161, 403-408.
- [87] S. Marquis, A. Moissette, H. Vezin, C. Brémard, *Comp. Ren. Chimie* **2005**, 8, 419-440.
- [88] G. De Cremer, B. F. Sels, D. E. De Vos, J. Hofkens, M. B. J. Roeffaers, *Chem. Soc. Rev.* **2010**, 39, 4703-4717.
- [89] L. Karwacki, B. M. Weckhuysen, *Phys. Chem. Chem. Phys.* **2011**, 13, 3681-3685.
- [90] M. H. F. Kox, A. Mijovilovich, J. J. H. B. Sattler, E. Stavitski, B. M. Weckhuysen, *ChemCatChem.* **2010**, 2, 564-571.
- [91] F. Bleken, W. Skistad, K. Barbera, M. Kustova, S. Bordiga, P. Beato, K. P. Lillerud, S. Svelle, U. Olsbye, *Phys. Chem. Chem. Phys.* **2011**, 13, 2539-2549.
- [92] D. Chen, H. P. Rebo, A. Gronvold, K. Moljord, A. Holmen, *Microporous Mesoporous Mater.* **2000**, 35-6, 121-135.
- [93] H. Fu, W. G. Song, J. F. Haw, *Catal. Lett.* **2001**, 76, 89-94.
- [94] Y. J. Jiang, J. Huang, V. R. R. Marthala, Y. S. Ooi, J. Weitkamp, M. Hunger, *Microporous Mesoporous Mater.* **2007**, 105, 132-139.
- [95] M. W. Anderson, B. Sulikowski, P. J. Barrie, J. Klinowski, *J. Phys. Chem.* **1990**, 94, 2730-2734.
- [96] G. F. Froment, *Catal. Rev. Sci. Eng.* **2008**, 50, 1-18.

Chapter 3

Coke Formation during the Methanol-to-Olefin Conversion over H-ZSM-5 Molecular Sieves

Influence of the Silicon-to-Aluminum Ratio



UV-Vis micro-spectroscopy and confocal fluorescence microscopy demonstrate that the zeolite Brønsted acid site density and applied reaction conditions affect the formation of coke species during the Methanol-to-Olefin conversion. Differences in location and molecular size are monitored at the single catalyst particle level by using polarization dependent measurements and applying multiple excitation wavelength lasers.

3.1 Introduction

The restricted availability of crude oil and the growing public environmental awareness, urge the need to produce transportation fuels and chemicals from other, more sustainable resources. Biomass, natural gas and coal are interesting alternatives because they can be converted into methanol via synthesis gas. In this class of catalytic reactions, commonly referred to as Methanol-to-Hydrocarbons (MTH), the Methanol-to-Olefin (MTO) conversion has gained considerable interest as valuable chemical building blocks, like ethene and propene, can be obtained from this chemical process.^[1, 2] Chapter 2 highlighted the potential of microporous crystalline aluminosilicates and aluminophosphates as catalysts for MTO conversions. The pronounced acidity of these materials accounts for the chemical transformation of methanol, while their well-defined porous structure influences the size and shape selectivity of the hydrocarbons formed.^[3, 4]

At present, most researchers agree that the MTO reaction occurs by the so-called hydrocarbon pool (HCP) mechanism. Here, poly-methylated benzenes and their protonated analogues, constitute the catalytic active HCP scaffold. Methanol is added to these large intermediates and alkenes are formed in a closed catalytic cycle.^[5-8] The precise active species depend on the applied catalyst and in particular its crystallographic architecture. It has been shown that in H-ZSM-5 zeolites, two parallel methanol-consuming cycles occur. The ethene formation proceeds via an aromatic cycle, whereas propene formation is linked to partly the aromatic cycle and partly to an alkene cycle.^[5, 7, 9-13] As a result of the HCP mechanism and additional parallel reactions, the MTO conversion produces a variety of hydrocarbons. Consequently, besides the production of the desired light olefins, poly-olefins, aromatics and undesired carbon deposits are formed as well and these compounds can lead to catalyst deactivation.^[7, 14-16] Coke compounds can, for example, adsorb on the zeolite acid sites, thereby poisoning the catalyst active centers. An increasing methyl-substitution of the aromatic intermediates can furthermore affect both the activity and selectivity of the catalyst while additionally, due to aging, the growth of these undesired compounds can lead to polycyclic aromatic structures that block the crystal pores and restrict mass transportation within the zeolite catalyst.

All processes mentioned occur simultaneously and the distinction between activity-enhancing and deactivating species is not unambiguous. Extensive studies therefore aim at improving olefin conversion or reducing the catalyst deactivation process.^[17-24] The study of the formation of coke deposits requires powerful analytical tools. Chapter 2 illustrated how in-situ UV-Vis micro-spectroscopy and confocal fluorescence microscopy allow monitoring

spatiotemporal differences in the carbonaceous deposition between individual H-ZSM-5 and H-SAPO-34 crystals.^[25-28] The current Chapter extends that work by introducing the use of multiple laser excitation wavelengths in confocal fluorescence microscopy and by employing polarization-dependent UV-Vis micro-spectroscopy. These tools are used to examine the effect of the Brønsted acid site density on the coke formation that occurs during the MTO conversion on H-ZSM-5 zeolite crystals. The acidity is reflected in the different Si/Al molar ratio of a series of micron-sized H-ZSM-5 catalysts. Their sizes enable individual particle level analysis thereby excluding outer surface area effects encountered in bulk analytical studies.

3.2 Experimental

3.2.1 Methods

UV-Vis micro-spectroscopy

The micro-spectroscopic equipment is described in Chapter 1.^[29] In-situ UV-Vis absorption measurements are performed using the upright research microscope Olympus BX41, equipped with a 50x0.5 NA-high working distance objective. The set-up additionally has a 50/50 double viewport tube that accommodates the CCD video camera (ColorView IIIu, Soft Imaging System GmbH) and an optical fibre mount. A 200 μm -core fibre connects the microscope to a CCD UV/Vis spectrometer (AvaSpec-2048TEC, Avantes). A rotatable polarizer between the objective lens and the detector allow separating a desirable light polarization.

Confocal fluorescence microscopy

Confocal fluorescence microscopy is performed on an upright configuration of the Nikon Eclipse 90i fluorescence microscope. All crystals have been measured using a 50x0.55 NA dry objective lens. The fluorescence images were collected with the use of a Nikon A1-SHR A1 R scan head connected to laser light sources 405, 561 and 637 nm, while the emission was detected in the 425-475, 565-635 and 662-737 nm range, respectively with a PMT.

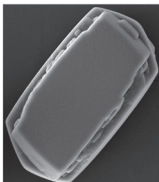
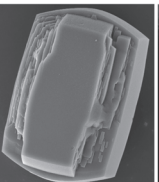
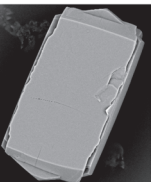
In-situ cell

The experiments were performed on a Linkam FTIR 600 in-situ cell equipped with temperature controller (Linkam TMS 93). The zeolite crystals were heated to 773 K at a rate of 10 $\text{K}\cdot\text{min}^{-1}$ and kept at this temperature under inert atmosphere for 1 h after which the temperature was brought to the desired reaction temperature with a rate of 10 $\text{K}\cdot\text{min}^{-1}$. Subsequently, the N_2 flow was diverted through a bubbler containing the methanol thereby acting as a carrier gas.

3.2.2 Materials

The formation of carbonaceous deposits during the MTO reaction is examined, in a comparative study, between micron-sized H-ZSM-5 crystals containing different Si/Al molar ratio. The preparation methods and details of the micron-sized zeolites (A-E) are reported in the literature.^[30-35] The properties of the investigated H-ZSM-5 molecular sieves are summarized in Table 3.1.

Table 3.1: Micron-sized H-ZSM-5 crystals studied (A-E) with their corresponding properties as determined by SEM-EDX and synthesis protocols.

Sample	A	B	C	D	E
					
Size (μm)	80x40	90x50	100x20	60x35	200x90
Si/Al ratio	11	12	17	37	44

The Si/Al molar ratio of these materials has been determined by the synthesis protocol and the value is confirmed with scanning electron microscopy – energy dispersive X-ray spectroscopy (SEM-EDX) measurements. The crystals were converted into their acid form by triple ion-exchange with a 10 wt% ammonium nitrate (99+%, Acros Organics) solution. SEM-EDX showed a comparable residual sodium content i.e. 0.27, 0.28, 0.11, 0.2 and 0.26 wt. % for crystal A-E, respectively and these values are considered to be within the experimental error. These zeolite materials are not single crystals, but are composed of distinct intergrowth subunits as illustrated in Figure 3.1.^[30, 35]

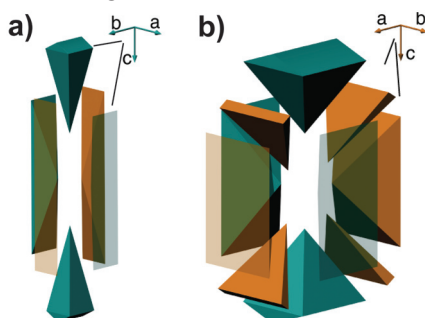


Figure 3.1: Schematic representation of the intergrowth structure of the investigated H-ZSM-5 crystals: (a) crystal C and (b) crystals A, B, D and E. The pore orientations are color coded in green and orange and indicate a 90° rotation over the crystallographic c axis.

More specifically, crystal C has an intergrowth structure consisting of six different subunits with a 90° mismatch, whereas the intergrowth structures of crystals A, B, D and E possess additional subunits, called wedges. The zeolites are investigated during the conversion of methanol into olefins. Methanol (99%, Antonides Interchema) was used as received, while the crystals were monitored using UV-Vis micro-spectroscopy and confocal fluorescence microscopy.

3.3 Results and discussion

3.3.1 In-situ UV-Vis micro-spectroscopy

The large zeolite crystals are placed on the heating stage of the in-situ cell where they are exposed to a methanol flow at two distinct reaction temperatures; i.e. 623 and 773 K. During this process, the formation of carbonaceous deposits causes darkening of the initially transparent H-ZSM-5 crystals. A selection of the optical microphotographs taken during the MTO conversion is displayed in Figure 3.2.

The variations in crystal coloration are indicative of the differences in the nature and formation rate of the coke compounds during the MTO process. At 623 K, the mild reaction conditions induce a soft brown coloration that is obtained for all samples throughout the entire period of reaction. With increasing reaction temperature, the crystals start to show apparent color intensification that eventually ends in a gray/black tint at longer exposure times. Chapter 2 indicated how both the rate and crystal coloration degree depends on the applied reaction conditions and increase with increasing reaction temperature.^[28]

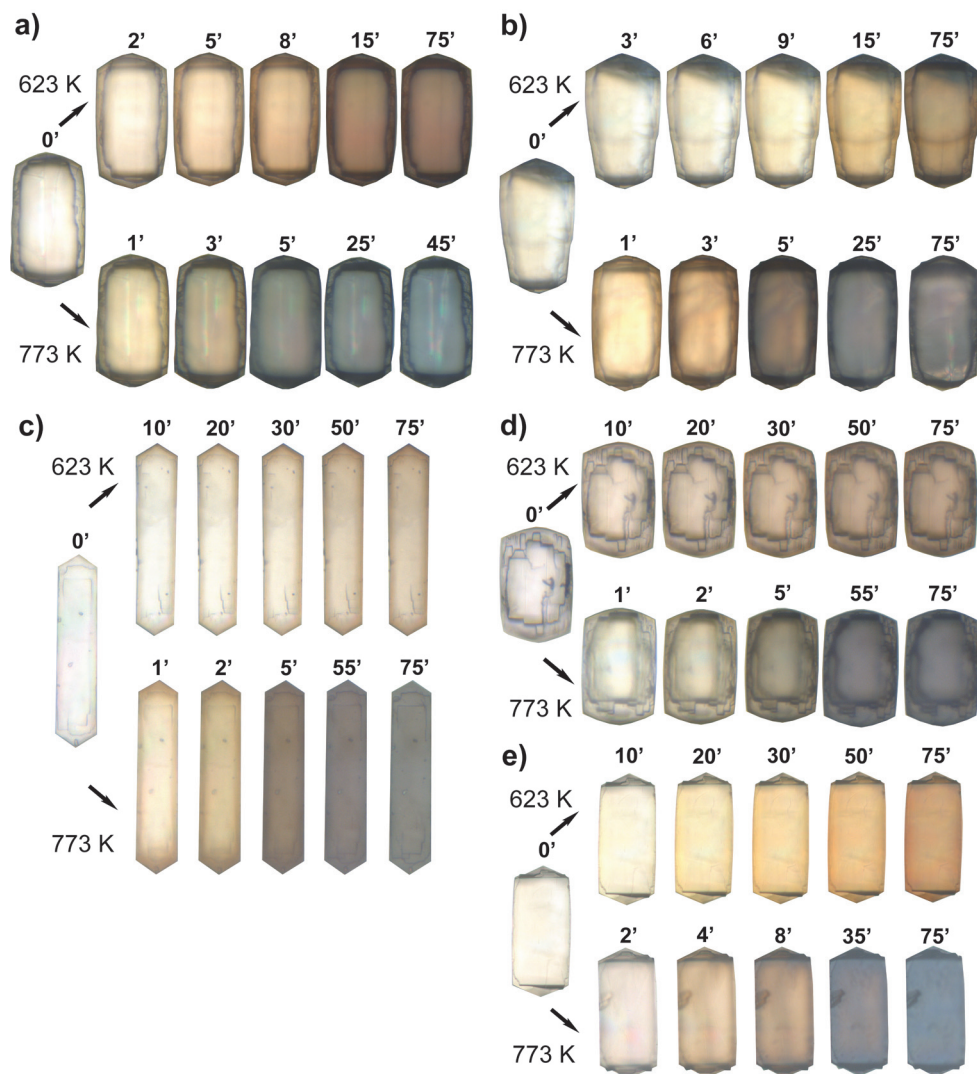


Figure 3.2: Selection of optical microphotographs taken during the MTO conversion for H-ZSM-5 crystal A (a), B (b), C (c), D (d) and E (e). The reaction temperature is 623 K (top) and 773 K (bottom). The corresponding time is indicated in min.

Figure 3.2 additionally illustrates how at both reaction temperatures, a decrease in Brønsted acid site density results in a less pronounced darkening that moreover occurs at a reduced rate. It is known from literature that the bridging OH concentration and the corresponding acid-catalyzed hydrocarbon transformation activity have a linear relationship. This advocates for a comparable strength of the Brønsted acid sites. However, in addition

to the overall acid site density, the local proton distribution and its respective accessibility can influence the hydrocarbon conversion too.^[36-40] The distinct color variations, depending on acid site density, exposure time and applied reaction conditions, are indicative of the influence of these parameters on the coke formation process. The images furthermore illustrate how the coke formation starts at the edges of the H-ZSM-5 crystal, and with time-on-stream, the coloration homogeneously spreads throughout the entire crystal surface. This finding confirms previous observations mentioned in Chapter 2 and indicates that independently of the Brønsted acid site density, the formation of the optically active coke species occurs as soon as the reactants enter the crystal pores.

The optically observed variations in coke formation, as illustrated in Figure 3.2, are fully reflected in the time-resolved UV-Vis absorption measurements taken from a spot in the middle of the H-ZSM-5 crystals. The obtained results are summarized in Figure 3.3.

When analyzing the UV-Vis absorption spectra of the reactions performed at 623 K, that is Figure 3.3 (a), (c), (e), (g), and (i), spectral similarities are obtained among all H-ZSM-5 crystals measured. In line with previous findings this observation confirms that under mild reaction conditions, regardless of the crystal Brønsted acid site density, comparable hydrocarbons are retained within the zeolite.^[5, 41] As methanol reaches the catalytic crystal, the coke build-up starts with the formation of an absorption band at around 400 nm and with time-on-stream, this band undergoes a red shift towards the 420 nm. The 400 nm absorption band has been previously assigned to π - π^* transitions originating from methyl-substituted benzenium cations, which constitute the catalytic scaffold of the HCP mechanism.^[42-51] With the further addition of methanol, an additional absorption band forms around 475 nm. This second absorption band starts as a shoulder of the previously formed 420 nm band and with time-on-stream, it undergoes a red shift towards 500 nm. These observations, combined with previous studies, are reason to assign this additional band to more extended aromatic species. These compounds are most probably formed from the previously mentioned methyl-substituted carbenium ions. However, it must be emphasized that the formation of the 500 nm absorption band does not occur at the expense of the 400 nm absorption band.^[22, 48, 52, 53]

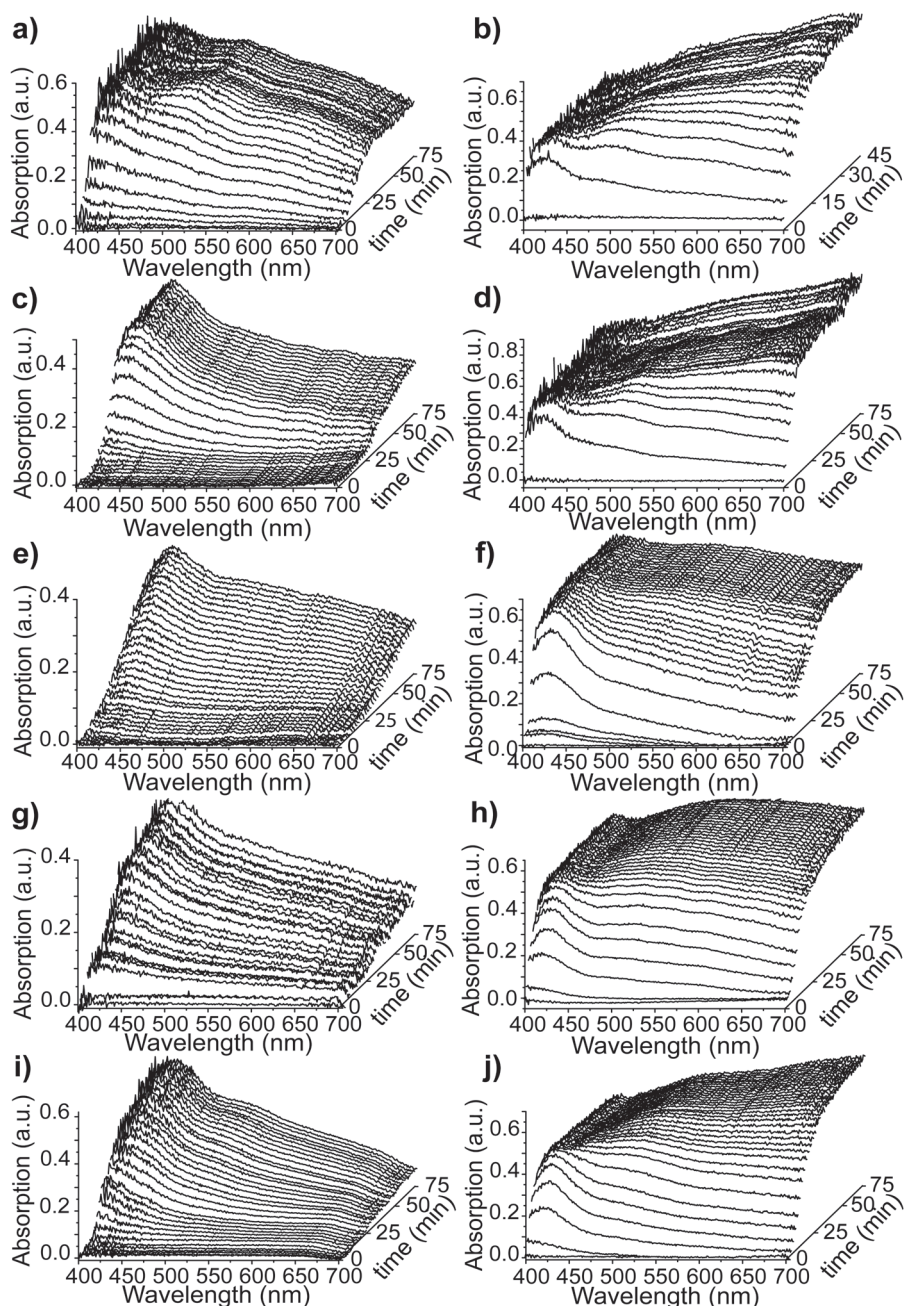


Figure 3.3: UV-Vis absorption spectra of the H-ZSM-5 crystals (A-E) taken during the MTO reaction. (a) A at 623 K, (b) A at 773 K, (c) B at 623 K, (d) B at 773 K, (e) C at 623 K, (f) C at 773 K, (g) D at 623 K, (h) D at 773 K, (i) E at 623 K and (j) E at 773 K. The UV-Vis spectra were taken from a 2 μm spot in the middle of the H-ZSM-5 crystals.

These results point out that at mild reaction conditions, the formation of important HCP compounds and their extended variants is not impeded by morphological constrains. The acidity does not notably affect the nature of the coke species formed although a high acid site density results in a faster formation of the carbonaceous species. These results can be explained by the location of the coke deposition. Hence, the majority of these coke compounds are rather constrained in size and most likely located at the channel intersections where they do not directly affect the available Brønsted acid sites in their conversion practice. Therefore, more available acid sites imply more conversions.^[37, 39, 42, 54-56]

From Figure 3.3 it is observed that the H-ZSM-5 crystals containing the highest Brønsted acid site density (crystal A and to a lesser extent crystal B) additionally show a less apparent absorption band at around 600 nm. This absorption band does not expand towards the 700 nm and becomes less pronounced with decreasing acid site density, where it basically vanishes in the overall absorption that covers the whole visible region. Additionally, for all H-ZSM-5 crystals measured at 623 K, only a limited increase of the overall background absorption is observed. This illustrates that the higher aluminum content facilitates the formation of larger coke species. However, at these temperatures hardly any external graphite-like coke compounds are formed.

Figure 3.3 (b), (d), (f), (h), and (j) illustrates how the fast and pronounced darkening that occurs at elevated temperatures strongly differs from the results obtained during the methanol conversion at mild reaction conditions. In this case, as soon as the methanol stream is opened, the fast formation of carbonaceous species causes several processes to sequentially occur. As the first absorption band at 420 nm is still being formed, the formation of the second absorption band with a maximum at around 500 nm starts as well. Again we assign these two UV-Vis bands to cationic methylated aromatic species and their extended structures that are retained within the H-ZSM-5 crystals. However, under these harsh reaction conditions, the growth of the 500 nm band is subsequently followed by the formation of a third broad band above 600 nm and accompanied with an intense absorption covering the whole visible region. Furthermore, as the 420 nm band reaches a maximum in intensity, the growth of the absorption bands at higher wavelength progresses and eventually exceeds in intensity. This observation is particular for the samples containing a high Brønsted acid site density and to the best of our knowledge no such observation has been reported in the literature. With increasing acidity and higher reaction temperatures, the formation of larger aromatic compounds is evident.^[18, 51, 57, 58] However, the absorption

bands formed above 600 nm cannot be assigned to even more extended aromatic compounds occluded within the microporous network of H-ZSM-5, because the size of the carbonaceous compounds would go beyond the size that is topographically allowed by the H-ZSM-5 crystal structure. Under these reaction conditions, the fast formation of large coke species might induce pore blocking. It is also known that elevated temperatures induce hydrocarbon cracking in H-ZSM-5.^[18, 56, 59] The large compounds retained inside the crystal might therefore break into smaller components. These compounds, together with entering reactants, recombine into polyaromatic species, which as a consequence of the spatial restrictions imposed by the zeolite, direct the formation of carbonaceous deposits towards the zeolite outer surface. Outside the zeolite crystal these species do not experience any size limitations, allowing the formation of large coke molecules. The elevated temperatures consent the formation of graphite-like coke compounds that generate an overall increase of the background absorption.^[28, 60] With decreasing Brønsted acid site density, a reduced formation of large coke compounds is combined with additional lower internal cracking and results in less pronounced external coke. Both external and internal coke compounds may well contain extended forms of π - π^* transitions and the less severe external coke is reflected in reduced absorption intensity at higher wavelengths. Optical microphotographs portrayed in Figure 3.2 confirm this hypothesis by indicating a rather metallic gray coloration for the more acidic samples, which suggests the presence of graphite-type species on the external surface.

Interestingly, when performing the reaction on crystal E, this explanation seems not to stand as the intensity of the red part of the UV-Vis absorption spectrum becomes more pronounced with time-on-stream. However, it must be mentioned that crystal E is by far the largest crystal examined. Therefore, due to diffusion limitations, reactants and products could experience more difficulty to enter or exit the crystal and therefore become more susceptible towards the formation of larger coke species. This assumption is supported by the observation that the UV-Vis band formed at 420 nm, responsible for the active species of the HCP compounds, decreases in intensity after having reached a maximum. It indicates that the formation of methyl-substituted benzene compounds stagnates. Both the internal and external coke materials prevent the access of the methanol feed and the band originating from the catalytic scaffold becomes less intense as cracking and oligomerization processes occur at the expense of these methyl-substituted benzene species.

3.3.2 Deconvolution of the UV-Vis absorption spectra

The large variety of carbonaceous species formed during the MTO reaction is reflected by the overlapping absorption bands in the UV-Vis spectra illustrated in Figure 3.3. In order to elucidate our UV-Vis data in more detail, deconvolution of all spectra as a function of time has been performed for the different H-ZSM-5 crystals. At both reaction temperatures, three major Gaussian functions determined the shape of the UV-Vis absorption spectra. These bands are approximately located at 415, 500 and 590 nm. A representative set of deconvoluted UV-Vis absorption spectra is shown in Figure 3.4 and Table 3.2 summarizes the band position and width of the Gaussian functions obtained for the deconvolution of the spectral data.

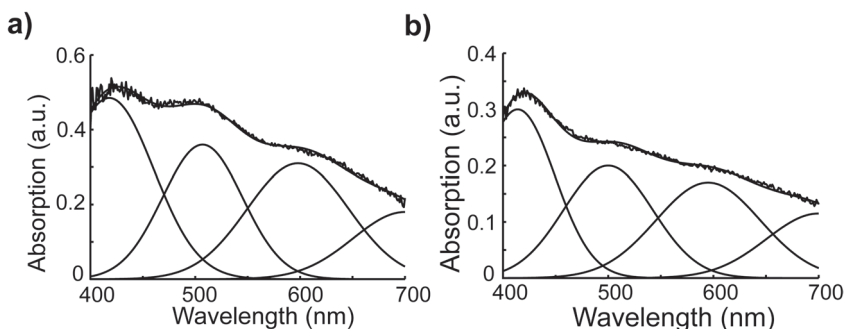


Figure 3.4: Example of the deconvolution procedure applied to the UV-Vis spectra of (a) crystal A at 623 K and (b) crystal C at 623 K.

Table 3.2: Overview of the position of the Gaussian functions used for the deconvolution of the UV-Vis absorption spectra of the H-ZSM-5 crystals (A-E).

Sample	Band position and width (between brackets) of the Gaussians	
	623 K	773 K
A	420 (60), 509 (55), 597 (70)	420 (50), 497 (55), 576 (70)
B	417 (50), 505 (65), 600 (60)	418 (50), 499 (60), 591 (70)
C	414 (50), 500 (60), 595 (70)	410 (55), 496 (70), 593 (70)
D	413 (50), 495 (60), 590 (70)	406 (45), 490 (70), 589 (70)
E	414 (50), 499 (65), 600 (72)	420 (50), 498 (60), 597 (70)

It must be noted that the red shift occurring with time-on-stream has occasionally been challenging to fit. For the sake of accuracy, we always kept a maximum shift of 4 nm if a shift in wavelength had to be applied.

Furthermore, only half of the Gaussian band at 700 nm is used in the calculation and this band is considered to be part of the baseline correction. A selection of the time development of the normalized Gaussian functions is displayed in Figure 3.5 for crystals A, C and E.

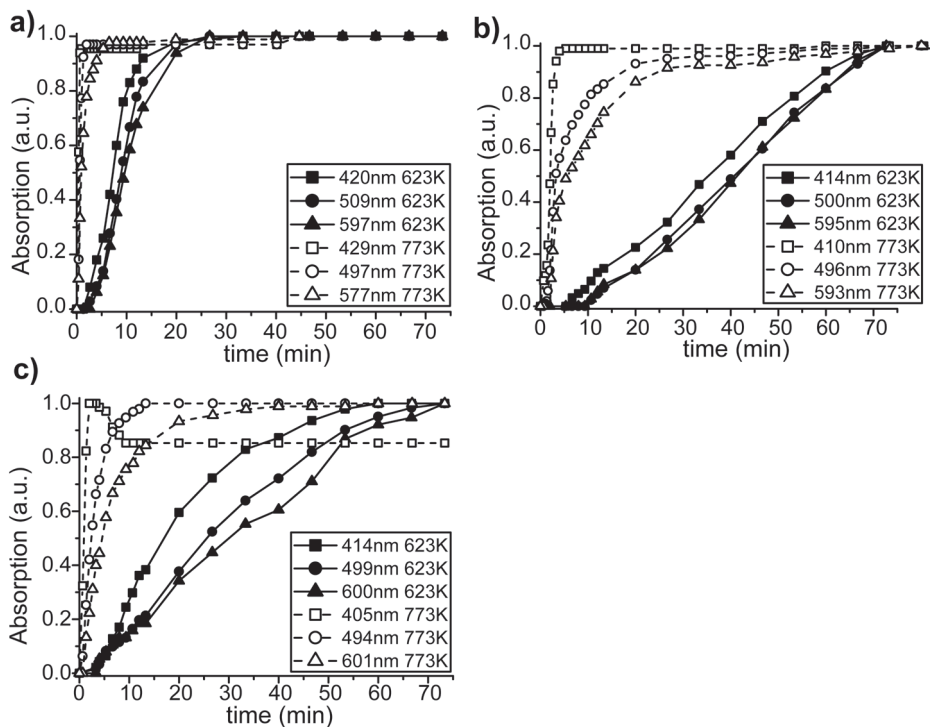


Figure 3.5: Time development of the normalized Gaussian functions for H-ZSM-5 crystals A (a), C (b) and E (c).

The 415 nm absorption band forms first for all H-ZSM-5 crystals measured at 623 K and shortly thereafter the formation of the two remaining absorption bands at around 500 and 600 nm follows. At these mild reaction conditions the band formation starts slow, the absorption bands are formed in consecutive order and their similar slope is considered to be within the experimental error. Curiously, crystals containing a high Brønsted acid site density (i.e., H-ZSM-5 crystal A) reach an intensity maximum with all absorption bands. However, when moving towards less acidic H-ZSM-5 crystals (Figure 3.5 (b) and (c)) no apparent maximum is observed by the time the reaction is stopped. This observation indicates that despite the low temperatures applied, the Brønsted acid site density does affect the formation of the coke species and coke saturation occurs for the most acidic H-ZSM-5 crystals.

At a reaction temperature of 773 K the situation clearly differs. First, the formation of all absorption bands starts almost instantly as methanol vapor enters the reactor. Second, all absorption bands reach an intensity maximum, including the H-ZSM-5 crystals containing a low Brønsted acid site density. Third, two separate coke stages are observed. One is reflected at a high Brønsted acid site density, where the absorption band at around 415 nm is rapidly followed by the absorption bands formed at 500 nm and 590 nm. It represents the fast formation of larger coke species following the formation of the methylated mono-aromatic compounds. Under mild reaction conditions, the coke formation has limited effect on the accessible acid sites. The faster rate of formation, as temperature is raised, however, cause more pore blockage. With decreasing Brønsted acid site density, this rapid growth of the absorption bands at higher wavelengths gradually decreases. Here, the formation of larger coke species slows down, pore blockages diminish and a change in coke formation pattern becomes evident.^[51, 54, 57, 61] Studies indicated that the crystal framework that surrounds the HCP active species influences the fundamental reaction kinetics of the conversion. Here, crucial parameters like framework topology and composition are strongly combined with the size, shape and orientation of the hydrocarbons formed.^[8, 14, 21, 62] By increasing the aluminum concentration in the framework composition, the total Brønsted acid site density of the H-ZSM-5 crystal increases. The strength of the individual acid sites, however, decreases when these are less isolated; a phenomenon known as next nearest neighbor. Calculations on the aluminum topological density showed that the maximum in effective acidity obtained in H-ZSM-5 is around a Si/Al molar ratio of 9.5.^[63-66] Interestingly however, in the case of H-ZSM-5, reports suggest that the difference in acid site density does not noticeably affect the overall Brønsted acid strength and the thereby linked crystal activity only depends on the number of available acid sites.^[55, 66-68] Our findings show that a higher Brønsted acid site density does not produce noticeably different coke species, but it does increase the rate of formation of the methyl-substituted aromatic species and the subsequent growth towards larger coke species. This effect is even more enhanced as temperature is raised, most likely due to a higher diffusion rate.

Since more acid sites translate in more conversion, we can relate the absorption to the concentration in an attempt to compare the effective rate constant between the different samples. For this reason, the time-development of the obtained Gaussian functions was fitted to first order kinetics. From the fitting curves, we can determine the rate constants and plot them as a function of the Si/Al molar ratio of the zeolite crystals under

study. The results are shown in Figure 3.6. The effective rate constants for the formation of the three absorption bands at around 400, 500 and 600 nm, show a clear maximum for the samples containing the highest Brønsted acid site density and the k values decrease with decreasing acidity. More precisely, the k values obtained above a Si/Al molar ratio of 17 are rather similar. This indicates that below a certain aluminum concentration in the zeolite material the acid site density has a limited influence on the coke formation rate; a finding that interestingly is valid for both temperatures. The formation of methyl-substituted aromatic species and their growth towards larger compounds depend on available reactants and vacant acid sites. In this line of thinking, it is possible to assume that as the Brønsted acid site density decreases uniformly, the distance between the individual acid sites increases and consequently reduces the chance of conversion towards more extended coke compounds. However, the relatively similar magnitudes of the k values obtained at low reaction temperatures indicate that despite the overall Brønsted acid site density the temperature largely influences the formation rate. An increased diffusion speed of reactants combined with more internal hydrocarbon cracking eventually results in a larger amount of available reactants that, as a consequence, results in the formation of large coke species even at high Si/Al molar ratio.

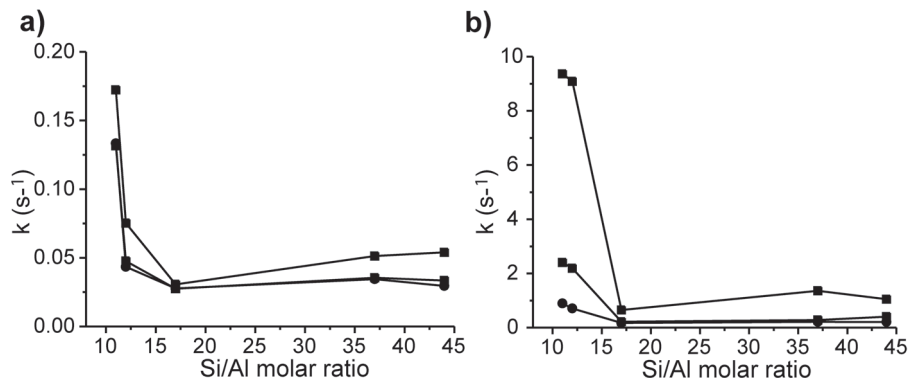
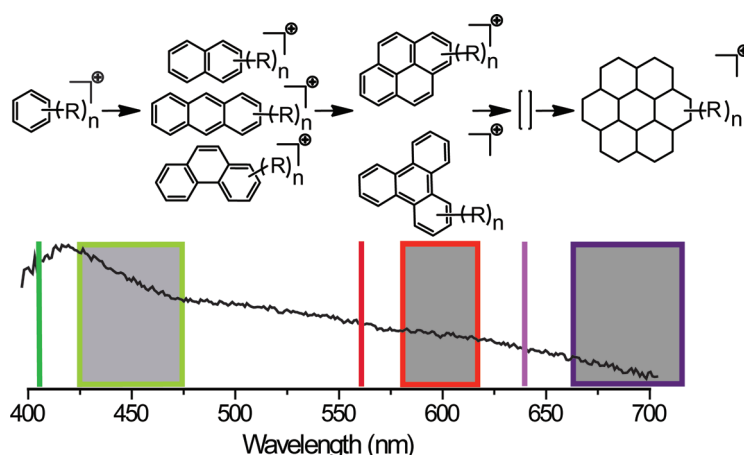


Figure 3.6: Effective reaction rate constant of the coke formed on H-ZSM-5 crystals as a function of the Si/Al molar ratio: (a) 623 K and (b) 773 K for 400 nm (■), 500 nm (□) and 600 nm (●).

The observations made so far invite us to discuss the mode of coke formation. The build-up of the coke species starts with the formation of the methyl-substituted benzene carbocations. These compounds subsequently evolve, with the further addition of methanol, into linear poly-aromatic coke species, located in the channels of H-ZSM-5.^[68-70]

Above 673 K, up to pyrene-like structures can be formed in the H-ZSM-5 zeolite channels.^[41, 54, 62, 70-73] Especially at high reaction temperature, the further addition of reactants causes these compounds to grow in the direction of the crystal outer surface where the poly-aromatic structure loses spatial restrictions and forms compounds with a more graphite-like character. This gradual transformation process is illustrated in Scheme 3.1.



Scheme 3.1: Proposed coke formation process taking place during the MTO conversion over H-ZSM-5 zeolites. The process occurs within and at the outer surface of H-ZSM-5 zeolite crystals. The displayed laser excitation lines (405 nm, 561 nm and 637 nm) with their corresponding detection regions (425-475 nm; 565-635 nm; and 662-737 nm) indicate the distinctive UV-Vis detectable coke species revealed with each laser wavelength when applied in the confocal fluorescence microscopy experiments.

3.3.3 Confocal fluorescence microscopy

Confocal fluorescence microscopy allows the detection of fluorescent coke species and their precursors within the volume of large H-ZSM-5 crystals.^[29] Furthermore, as coke species grow, their light absorption at higher wavelengths becomes more pronounced. Consistent with this line of thinking, longer excitation wavelengths excite more-extended coke compounds, as shown in Scheme 3.1. Therefore, a set of novel confocal fluorescence microscopy experiments has been performed in which multiple laser excitation wavelengths have been applied to discriminate between the different coke species formed within an individual H-ZSM-5 crystal. Figure 3.7 shows the results obtained after 2 min of methanol conversion over crystal C performed at both 623 and 773 K.

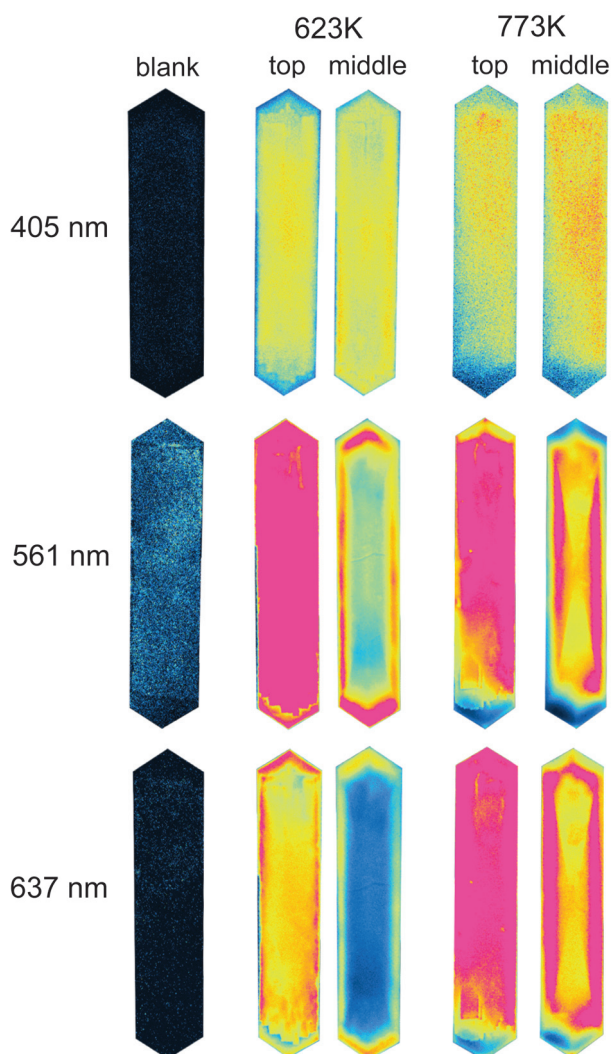


Figure 3.7: Confocal fluorescence microscopy images of the H-ZSM-5 crystal after two minutes of MTO conversion at 623 K and 773 K. The samples are measured at the top and middle focal plane through the crystal body. The applied laser excitation wavelengths are 405 nm (425-475 nm detection region), 561 nm (570-620 nm detection region) and 637 nm (662-737 nm detection region). The images are shown in false color (intensity profile) and minor adjustments in the saturation level have been made to decrease the overexposure level.

During these experiments, three separate excitation wavelengths have been applied. The 405 nm with detection region of 425-475 nm, the 561 nm has

a detection region at 570-620 nm and 637 nm with the detection region at 662-737 nm. None of the wavelengths shows fluorescence before the introduction of the methanol flow into the in-situ cell as illustrated by the blank micrographs in Figure 3.7. The 405 nm excitation wavelength detects mainly small aromatic coke species that form firstly as the MTO conversion is started (Scheme 3.1). The slow formation, occurring at 623 K, gradually generates these small compounds throughout the entire crystal and both the top and middle of the zeolite crystal contain these fluorescent species. When moving towards the 561 nm excitation wavelength, hence the detection of larger coke species (Scheme 3.1), an inhomogeneous fluorescence pattern become visible. The majority of the fluorescent species are located near the crystal surface and the delicate revelation of the characteristic hour-glass pattern indicates that diffusion limitations or channel mismatch between the different subunits slightly hinders the formation of these larger coke compounds in the crystal core. Similar observations are made for the more extended coke species excited with the 637 nm line (Scheme 3.1). The lower fluorescence intensity point out that less fluorescent material is detected, which is reasonable if one considers the mild reaction conditions and the limited reaction time. However, it is striking to observe that these fluorescent species are detected in a more confined space at the surface of the crystal compared to the coke species detected with the 561 nm laser light.

The same experiment performed at 773 K revealed many similarities to the previously described experiment at 623 K. However, a higher reaction temperature results in the faster and more pronounced formation of large coke species. This is reflected in the more dominant fluorescence intensities for the laser excitation at 637 nm because more extended conjugated coke species resulted to be present. Contrary to previous observations made at 623 K, these extended coke species, detected with the 637 nm laser light, were located in a thicker layer covering the H-ZSM-5 crystal surface and diffusion limitation resulted in the evident hour-glass pattern. The results are in agreement with previous findings where both optical microphotographs and UV-Vis absorption measurements indicate the progressing darkening of the crystal that is dominant at the crystal edge and causing an increasing UV-Vis absorption above 600 nm.

3.3.4 Polarization dependent in-situ UV-Vis micro-spectroscopy

In a separate set of experiments, the gradual formation of carbonaceous deposits was examined by applying polarization dependent UV-Vis micro-spectroscopy. Previous studies indicated that the use of optical absorption measurements with polarized light enabled UV-Vis absorbing species to

be visualized. These species were aligned within the straight channels of zeolite H-ZSM-5.^[29, 74] For this reason, the MTO conversion on crystal C was performed at 623 and 773 K. During this, a horizontal (along the straight channels) and a vertical (perpendicular to the straight channels) orientation of the polarizer in respect to the examined zeolite crystal were applied. The microphotographs of crystal C taken after 20 min of reaction with the corresponding orientation are presented in Figure 3.8.

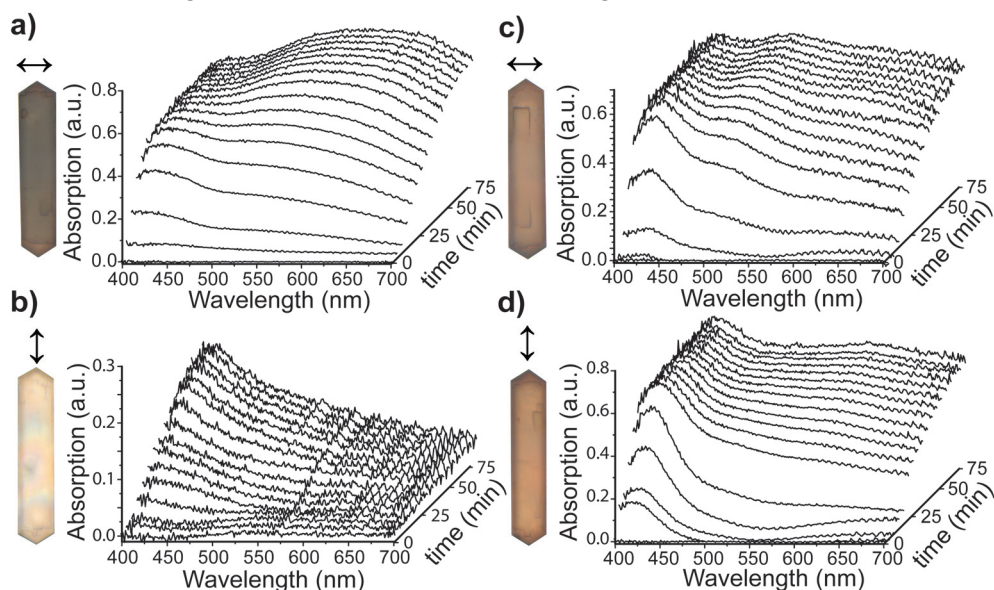


Figure 3.8: In-situ polarization dependent UV-Vis absorption spectra obtained from the H-ZSM-5 crystal during MTO conversion at 623 K (a and b) and 773 K (c and d). Microphotographs of the crystal after 20 min of reaction with the corresponding polarization direction (indicated by the arrow) are included.

One can observe a strong coloration when the polarization light coincides with the alignment of the large straight pores, whereas a 90° rotation results in a remarkable lighter crystal; a phenomenon that is especially clear for MTO reactions performed at mild reaction conditions. This finding illustrates the macroscopic alignment of the carbocationic coke molecules along the short axis of the zeolite crystal.

The corresponding time-resolved UV-Vis spectra measured from a spot in the middle of the crystal mirror these observations. In case of a horizontal polarization alignment (Figure 3.8a and c) the formation of the UV-Vis bands at 500 nm and 600 nm is characteristic. Since these bands are assigned to the π - π^* transitions of large coke molecules, their pronounced formation in this alignment indicates their presence in the large straight pores of the zeolite

crystal. A 90° rotation of the polarizer (Figure 3.8b and d) however results in a remarkable different UV-Vis spectrum. Here, large coke molecules no longer provide a prominent contribution to the overall absorption spectrum and the 420 nm band, originating from smaller methyl-substituted aromatic species, is dominant. With this vertical polarization, the lack of alignment with the straight channels introduces a larger contribution of the smaller sinusoidal channels. At higher temperatures, the conversion of these small molecules towards larger deactivating coke compounds increases. The use of polarized light confirms this and additionally indicates that the faster conversion of small species pushes the larger conformations to form towards the channel intersections and the zeolite outer surface, as illustrated by the 500 and 600 nm UV-Vis bands at higher reaction temperatures for the vertical alignment. However, a pronounced 420 nm UV-Vis band strongly indicates that large coke species mostly build up in the straight pores of H-ZSM-5 crystals.

3.4 Conclusions

The Methanol-to-Olefin conversion suffers from deactivation by carbonaceous deposits. The application of in-situ UV-Vis and confocal fluorescence microscopy provides detailed insights in the coke formation processes on individual H-ZSM-5 crystals varying in their Brønsted acid site density. The aluminum concentration, as represented by the Si/Al molar ratio, proved to influence the deactivation characteristics of the catalyst material.

UV-Vis micro-spectroscopy measurements indicate that under mild reaction conditions, the formed coke species predominantly consist of methyl-substituted aromatic compounds located in the H-ZSM-5 crystal. At these low reaction temperatures, the Brønsted acid site density does not affect the chemical nature of the formed coke species. However, with increasing available acid sites, the formation of the coke compounds occurs faster and the growth of these compounds into extended linear aromatics is facilitated. Higher reaction temperature causes the fast formation of larger aromatic species, independently of the Brønsted acid site density. Furthermore, under these reaction conditions, larger graphite-like coke deposits form at the external surface of the catalysts, especially for the most acidic crystals.

Analysis of the UV-Vis absorption measurements shows that mild reaction conditions cause similar absorption band formation rates, whereas increasing the reaction temperature induce an enhanced rate of coke formation for the more acidic crystals. Here, deconvolution analysis of the UV-Vis spectra indicates that above a Si/Al molar ratio of 17, the rate formation constants of all coke types is within the experimental error and the reaction temperature

becomes the dominant parameter. The results are explained in terms of formation of large aromatic species that cause pore blockage and outer-surface coverage. The coke formation starts with the build-up of the methyl-substituted benzenium species. The further addition of reactants and the presence of Brønsted acid sites cause these compounds to grow, which results in the formation of linear aromatic compounds. As a consequence, pore blockage occurs and the addition of reactants combined with internal cracking at high temperatures leads to the formation of large coke species towards the external crystal surface where lack of size restrictions allows the formation of graphite-like compounds.

The combination of multiple laser excitation wavelengths with confocal fluorescence microscopy allows the spatially-resolved visualization of coke species with distinctive dimensions. The small methylated aromatic compounds spread uniformly over the entire zeolite crystal. More-extended aromatic compounds, however, predominantly form near the crystal surface. Increasing reaction temperature enhances this process. Finally, time-resolved UV-Vis micro-spectroscopy with polarized light illustrates that the majority of the large coke species build up within the straight zeolite pores.

Acknowledgements

Dr. Machteld Mertens (ExxonMobil, Belgium) is acknowledged for providing ZSM-5 crystal C. Dr. Jan Kornatowski (Max Planck Institut, Germany) is acknowledged for providing ZSM-5 crystal A, B, D and E. Prof. Unni Olsbye is thanked for fruitful discussions. Sander de Brouwer is thanked for his participation in the project. Dr. Eli Stavitski is acknowledged for writing the deconvolution analysis software. Marjan Versluijs-Helder is acknowledged for performing the SEM-EDX measurements.

References

- [1] J. L. G. Fierro, *Catal. Lett.* **1993**, 22, 67-91.
- [2] M. Stöcker, *Microporous Mesoporous Mater.* **1999**, 29, 3-48.
- [3] H. van Bekkum, E.M. Flanigen, P.A. Jacobs, J.C. Jansen (Eds.), *Introduction to Zeolite Science and Practice*, Elsevier, Amsterdam, **2001**.
- [4] H. van Bekkum, F. Bauer (Eds.), *Molecular Sieves*, Springer-Verlag, Berlin Heidelberg, **2007**.
- [5] M. Bjorgen, S. Akyalcin, U. Olsbye, S. Benard, S. Kolboe, S. Svelle, *J. Catal.* **2010**, 275, 170-180.
- [6] D. Lesthaeghe, V. Van Speybroeck, G. B. Marin, M. Waroquier, *Ind. Eng. Chem. Res.* **2007**, 46, 8832-8838.

- [7] D. Lesthaeghe, A. Horre, M. Waroquier, G. B. Marin, V. Van Speybroeck, *Chem. Eur. J.* **2009**, 15, 10803-10808.
- [8] D. Lesthaeghe, J. Van der Mynsbrugge, M. Vandichel, M. Waroquier, V. Van Speybroeck, *ChemCatChem*. **2011**, 3, 208-212.
- [9] M. Bjorgen, F. Joensen, K. P. Lillerud, U. Olsbye, S. Svelle, *Catal. Today* **2009**, 142, 90-97.
- [10] M. Bjorgen, S. Svelle, F. Joensen, J. Nerlov, S. Kolboe, F. Bonino, L. Palumbo, S. Bordiga, U. Olsbye, *J. Catal.* **2007**, 249, 195-207.
- [11] J. F. Haw, W. G. Song, D. M. Marcus, J. B. Nicholas, *Acc. Chem. Res.* **2003**, 36, 317-326.
- [12] U. Olsbye, M. Bjorgen, S. Svelle, K. P. Lillerud, S. Kolboe, *Catal. Today* **2005**, 106, 108-111.
- [13] S. Svelle, F. Joensen, J. Nerlov, U. Olsbye, K. P. Lillerud, S. Kolboe, M. Bjorgen, *J. Am. Chem. Soc.* **2006**, 128, 14770-14771.
- [14] J. F. Haw, D. M. Marcus, *Top. Catal.* **2005**, 34, 41-48.
- [15] J. Li, G. Xiong, Z. Feng, Z. Liu, Q. Xin, C. Li, *Microporous Mesoporous Mater.* **2000**, 39, 275-280.
- [16] D. Lesthaeghe, V. Van Speybroeck, M. Waroquier, *Phys. Chem. Chem. Phys.* **2009**, 11, 5222-5226.
- [17] D. M. Bibby, R. F. Howe, G. D. Mclellan, *Appl. Catal. A* **1992**, 93, 1-34.
- [18] D. M. Bibby, N. B. Milestone, J. Patterson, L. P. Aldridge, *J. Catal.* **1986**, 97, 493-502
- [19] C. D. Chang, A. J. Silvestri, *J. Catal.* **1977**, 47, 249-259.
- [20] B. P. C. Hereijgers, F. Bleken, M. H. Nilsen, S. Svelle, K. P. Lillerud, M. Bjorgen, B. M. Weckhuysen, U. Olsbye, *J. Catal.* **2009**, 264, 77-87.
- [21] K. Hemelsoet, A. Nollet, M. Vandichel, D. Lesthaeghe, V. Van Speybroeck, M. Waroquier, *ChemCatChem*. **2009**, 1, 373-378.
- [22] H. Schulz, *Catal. Today* **2010**, 154, 183-194.
- [23] L. Travalloni, A. C. L. Gomes, A. B. Gaspar, M. A. P. da Silva, *Catal. Today* **2008**, 133, 406-412.
- [24] W. J. H. Dehertog, G. F. Froment, *Appl. Catal.* **1991**, 71, 153-165.
- [25] B. M. Weckhuysen, *Angew. Chem. Int. Ed.* **2009**, 48, 4910-4943.
- [26] L. Sommer, D. Mores, S. Svelle, M. Stöcker, B. M. Weckhuysen, U. Olsbye, *Microporous Mesoporous Mater.* **2010**, 132, 384-394.
- [27] A. N. Parvulescu, D. Mores, E. Stavitski, C. M. Teodorescu, P. C. A. Bruijninx, R. J. M. K. Gebbink, B. M. Weckhuysen, *J. Am. Chem. Soc.* **2010**, 132, 10429-10439.
- [28] D. Mores, E. Stavitski, M. H. F. Kox, J. Kornatowski, U. Olsbye, B. M. Weckhuysen, *Chem. Eur. J.* **2008**, 14, 11320-11327.
- [29] E. Stavitski, M. H. F. Kox, B. M. Weckhuysen, *Chem. Eur. J.* **2007**, 13, 7057-7065.
- [30] L. Karwacki, M. H. F. Kox, D. A. M. de Winter, M. R. Drury, J. D. Meeldijk, E. Stavitski, W. Schmidt, M. Mertens, P. Cubillas, N. John, A. Chan, N. Kahn, S. R. Bare, M. Anderson, J. Kornatowski, B. M. Weckhuysen, *Nature Mater.* **2009**, 8, 959-965.
- [31] L. Karwacki, E. Stavitski, M. H. F. Kox, J. Kornatowski, B. M. Weckhuysen, *Angew. Chem. Int. Ed.* **2007**, 46, 7228-7231.

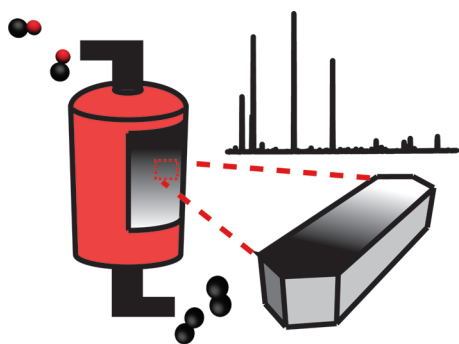
- [32] L. Karwacki, H. E. van der Bij, J. Kornatowski, P. Cubillas, M. R. Drury, D. A. M. de Winter, M. W. Anderson, B. M. Weckhuysen, *Angew. Chem. Int. Ed.* **2010**, 49, 6790-6794.
- [33] L. Karwacki, B. M. Weckhuysen, *Phys. Chem. Chem. Phys.* **2011**, 13, 3681-3685.
- [34] M. H. F. Kox, E. Stavitski, J. C. Groen, J. Perez-Ramirez, F. Kapteijn, B. M. Weckhuysen, *Chem. Eur. J.* **2008**, 14, 1718-1725.
- [35] E. Stavitski, M. R. Drury, D. A. M. de Winter, M. H. F. Kox, B. M. Weckhuysen, *Angew. Chem. Int. Ed.* **2008**, 47, 5637-5640.
- [36] P. Sazama, J. Dedecek, V. Gabova, B. Wichterlova, G. Spoto, S. Bordiga, *J. Catal.* **2008**, 254, 180-189.
- [37] P. L. Benito, A. G. Gayubo, A. T. Aguayo, M. Olazar, J. Bilbao, *J. Chem. Technol. Biotechnol.* **1996**, 66, 183-191.
- [38] F. Bleken, M. Bjorgen, L. Palumbo, S. Bordiga, S. Svelle, K. P. Lillerud, U. Olsbye, *Top. Catal.* **2009**, 52, 218-228.
- [39] D.B. Luk'yanov, *Zeolites* **1992**, 12, 287-288.
- [40] J. Huang, Y. J. Jiang, V. R. R. Marthala, A. Bressel, J. Frey, M. Hunger, *J. Catal.* **2009**, 263, 277-283.
- [41] M. Guisnet, P. Magnoux, *Appl. Catal. A* **2001**, 212, 83-96.
- [42] L. Palumbo, F. Bonino, P. Beato, M. Bjorgen, A. Zecchina, S. Bordiga, *J. Phys. Chem. C* **2008**, 112, 9710-9716.
- [43] G. Spoto, F. Geobaldo, S. Bordiga, C. Lamberti, D. Scarano, A. Zecchina, *Top. Catal.* **1999**, 8, 279-292.
- [44] S. Svelle, M. Bjorgen, S. Kolboe, D. Kuck, M. Letzel, U. Olsbye, O. Sekiguchi, E. Uggerud, *Catal. Lett.* **2006**, 109, 25-35.
- [45] B. Arstad, S. Kolboe, O. Swang, *J. Phys. Chem. B* **2002**, 106, 12722-12726.
- [46] B. Arstad, J. B. Nicholas, J. F. Haw, *J. Am. Chem. Soc.* **2004**, 126, 2991-3001.
- [47] B. Arstad, S. Kolboe, O. Swang, *J. Phys. Chem. A* **2005**, 109, 8914-8922.
- [48] M. Bjorgen, F. Bonino, S. Kolboe, K. P. Lillerud, A. Zecchina, S. Bordiga, *J. Am. Chem. Soc.* **2003**, 125, 15863-15868.
- [49] I. Kiricsi, G. Tasi, H. Forster, P. Fejes, *J. Mol. Struct.* **1990**, 218, 369-374.
- [50] I. Kiricsi, H. Forster, G. Tasi, J. B. Nagy, *Chem. Rev.* **1999**, 99, 2085-2114.
- [51] R. H. Meinhold, D. M. Bibby, *Zeolites* **1990**, 10, 121-130.
- [52] S. Svelle, U. Olsbye, K. P. Lillerud, S. Kolboe, M. Bjorgen, *J. Am. Chem. Soc.* **2006**, 128, 5618-5619.
- [53] G. F. Froment, J. Demeyer, E. G. Derouane, *J. Catal.* **1990**, 124, 391-400.
- [54] P. L. Benito, A. G. Gayubo, A. T. Aguayo, M. Olazar, J. Bilbao, *Ind. Eng. Chem. Res.* **1996**, 35, 3991-3998.
- [55] A. G. Gayubo, P. L. Benito, A. T. Aguayo, M. Olazar, J. Bilbao, *J. Chem. Technol. Biotechnol.* **1996**, 65, 186-192.
- [56] A. T. Aguayo, A. G. Gayubo, R. Vivanco, M. Olazar, J. Bilbao, *Appl. Catal. A* **2005**, 283, 197-207.
- [57] R. H. Meinhold, D. M. Bibby, *Zeolites* **1990**, 10, 146-150.

- [58] L. Jansen van Rensburg, R. Hunter, G. J. Hutchings, *Appl. Catal.* **1988**, 42, 29-34.
- [59] N. Y. Topsoe, K. Pedersen, E. G. Derouane, *J. Catal.* **1981**, 70, 41-52.
- [60] J. M. Lopes, F. Lemos, F. R. Ribeiro, E. G. Derouane, P. Magnoux, M. Guisnet, *Appl. Catal. A* **1994**, 114, 161-172.
- [61] D. M. McCann, D. Lesthaeghe, P. W. Kletnieks, D. R. Guenther, M. J. Hayman, V. Van Speybroeck, M. Waroquier, J. F. Haw, *Angew. Chem. Int. Ed.* **2008**, 47, 5179-5182.
- [62] M. Guisnet, P. Magnoux, *Appl. Catal.* **1989**, 54, 1-27.
- [63] R. Beaumont, D. Barthomeuf, *J. Catal.* **1972**, 26, 218-225.
- [64] D. Barthomeuf, *Mater. Chem. Phys.* **1987**, 17, 49-71.
- [65] R. J. Mikovsky, J. F. Marshall, *J. Catal.* **1976**, 44, 170-173.
- [66] H. S. Cerqueira, P. C. Mihindou-Koumba, P. Magnoux, M. Guisnet, *Ind. Eng. Chem. Res.* **2001**, 40, 1032-1041.
- [67] P. C. Mihindou-Koumba, H. S. Cerqueira, P. Magnoux, M. Guisnet, *Ind. Eng. Chem. Res.* **2001**, 40, 1042-1051.
- [68] F. F. Madeira, N. S. Gnep, P. Magnoux, H. Vezin, S. Maury, N. Cadran, *Chem. Eng. J.* **2010**, 161, 403-408.
- [69] P. Magnoux, H. S. Cerqueira, M. Guisnet, *Appl. Catal. A* **2002**, 235, 93-99.
- [70] M. Hureau, A. Moissette, S. Marquis, C. Bremard, H. Vezin, *Phys. Chem. Chem. Phys.* **2009**, 11, 6299-307.
- [71] M. Guisnet, N. S. Gnep, D. Aittaleb, Y. J. Doyemet, *Appl. Catal. A* **1992**, 87, 255-270.
- [72] F. Bauer, W. H. Chen, E. Biiz, A. Freyer, V. Sauerland, S. B. Liu, *J. Catal.* **2007**, 251, 258-270.
- [73] A. O. E. Beyne, G. F. Froment, *Chem. Eng. J.* **2001**, 82, 281-290.
- [74] F. Marlow, K. Hoffmann, G. G. Lindner, I. Girnus, G. van de Goor, J. Kornatowski, J. Caro, *Micropor. Mater.* **1996**, 6, 43-49.

Chapter 4

Catalytic Performance of Micron-sized H-ZSM-5 Zeolite Crystals during Methanol-to-Olefin Conversion

Bridging the Gap between Single Particle Examination and Bulk Catalyst Analysis



The bulk catalytic properties of large coffin-shaped H-ZSM-5 zeolites are investigated with on-line GC effluent analysis of a fixed-bed reactor and the GC-MS examination of coke material retained within the crystals. These findings are related to observations made at the individual particle level using UV-Vis micro spectroscopy.

4.1 Introduction

Zeolites are commonly used catalysts applied in a variety of commercial processes. The catalytic activity of these materials is caused by the presence of acid sites, while their well-defined microporous network provides unique size and shape selectivity.^[1-4] Due to these intrinsic properties, the application of zeolite and zeotype materials in Gas-to-Liquid (GTL) conversions is noted. The transformation of methanol into hydrocarbons is such conversion process that, depending on the catalyst choice and applied reaction conditions, gives variable product selectivity.^[5, 6]

The Methanol-to-Olefin (MTO) conversion is an important GTL-branch that mainly provides light alkenes. H-ZSM-5 is a well-known catalyst for this conversion. The reaction proceeds via the hydrocarbon pool (HCP) mechanism, albeit combined with alkene methylations and hydrocarbon cracking. Here, methyl substituted aromatic species, retained in the catalyst pores, are the active reaction intermediates. To these compounds, methanol is added and olefins are formed in a closed catalytic cycle.^[7-14] As a result of the HCP mechanism and secondary reactions thereof, the formation of carbonaceous deposits can occur.^[15] These large hydrocarbons are retained within the catalyst porous network where they can cause pore blockage, thereby affecting the diffusion of reactants and products throughout the catalyst particle. Also poisoning of the zeolite active sites, by adsorption of undesired species, can influence the catalyst activity. As a result, the catalyst conversion may change during operation.^[16-22]

By varying the zeolite acid site density, the creation of mesopores and the introduction of surface modifications, this detrimental coke formation process can be suppressed. The removal of undesired coke deposits is furthermore an often applied catalyst regeneration procedure. This practice requires an oxidative treatment of the catalyst material at high temperatures.^[23-27] However, besides burning off the carbonaceous compounds, the severe reaction conditions can also affect the zeolite properties. Catalyst regeneration can for example cause dealumination and degradation of the zeolite framework with consequences for the catalyst performance.^[28-30]

Many efforts focus on the development of catalysts and processes that diminish the undesired coke formation.^[31-33] For advancement in this field of research, further understanding of the coke formation process, the chemical composition of the carbonaceous species and their location within a catalyst particle is essential. A large variety of analytical techniques have been developed to address these issues.^[34-40] Previous Chapters illustrated how the use of in-situ micro-spectroscopic techniques can be valuable to study coke formation processes in a space- and time-resolved manner at the individual

catalyst particle level.^[41-46] These tools use an in-situ micro-spectroscopy cell and are mainly applied on large model zeolites of several microns. These crystal sizes do not directly correspond to industrially used catalyst materials, but is required to overcome diffraction limitation constrains imposed by the microscopic techniques. Parallel to this, GC-MS based online fixed-bed reactor effluent analysis with subsequent offline analysis of the retained material has proven to provide essential details on the chemical nature of the formed hydrocarbons and their influence on the catalytic conversion.^[13, 47-50] In this work, we apply GC for the on-line analysis of a fixed-bed reactor effluent and perform GC-MS on the organic species that are retained in the large H-ZSM-5 zeolite crystals after methanol conversion. These studies are performed on bulk samples and therefore provide information that is an ensemble average over a large set of micron-sized H-ZSM-5 crystals. The same conversions are performed in an in-situ micro-spectroscopy cell, while monitored with UV-Vis micro-spectroscopy that permits the visualization of the coke formation at the individual catalyst particle level. The combination of these two analytical approaches allows comprehending the activity, selectivity and coke formation of the large coffin-shaped H-ZSM-5 zeolites during MTO conversion and to link the bulk catalyst characterization results with spectroscopic observations made on individual catalyst particles.

4.2 Experimental

4.2.1 Methods

UV-Vis micro-spectroscopy

The research was performed using the upright research microscope Olympus BX41, equipped with a 50x0.5 NA-high working distance objective.^[55] The set-up additionally has a 50/50 double viewport tube that accommodates the CCD video camera (ColorView Illu, Soft Imaging System GmbH) and an optical fibre mount. A 200 μm -core fibre connects the microscope to a CCD UV/Vis spectrometer (AvaSpec-2048TEC, Avantes).

In-situ cell

The experiments were performed on a Linkam FTIR 600 in-situ cell equipped with temperature controller (Linkam TMS93). The zeolite crystals were heated to 773 K at a rate of 10 $\text{K}\cdot\text{min}^{-1}$ and kept at this temperature under inert atmosphere with N_2 for 1 h after which the temperature was brought to the desired reaction temperature with a rate of 10 $\text{K}\cdot\text{min}^{-1}$. Subsequently, the N_2 flow (70 $\text{ml}\cdot\text{min}^{-1}$) was diverted through a bubbler containing the methanol thereby acting as a carrier gas.

On-line effluent analysis

Catalyst tests (coking) were performed without pressing and sieving the zeolite crystals and 30 mg of the catalyst was used for each experiment. The reaction products were analyzed using an online GC connected to the outlet of a fixed bed reactor (i.d. 10 mm) using a heated transfer line. The inlet of the reactor was connected to a He carrier gas, which was bubbled through a methanol solution and kept at 293 K ($P_{\text{MeOH}} = 130$ mbar) in a saturation evaporator ($\text{WHSV} = 5.56 \text{ gg}^{-1}\cdot\text{h}^{-1}$). The first GC analysis of the effluent product was performed after 5 min on stream. Details on the experimental procedure have been reported in literature.^{49, 50}

Off-line analysis of the retained species

The retained species in the pores of the catalyst were liberated and analyzed using a standard HF dissolution procedure.^{12, 49} In short, 15 mg of the aged (coked) catalyst was dissolved in a Teflon liner using 1 ml of 15 % HF. The liberated organics were extracted using dichloromethane (CH_2Cl_2) having hexachloroethane (C_2Cl_6) as an internal standard. The organic extracts were transferred into a glass vial and analyzed using GC-MS as described in literature.⁴⁷

Catalyst regeneration

The coked catalyst was heated to the regeneration temperature (773 K) under a flow of He (40 ml/min). The catalyst was kept at 773 K for ~ 11 h under the flow of O_2 and He (1 h under 5 % O_2 in He, 1 h under 10 % O_2 in He, 1 h under 20 % O_2 in He, 8 h under 50 % O_2 in He). The flow rate of He was kept constant ($40 \text{ ml}\cdot\text{min}^{-1}$) during regeneration.

4.2.2 Materials

The micron-sized H-ZSM-5 crystallites are provided by ExxonMobil (Machelen, Belgium) and have $100 \times 20 \times 20 \text{ }\mu\text{m}$ dimensions with a Si/Al ratio of ~ 17 as determined by synthesis protocol and SEM-EDX measurements.⁵¹⁻⁵⁴ Methanol (99 %, Antonides Interchema) was used as received.

4.3 Results and discussion

4.3.1 Activity and selectivity

The HCP mechanism and secondary reactions associated to it result in the formation of undesired coke deposits during the conversion of methanol into hydrocarbons.^[15, 17, 22] It has been shown that the mode of coke formation and the chemical nature of these carbonaceous species strongly depend on parameters, such as zeolite composition and applied reaction

conditions.^[56-58] These studies are mainly performed on small zeolite crystals of a few micrometers. In addition to these findings, experiments performed on large model H-ZSM-5 zeolites provided spatiotemporal spectroscopic insights on the coke formation process during the MTO conversion in individual H-ZSM-5 zeolite crystals.^[41, 42, 44, 45] However, the in-situ micro-spectroscopic set-up used for the single particle analysis does not allow the examination of the catalytic properties of these large micron-sized catalysts. The large crystal dimensions could affect the activity and selectivity properties that, as a consequence, could deviate from the industrially applied catalysts with smaller crystal dimensions. Therefore, a set of experiments, equivalent to the traditional bulk measurements have been performed with the purpose to assess the catalytic properties of large micron-sized H-ZSM-5 zeolite crystals. Two reaction temperatures are thereby investigated; i.e. 623 K and 773 K. The obtained results are shown in Figures 4.1 and 4.2.

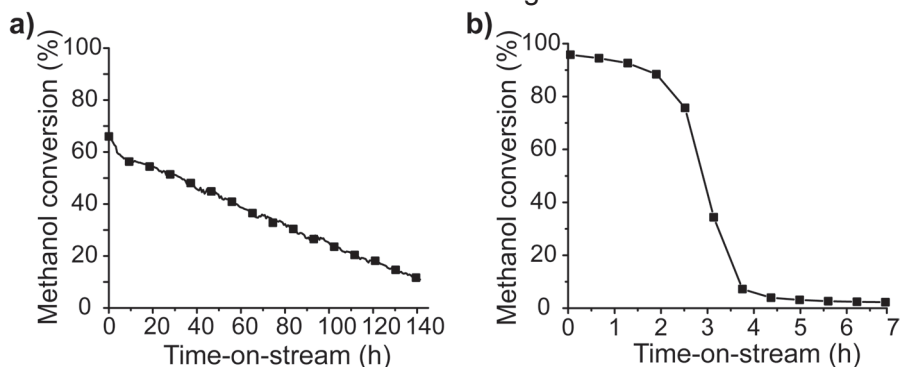


Figure 4.1: Methanol conversion activity of large coffin-shaped H-ZSM-5 zeolite crystals during the MTO reaction at (a) 623 K and (b) 773 K (WHSV = 5.56 gg⁻¹h⁻¹).

Figure 4.1 illustrates the methanol conversion activity of the large H-ZSM-5 zeolite crystals in a fixed-bed reactor. It is shown that despite their large crystal size, these coffin-shaped zeolites provide conversion profiles that are close to the conversion activities of H-ZSM-5 catalysts containing smaller crystal dimensions.^[6, 48, 59-62]

At a low reaction temperature of 623 K, the mild coke formation causes a slow deactivation that steadily progresses with reaction time. Here, the methanol conversion starts at ~ 65 % and ends-up to a final ~ 11 % after 142 h of reaction. Equivalent experiments, performed at 773 K, indicate a high initial conversion of ~ 96 % and the activity quickly drops after approximately 2.5 h ending up in ~ 3 % within 7 h of time-on-stream. The results are indicative for the temperature dependence of the coke formation and the

thereby related conversion activity. At mild reaction conditions, mostly alkylated mono-aromatic hydrocarbons form.^[17, 63, 64] These species play a double role. On one side they constitute the catalytic engine behind the MTO conversion thereby producing the desired olefins. On the other hand, further alkylations and subsequent growth of these hydrocarbons affect the methanol conversion, which explains the gradual deactivation. Increasing reaction temperature enhances the growth rate of these coke compounds that, in general, are considered to develop into larger species as well. This severe carbonaceous deposition strongly affects the catalyst activity as observed in Figure 4.1b. Parallel to the catalyst activity, the conversion selectivity was examined and the product yield is shown in Figure 4.2 as a function of methanol conversion.

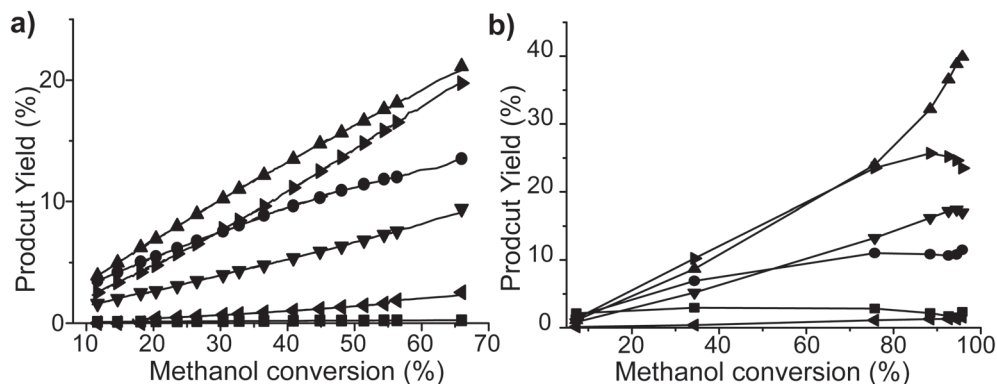


Figure 4.2: Effluent product yield of large coffin-shaped H-ZSM-5 zeolite crystals during the MTO conversion at (a) 623 K and (b) 773 K. The detected compounds are: C1 (■), C2 (●), C3 (▲), C4= (▼), C4 (◄) and C5+ (►).

At 623 K the gradual decrease in conversion activity results in a rather linear reduction of the corresponding conversion selectivity. The yield of desired C2 and C3 olefins, present in the reaction effluent, steadily decreases, while the fraction of larger C5+ compounds undergoes a more pronounced decline with progressing deactivation. The coke molecules retained within the zeolite porous network can still participate in the olefin conversion process, although they are less active reaction intermediates. In addition, their molecular size favors the effluent of light olefins compared to larger hydrocarbons.^[20, 64] The activity and selectivity results confirm that the large coffin-shaped zeolite is a proper catalyst that, at low reaction temperatures, produces light olefins despite the increasing carbonaceous deposition. When methanol is converted at elevated reaction temperatures, the severe coke formation strongly affects the amount of C3 species that diminishes with time-on-stream. At the same time, the fraction of large C4-C5+ compounds appears to increase, while the

amount of C1 and C2 products remain rather stable. This feature changes after 120 min of reaction. At this point, the coke growth generates more severe pore blockage. Here, the conversion activity strongly drops (Figure 4.1b) and the yield of bulky hydrocarbons decreases stronger compared to the C1 and C2 fractions.

4.3.2 Catalyst regeneration

The oxidative regeneration of coked zeolite catalysts can affect the crystal characteristics with possible consequences for the catalytic properties. Therefore, regeneration of the deactivated large coffin-shaped H-ZSM-5 zeolite crystals has been examined. The treatment was performed under oxidative atmosphere at 773 K for 11 h. After that, the zeolite material was re-subjected to an MTO cycle and this procedure was repeated 5 times, while monitoring the activity of the catalyst. The results are shown in Figure 4.3.

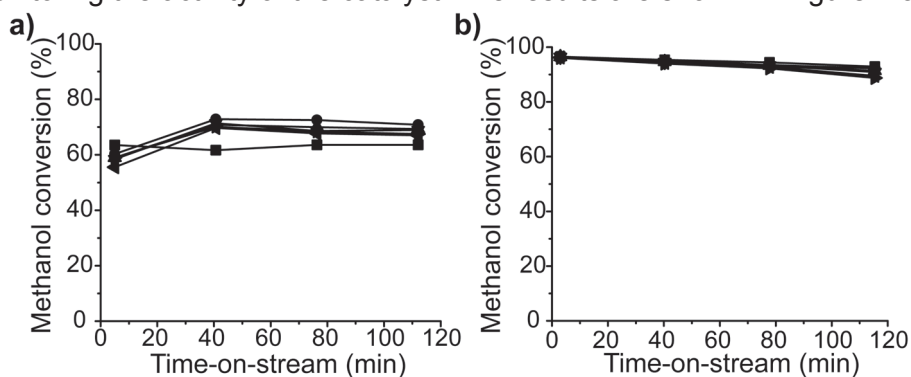


Figure 4.3: Conversion activity of large coffin-shaped H-ZSM-5 zeolite crystals during MTO conversion at (a) 623 K and (b) 773 K after different regeneration cycles: Fresh catalyst (■), 2nd cycle (●), 3rd cycle (▲), 4th cycle (▼), 5th cycle (◄) and 6th cycle (►).

At 623 K, the fresh H-ZSM-5 catalyst reaches rapidly a maximum methanol conversion activity that, over time, remains rather stable. After regeneration, however, the conversion requires a longer induction period of the HCP compounds and this initial increase of the methanol conversion is obtained for all subsequent cycles. It indicates that the first regeneration affects the H-ZSM-5 zeolite. However, this effect does not notably aggravate with consecutive regenerations. During the reaction at 773 K, such induction period is not observed and the methanol conversion profile is similar for all regenerations. The HCP build-up at these reaction temperatures is faster and probably within the experimental error.^[30, 33] These observations indicate a stable catalyst material that displays similar conversion activity despite the applied regeneration treatments.

4.3.3 Optical micro-spectroscopy

After reaction in the fixed-bed reactor, the coked zeolites have been analyzed with micro-spectroscopic techniques in order to examine the carbonaceous deposition at the individual catalyst particle level. Chapter 3 showed how the use of polarized light, in optical absorption measurements, enables to visualize species that are aligned within the straight channels of H-ZSM-5 zeolite.^[42, 51, 65] For this reason, the deactivated coffin-shaped H-ZSM-5 zeolites have been subjected to a polarization dependent UV-Vis absorption study at which a horizontal (along the straight channels) and a vertical (perpendicular to the straight channels) orientation of the polarizer with respect to the examined zeolite crystal was applied. A selection of the polarization dependent microphotographs with their corresponding absorption spectra and polarizer orientation are presented in Figure 4.4.

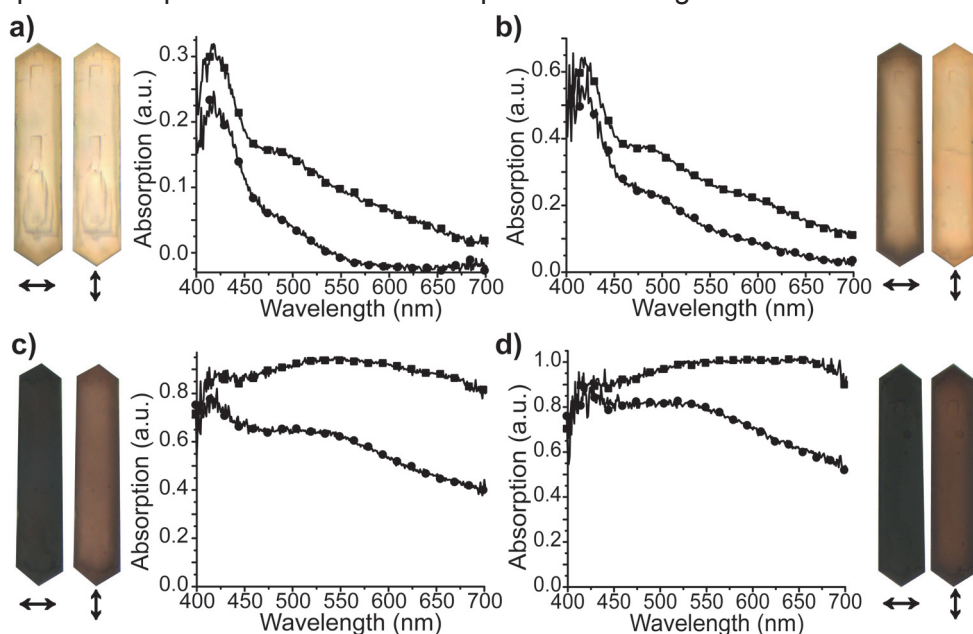


Figure 4.4: Polarization dependent optical microphotographs of the large coffin-shaped H-ZSM-5 zeolite crystals with their corresponding UV-Vis absorption spectrum. Images are taken after MTO conversion in the fixed-bed reactor at 623 K for (a) 1 MTO cycle and (b) 6 MTO cycles. Similar reaction performed at 773 K for (c) 1 MTO cycle and (d) 6 MTO cycles. The orientation of the polarizer is 0 and 90 degree as denoted with the arrows \leftrightarrow (■) and \updownarrow (●), respectively.

A stronger crystal darkening is observed when the light polarization coincides with the arrangement of the straight pores (0° , as denoted with the horizontal

arrow in Figure 4.4) and 90° rotation of the polarizer provides lighter crystal coloration.^[42, 55] These results are in line with a previous study.^[42] With the vertical polarization, the lack of alignment with the straight channels introduces a larger contribution of the zigzag pores. The findings therefore suggest a preferred macroscopic alignment of the carbocationic coke molecules along the straight channels of the H-ZSM-5 zeolite crystal. As it is plausible to assume that the coke compounds form throughout the entire zeolite, more conjugated compounds i.e. larger linear aromatic species, experience less constraints when they grow within the straight channels. The result is confirmed by the detection of intense absorption at higher wavelength.

At 623 K, the coke molecules cause mild crystal browning. This coloration intensifies with increasing number of regenerations and is most pronounced near the crystal edge. The absorption profile is characterized by an intense band located at 420 nm. In alignment with the straight zeolite pores, an additional band around 500 nm becomes most evident and with increasing regenerations this band becomes more distinct together with a minor absorption band around 600 nm. The 420 nm absorption band has been previously assigned to π - π^* transitions that originate from methyl-substituted benzenium cations.^[57, 66-69] These compounds constitute the catalytic scaffold of the HCP mechanism. The bands at higher excitation wavelengths originate from larger conjugated systems, mostly linear polyaromatic in nature.^[15, 17, 39] The vertical polarization introduces a larger contribution of the sinusoidal channels. Here, the large coke molecules no longer provide a prominent contribution to the overall absorption spectrum and the 420 nm band is dominant. At 773 K, crystal darkening is distinct and minor variations between the different regenerations are observed. When aligned with the straight zeolite channels, coke deposits are marked by a broad and intense absorption band around 550 nm that undergoes a red-shift. The results demonstrate the pronounced formation of large coke deposits with rising reaction temperature and this effect is further enhanced with increasing number of catalyst regeneration treatments.

When the same experiment is performed in the in-situ micro-spectroscopy cell, major similarities in both coloration and band location are observed as illustrated in Figure 4.5. Surprisingly, the shape of the absorption bands is less distinctive and in addition, at mild reaction conditions, more regeneration treatments translate in less coke formation. This last observation is in contrast to the results obtained with the fixed bed reactor. As the space-time between the in-situ cell and the fixed bed reactor has been kept at similar values, this variation must be explained by intrinsic reactor differences. Zeolites placed in the in-situ cell mainly come in contact with the reactant molecules only.

In the fixed-bed reactor however, the flow goes through the whole catalyst bed. As a result, (side) products that form during conversion additionally react with the zeolites in the catalyst bed. This has consequences for further coke formation and explains the differences observed. At elevated reaction temperatures, the enhanced coke formation and the occurrence of cracking and rearrangement reactions alleviate this effect as mirrored in the similarity of the experimental results.

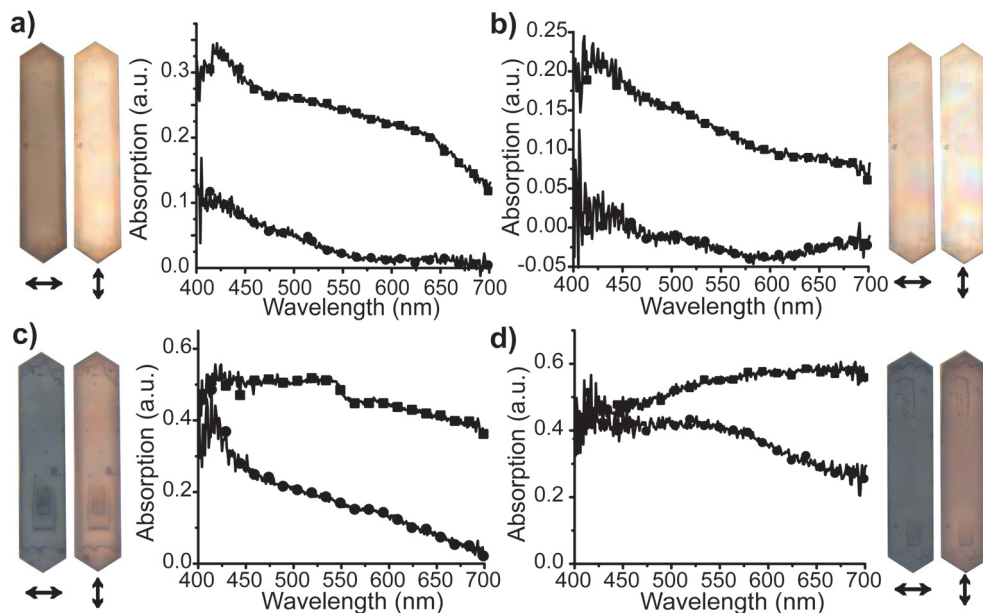


Figure 4.5: Polarization dependent optical microphotographs of the large coffin-shaped H-ZSM-5 zeolite crystals with their corresponding UV-Vis absorption spectrum. Images are taken after MTO conversion in the in-situ cell at 623 K for (a) 1 MTO cycle and (b) 6 MTO cycles. Similar reaction performed at 773 K for (c) 1 MTO cycle and (d) 6 MTO cycles. The orientation of the polarizer is 0 and 90 degree as denoted with the arrows \leftrightarrow (\blacksquare) and \updownarrow (\bullet), respectively.

4.3.4 Analysis of the retained species

After reaction, the zeolites have been dissolved in HF and extraction with dichloromethane (DCM) allowed the analysis of the hydrocarbons retained within the zeolite H-ZSM-5 crystals. Figure 4.6 shows the GC-MS total ion chromatogram of the hydrocarbon extracts obtained after reaction at 623 K for 2.5 days, 6 days and after 1 regeneration cycle. A small number of compounds were detected as dominant species. These are: Tetramethylbenzene (TMB), pentamethylbenzene (PMB) and hexamethylbenzene (HMB) and their peak intensities are directly comparable. The highest amount of retained

hydrocarbons was obtained after 2.5 days on stream and the amount of species, that are soluble in DCM, decreased with increasing reaction time (Figure 4.6b). The regenerated catalyst (Figure 4.6c) contained, after 2 h on methanol stream, a larger amount of retained hydrocarbons compared to the most deactivated catalyst (after 6 days of reaction, Figure 4.6b). This higher HCP species concentration is explained by the solubility in DCM of small aromatics compared to more heavy hydrocarbons. The larger compounds are less soluble in DCM. The coke determined by GC-MS is therefore not the total coke. Previous studies reported a discrepancy between the total coke content determined by temperature programmed oxidation and the organics determined by HF dissolution. This difference is fully ascribed to the amount of coke retained within the deactivated ZSM-5 zeolites that is insoluble in DCM.^[17, 47, 70, 71]

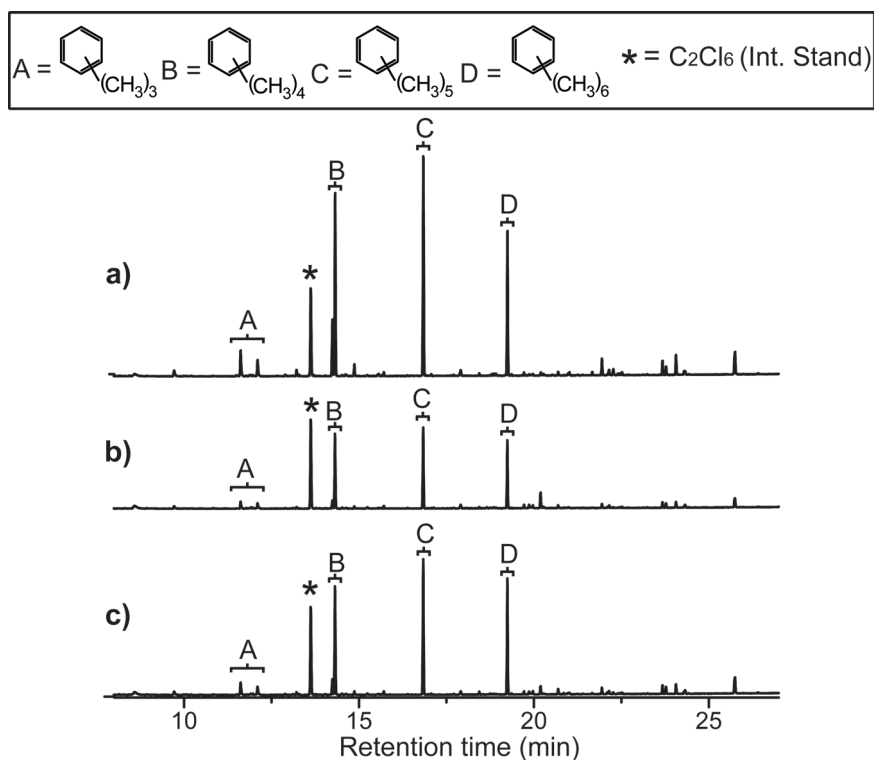


Figure 4.6: GC-MS total ion chromatogram of the hydrocarbon extracts after methanol conversion at 623 K for (a) 2.5 days on stream, (b) 6 days on stream and (c) regenerated large coffin-shaped H-ZSM-5 zeolite crystals after 2 h on stream. All peaks are normalized relative to the standard C₂Cl₆ peak indicated by * in the chromatogram.

Figure 4.7 displays the GC-MS total ion chromatogram of the hydrocarbon extracts obtained after methanol conversion at 773 K. Compared to the extract at 623 K, the amount of the retained species detected using GC-MS at 773 K was low despite the very dark color of the catalyst material. This is largely ascribed to the formation of insoluble coke compounds at this reaction temperature and in agreement with the intense UV-Vis absorption at higher wavelengths described before. After increasing the sensitivity by a factor of 10, TMB and PMB were seen as the most abundant species, whereas the concentration of HMB resulted to be lower. In addition, a relatively higher presence of larger hydrocarbons was detected.

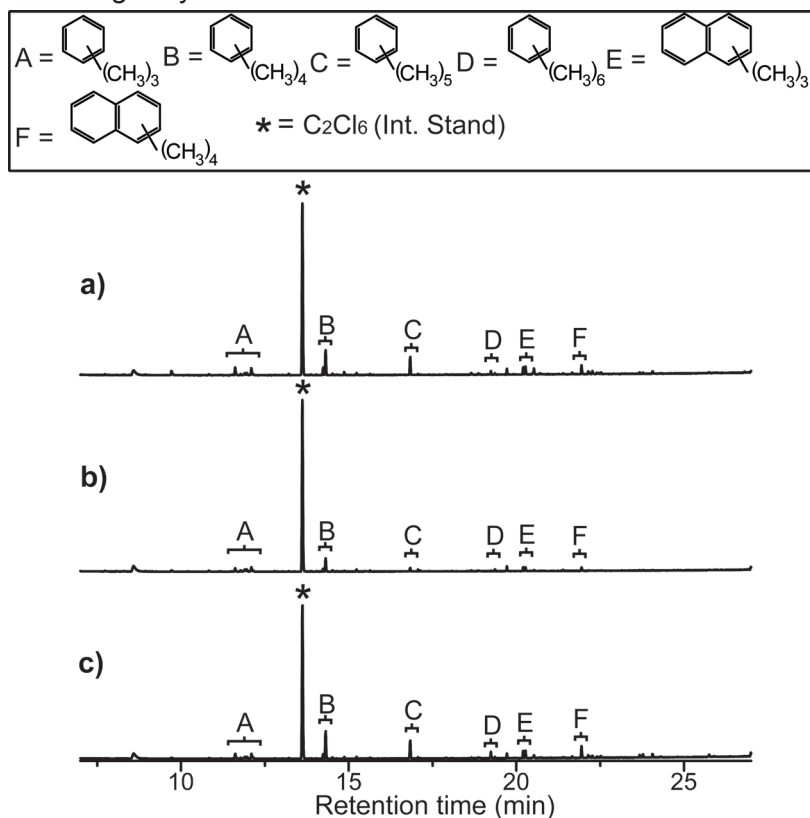


Figure 4.7: GC-MS total ion chromatogram of the hydrocarbon extracts after methanol conversion at 773 K for (a) 2.5 h on stream, (b) 7 h on stream and (c) regenerated large coffin-shaped H-ZSM-5 zeolite crystals after 2 h on stream. The peaks are normalized relative to the standard C_2Cl_6 peak indicated by * in the chromatogram. The sensitivity is increased by a factor of 10 compared to Figure 4.6.

4.4 Conclusions

Large coffin-shaped H-ZSM-5 zeolite crystals are investigated during the Methanol-to-Olefin (MTO) conversion. UV-Vis micro-spectroscopy is used to investigate the zeolite crystals in a spatiotemporal manner at the individual particle level. Fixed-bed effluent analysis is applied to provide insights on the catalyst activity and selectivity bulk properties. The combination of these approaches allows relating the catalyst bulk characteristics to the coke formation observed during single particle examinations.

The large zeolite crystals proved to have conventional conversion characteristics and moderate variations are obtained between the two different reaction cells applied. At mild reaction temperatures, a moderate coke formation translates in a slow progressing loss of activity. The catalyst remains active for a long period and the coke deposits formed contain highly methyl-substituted mono-aromatics. This methanol transformation produces mainly C₃, C₅₊ and C₂ hydrocarbons. With increasing reaction temperature, the enhanced coke formation rate induces a strong decline in conversion activity. During this, the catalyst selectivity changes allowing C₁ and C₂ products to form at the expense of C₃ and C₅ hydrocarbons. The coffin-shaped zeolite crystals showed stable MTO activity after 5 regeneration cycles. With the fixed bed reactor, increasing regeneration cycles generates more pronounced coke deposition that in addition contains larger coke species. This enhanced coke formation is however not observed when using the in-situ micro-spectroscopy cell. Regardless the reactor type, the coke deposits showed a preferred alignment with the H-ZSM-5 straight channels.

Acknowledgements

Shewangizaw Teketel and Prof. Unni Olsbye (Oslo University, Norway) are thanked for the measurements of the zeolite bulk catalytic properties as well as many fruitful discussions. Dr. Machteld Mertens (ExxonMobil, Belgium) is acknowledged for providing the H-ZSM-5 crystals.

References

- [1] A. Corma, *Chem. Rev.* **1995**, 95, 559-614.
- [2] G. Busca, *Chem. Rev.* **2007**, 107, 5366-5410.
- [3] H. van Bekkum, E.M. Flanigen, P.A. Jacobs, J.C. Jansen (Eds.), *Introduction to Zeolite Science and Practice*, Elsevier, Amsterdam, **2001**.
- [4] R.K. Graselli, A.W. Sleight (Eds.), *Structure-Activity and Selectivity Relationships in Heterogeneous Catalysis*, Elsevier, Amsterdam, **1990**.

- [5] T. Mokrani, M. Scurrrell, *Catal. Rev. Sci. Eng.* **2009**, *51*, 1-145.
- [6] M. Stöcker, *Microporous Mesoporous Mater.* **1999**, *29*, 3-48.
- [7] M. Bjorgen, U. Olsbye, D. Petersen, S. Kolboe, *J. Catal.* **2004**, *221*, 1-10.
- [8] M. Bjorgen, F. Joensen, K. P. Lillerud, U. Olsbye, S. Svelle, *Catal. Today* **2009**, *142*, 90-97.
- [9] I. M. Dahl, S. Kolboe, *Catal. Lett.* **1993**, *20*, 329-336.
- [10] I. M. Dahl, S. Kolboe, *J. Catal.* **1994**, *149*, 458-464.
- [11] I. M. Dahl, S. Kolboe, *J. Catal.* **1996**, *161*, 304-309.
- [12] S. Svelle, M. Bjorgen, S. Kolboe, D. Kuck, M. Letzel, U. Olsbye, O. Sekiguchi, E. Uggerud, *Catal. Lett.* **2006**, *109*, 25-35.
- [13] S. Svelle, F. Joensen, J. Nerlov, U. Olsbye, K. P. Lillerud, S. Kolboe, M. Bjorgen, *J. Am. Chem. Soc.* **2006**, *128*, 14770-14771.
- [14] U. Olsbye, M. Bjorgen, S. Svelle, K. P. Lillerud, S. Kolboe, *Catal. Today* **2005**, *106*, 108-111.
- [15] H. Schulz, *Catal. Today* **2010**, *154*, 183-194.
- [16] P. L. Benito, A. G. Gayubo, A. T. Aguayo, M. Olazar, J. Bilbao, *Ind. Eng. Chem. Res.* **1996**, *35*, 3991-3998.
- [17] M. Bjorgen, S. Akyalcin, U. Olsbye, S. Benard, S. Kolboe, S. Svelle, *J. Catal.* **2010**, *275*, 170-180.
- [18] D. Chen, H. P. Rebo, K. Moljord, A. Holmen *Ind. Eng. Chem. Res.* **1997**, *36*, 3473-3479.
- [19] G. F. Froment, J. Demeyer, E. G. Derouane, *J. Catal.* **1990**, *124*, 391-400.
- [20] K. Hemelsoet, A. Nollet, M. Vandichel, D. Lesthaeghe, V. Van Speybroeck, M. Waroquier, *ChemCatChem.* **2009**, *1*, 373-378.
- [21] J. F. Haw, D. M. Marcus, *Top. Catal.* **2005**, *34*, 41-48.
- [22] D. Lesthaeghe, A. Horre, M. Waroquier, G. B. Marin, V. Van Speybroeck, *Chem. Eur. J.* **2009**, *15*, 10803-10808.
- [23] M. Guisnet, L. Costa, F. R. Ribeiro, *J. Mol. Catal. A* **2009**, *305*, 69-83.
- [24] L. Sommer, D. Mores, S. Svelle, M. Stöcker, B. M. Weckhuysen, U. Olsbye, *Microporous Mesoporous Mater.* **2010**, *132*, 384-394.
- [25] L. Sommer, A. Krivokapic, S. Svelle, K. P. Lillerud, M. Stocker, U. Olsbye, *J. Phys. Chem. C* **2011**, *115*, 6521-6530.
- [26] A. O. E. Beyne, G. F. Froment, *Chem. Eng. J.* **2001**, *82*, 281-290.
- [27] Y. Bouzidi, I. Diaz, L. Rouleau, V. P. Valtchev, *Adv. Funct. Mater.* **2005**, *15*, 1955-1960.
- [28] A. T. Aguayo, A. G. Gayubo, A. Atutxa, B. Valle, J. Bilbao, *Catal. Today* **2005**, *107*, 410-416.
- [29] J. Datka, B. Gil, *Microporous Mesoporous Mater.* **2007**, *103*, 225-229.
- [30] H. Schulz, Z. Siwei, H. Kusterer (Eds.), *Autocatalysis, Retardation, Reanimation and Deactivation during Methanol Conversion on Zeolite HZSM5*, Elsevier, **1991**, 281-290.
- [31] F. Bauer, W. H. Chen, E. Biiz, A. Freyer, V. Sauerland, S. B. Liu, *J. Catal.* **2007**, *251*, 258-270.
- [32] M. Guisnet, P. Magnoux, *Appl. Catal.* **1989**, *54*, 1-27.

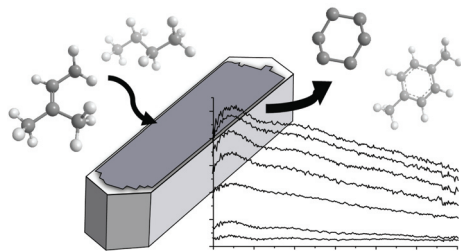
- [33] H. Schulz, K. Lau, M. Claeys, *Appl. Catal. A* **1995**, *132*, 29-40.
- [34] M. W. Anderson, B. Sulikowski, P. J. Barrie, J. Klinowski, *J. Phys. Chem.* **1990**, *94*, 2730-2734.
- [35] J. A. Bergwerff, A. A. Lysova, L. Espinosa-Alonso, I. V. Koptuyg, B. M. Weckhuysen, *Chem. Eur. J.* **2008**, *14*, 2363-2374.
- [36] D. Chen, A. Gronvold, H. P. Rebo, K. Moljord, A. Holmen, *Appl. Catal. A* **1996**, *137*, 1-8.
- [37] S. Gomm, R. Glaser, J. Weitkamp, *Chem. Eng. Technol.* **2002**, *25*, 962-966.
- [38] Y. J. Jiang, J. Huang, V. R. Marthala, Y. S. Ooi, J. Weitkamp, M. Hunger, *Microporous Mesoporous Mater.* **2007**, *105*, 132-139.
- [39] G. Spoto, F. Geobaldo, S. Bordiga, C. Lamberti, D. Scarano, A. Zecchina, *Top. Catal.* **1999**, *8*, 279-292.
- [40] B. M. Weckhuysen, *Angew. Chem. Int. Ed.* **2009**, *48*, 4910-4943.
- [41] D. Mores, E. Stavitski, M. H. F. Kox, J. Kornatowski, U. Olsbye, B. M. Weckhuysen, *Chem. Eur. J.* **2008**, *14*, 11320-11327.
- [42] D. Mores, J. Kornatowski, U. Olsbye, B.M. Weckhuysen, *Chem. Eur. J.* **2011**, *17*, 2874-2884.
- [43] A. N. Parvulescu, D. Mores, E. Stavitski, C. M. Teodorescu, P. C. A. Bruijninx, R. J. M. Klein-Gebbink, B. M. Weckhuysen, *J. Am. Chem. Soc.* **2010**, *132*, 10429-10439.
- [44] Y-M Chung, D. Mores, B.M. Weckhuysen, *Appl. Catal. A* **2011**, doi: 10.1016/j.apcata.2011.06.030.
- [45] D. Mores, E. Stavitski, S.P. Verkleij, A. Lombard, A. Cabiacc, L. Rouleau, J. Patarin, A. Simon-Masseron, B.M. Weckhuysen, *Phys. Chem. Chem. Phys.* **2011**, doi: 10.1039/c1cp21324e.
- [46] Q. Qian, D. Mores, J. Kornatovski, B.M. Weckhuysen, *Microporous Mesoporous Mater.* **2011**, doi: 10.1016/j.micromeso.1011.05.024.
- [47] M. Bjorgen, S. Svelle, F. Joensen, J. Nerlov, S. Kolboe, F. Bonino, L. Palumbo, S. Bordiga, U. Olsbye, *J. Catal.* **2007**, *249*, 195-207.
- [48] F. Bleken, W. Skistad, K. Barbera, M. Kustova, S. Bordiga, P. Beato, K. P. Lillerud, S. Svelle, U. Olsbye, *Phys. Chem. Chem. Phys.* **2011**, *13*, 2539-2549.
- [49] S. Teketel, S. Svelle, K. P. Lillerud, U. Olsbye *ChemCatChem* **2009**, *1*, 78-81.
- [50] S. Teketel, U. Olsbye, K. P. Lillerud, P. Beato, S. Svelle, *Microporous Mesoporous Mater.* **2010**, *136*, 33-41.
- [51] E. Stavitski, M. H. F. Kox, B. M. Weckhuysen, *Chem. Eur. J.* **2007**, *13*, 7057-7065.
- [52] M. H. F. Kox, E. Stavitski, J. C. Groen, J. Perez-Ramirez, F. Kapteijn, B. M. Weckhuysen, *Chem. Eur. J.* **2008**, *14*, 1718-1725.
- [53] L. Karwacki, B. M. Weckhuysen, *Phys. Chem. Chem. Phys.* **2011**, *13*, 3681-3685.
- [54] L. Karwacki, M. H. F. Kox, D. A. M. de Winter, M. R. Drury, J. D. Meeldijk, E. Stavitski, W. Schmidt, M. Mertens, P. Cubillas, N. John, A. Chan, N. Kahn, S. R. Bare, M. Anderson, J. Kornatowski, B. M. Weckhuysen, *Nature Mater.* **2009**, *8*, 959-965.
- [55] L. Karwacki, E. Stavitski, M. H. F. Kox, J. Kornatowski, B. M. Weckhuysen, *Angew. Chem. Int. Ed.* **2007**, *46*, 7228-7231.
- [56] P. Magnoux, H. S. Cerqueira, M. Guisnet, *Appl. Catal. A* **2002**, *235*, 93-99.

- [57] L. Palumbo, F. Bonino, P. Beato, M. Bjorgen, A. Zecchina, S. Bordiga, *J. Phys. Chem. C* **2008**, *112*, 9710-9716.
- [58] J. Li, G. Xiong, Z. Feng, Z. Liu, Q. Xin, C. Li, *Microporous Mesoporous Mater.* **2000**, *39*, 275-280.
- [59] F. Bleken, S. Svelle, K. P. Lillerud, U. Olsbye, B. Arstad, O. Swang, *J. Phys. Chem. A* **2010**, *114*, 7391-7397.
- [60] F. Bleken, F.T.V.W. Janssen, U. Olsbye, **2011**, *in preparation*.
- [61] Y. Q. Song, X. X. Zhu, L. Y. Xu, *Catal. Comm.* **2006**, *7*, 218-223.
- [62] W. J. H. Dehertog, G. F. Froment, *Appl. Catal.* **1991**, *71*, 153-165.
- [63] D. Lesthaeghe, J. Van der Mynsbrugge, M. Vandichel, M. Waroquier, V. Van Speybroeck, *ChemCatChem.* **2011**, *3*, 208-212.
- [64] M. Vandichel, D. Lesthaeghe, J. Van der Mynsbrugge, M. Waroquier, V. Van Speybroeck, *J. Catal.* **2010**, *271*, 67-78.
- [65] F. Marlow, K. Hoffmann, G. G. Lindner, I. Girnus, G. van de Goor, J. Kornatowski, J. Caro, *Micropor. Mater.* **1996**, *6*, 43-49.
- [66] C. Paze, B. Sazak, A. Zecchina, J. Dwyer, *J. Phys. Chem. B* **1999**, *103*, 9978-9986.
- [67] J. W. Park, G. Seo, *Appl. Catal. A* **2009**, *356*, 180-188.
- [68] I. Kiricsi, G. Tasi, H. Forster, P. Fejes, *J. Mol. Struct.* **1990**, *218*, 369-374.
- [69] I. Kiricsi, H. Forster, G. Tasi, J. B. Nagy, *Chem. Rev.* **1999**, *99*, 2085-2114.
- [70] M. Bjorgen, U. Olsbye, S. Kolboe, *J. Catal.* **2003**, *215*, 30-44.
- [71] F. Bleken, M. Bjorgen, L. Palumbo, S. Bordiga, S. Svelle, K. P. Lillerud, U. Olsbye, *Top. Catal.* **2009**, *52*, 218-228.

Chapter 5

Coke Formation during Paraffin and Olefin Aromatization over H-ZSM-5 Molecular Sieves

Spatial and Temporal Mapping of Coke within Individual Zeolite Crystals



The conversion of paraffin and olefin hydrocarbons causes the growth of carbonaceous deposits. This coke formation depends on the reactant type, size and branching. These differences are visualized, at the individual particle level, in a space- and time-resolved manner by using UV-Vis microspectroscopy and confocal fluorescence microscopy.

5.1 Introduction

The aromatization of paraffins and olefins, originating from light cracked naphtha, is considered a promising method that allows the conversion of excess low-value hydrocarbons into aromatics. These compounds, mostly light arenes like benzene, toluene and xylenes, are valuable and can be used either as chemical feedstock or high-octane gasoline blending components.^[1, 2] Unfortunately, this aromatization process suffers from severe catalyst deactivation and therefore fails to meet industrial requirements. Here, catalyst deactivation is mainly caused by the formation of undesired carbonaceous materials, a process that is usually inevitable during hydrocarbon processing.^[3] These coke deposits generally provoke the loss of activity and changes in selectivity. For this reason, major efforts are focusing on the development of catalysts with a good selectivity towards aromatization and high coke-resistance properties.^[4-18] Research studies elucidated, for example, how the modification of zeolites with group VIII, IB, IIB and IIIA metals can improve the selectivity towards aromatics. However, despite these modifications severe catalyst deactivation remains problematic, especially at high reaction temperatures.^[10-13, 19-21] Various characterization techniques have been applied with the aim of elucidating the nature of the coke and finding efficient methods that prevent or alleviate the unfavorable catalyst deactivation. The complex conversion, however, involves a variety of reactions to take place simultaneously, which make an in-depth characterization a challenging practice.^[22-24] The investigation of the coke formation under reaction conditions is furthermore limited. For this, in-situ characterization techniques have drawn the attention with the expectation to obtain new insights into the processes that occur in a working catalyst.^[25-31] This Chapter describes the use of in-situ UV-Vis and confocal fluorescence micro-spectroscopic techniques for the investigation of coke formation processes that occur during the aromatization reaction of linear and branched C4-C7 paraffin and olefin hydrocarbons. In this comparative study the light cracked naphtha components (butane, 1-butene, 2-methylbutane, 2-methyl-2-butene, pentane, 1-pentene, 2-methylpentane, 2-methyl-2-pentene, hexane, 1-hexene, 2-methylhexane and 2-methyl-2-hexene), are studied in a space- and time-resolved manner within an individual H-ZSM-5 zeolite crystal. It will be shown that the coke deposition varies depending on the applied reactants and the crystal location.

5.2 Experimental

5.2.1 Methods

UV-Vis micro-spectroscopy

An Olympus BX41 upright microscope, along with a 50 x 0.5 NA-high working distance objective was used for measuring UV-Vis absorption spectra.^[32] The setup was equipped with a 50/50 double-viewpoint tube, that accommodates a CCD video camera (ColorView IIIu, Soft Imaging System GmbH) and an optical fiber mount. A 200 μm -core fiber connected the microscope to a CCD UV/Vis spectrometer (AvaSpec-2048TEC, Avantes). A 75 W tungsten lamp provided the illumination, while a rotatable polarizer between the objective lens and the detector allows separating a desirable light polarization.

Confocal fluorescence microscopy

In-situ fluorescence microscopy studies were carried out on a Nikon Eclipse LV150 upright microscope equipped with a Nikon D-Eclipse C1 head connected to the laser light source (561 nm). The emission was detected with a photomultiplier tube in the 575-635 nm range. The in-situ confocal fluorescence microscopy measurements were carried out at the middle horizontal plane parallel to the upper plane in the crystal center. The ex-situ confocal fluorescence microscopy studies were performed using a Nikon Eclipse 90i upright microscope with a 50x 0.55 NA dry objective lens. Confocal fluorescence microscopy images were collected by a Nikon A1-SHR A1 R scan head connected to laser light sources with emission wavelengths of 405, 488, 561 and 637 nm. The emission was detected by an A1-DU4 4 detector unit. The used detection ranges were 425-475 nm, 510-550 nm, 570-620 nm and 662-737 nm, respectively.

In-situ cell

The experiments were performed at ambient pressure in a Linkam TS1500 in-situ cell equipped with a Linkam TMS 94 temperature controller. The calcined crystals were heated up to 773 K at the rate of 10 K $\cdot\text{min}^{-1}$ and kept at this temperature for 1 h under inert atmosphere with N_2 . After the in-situ cell temperature was stabilized, the N_2 flow was diverted through a bubbler containing the selected reactant thereby acting as carrier gas. The gas flow was kept constant at 60 ml $\cdot\text{min}^{-1}$ (WHSV 5.5 gg $^{-1}\text{h}^{-1}$) for all experiments. During the experiment, the bubbler was cooled with ice to control the evaporation rate of the volatile feedstock.

5.2.2 Materials

The H-ZSM-5 crystals (Si/Al ratio of 17) contain typical dimensions of 100 x 20 x 20 μm and detailed characteristics of the micron-sized H-ZSM-5 crystallites used are reported in Chapters 2-4.^[32-37] Butane (99%, ABCR), 1-butene (99%, Hoek Loos), pentane (99%, Acros Organics), 1-pentene (98%, Acros Organics), hexane (99%, Acros Organics), 1-hexene (98%, Acros Organics), 2-methylbutane (99%, Sigma-Aldrich), 2-methyl-2-butene (99%, Sigma-Aldrich), 2-methylpentane (99%, Sigma-Aldrich), 2-methyl-2-Pentene (99%, Fluka) 2-methylhexane (99%, Acros Organics) and 2-methyl-2-hexene (96%, Sigma-Aldrich) were used as received without further purification.

5.3 Results and discussion

The micron-sized H-ZSM-5 zeolite crystals are placed on the heating stage of the in-situ cell where they are exposed to each individual reactant flow at 773 K. The zeolites under study are not single crystals, but rather consist of six distinct subunits with a 90° rotation, as reported in previous chapters.^[34, 35, 38] In what follows, we discuss the in-situ micro-spectroscopy results separately for linear C4-C6 and branched C5-C7 hydrocarbons.

5.3.1 Conversion of linear paraffins and olefins

Upon exposure of linear C4-C6 paraffin and olefin vapor, darkening of the initially translucent H-ZSM-5 crystals indicates the formation of carbonaceous deposits during the aromatization process. These color changes are observed in the optical microphotographs taken as a function of reaction time and a selection of these images are displayed in Figure 5.1.

These images evidence the influence of the reactant molecule on the coke that forms during hydrocarbon conversion. The linear paraffinic hydrocarbons give minor zeolite darkening throughout the entire period of reaction, while the strong coloration, induced by the olefinic derivatives, suggests their pronounced role in the formation of undesired carbonaceous deposits. The darkening varies depending on the applied reactant chain length. Butene for instance causes a light crystal browning within 2 min of reaction, whereas hexene produces a darker crystal, although this coloration is detected after a longer time-on-stream. The higher partial pressure with increasing reactant size can be the cause behind the reduced coke growth rate and is inherent to the experimental set-up. The pronounced darkening with increasing reactant carbon number nevertheless indicates the formation of more or larger coke compounds when converting more extended hydrocarbons.

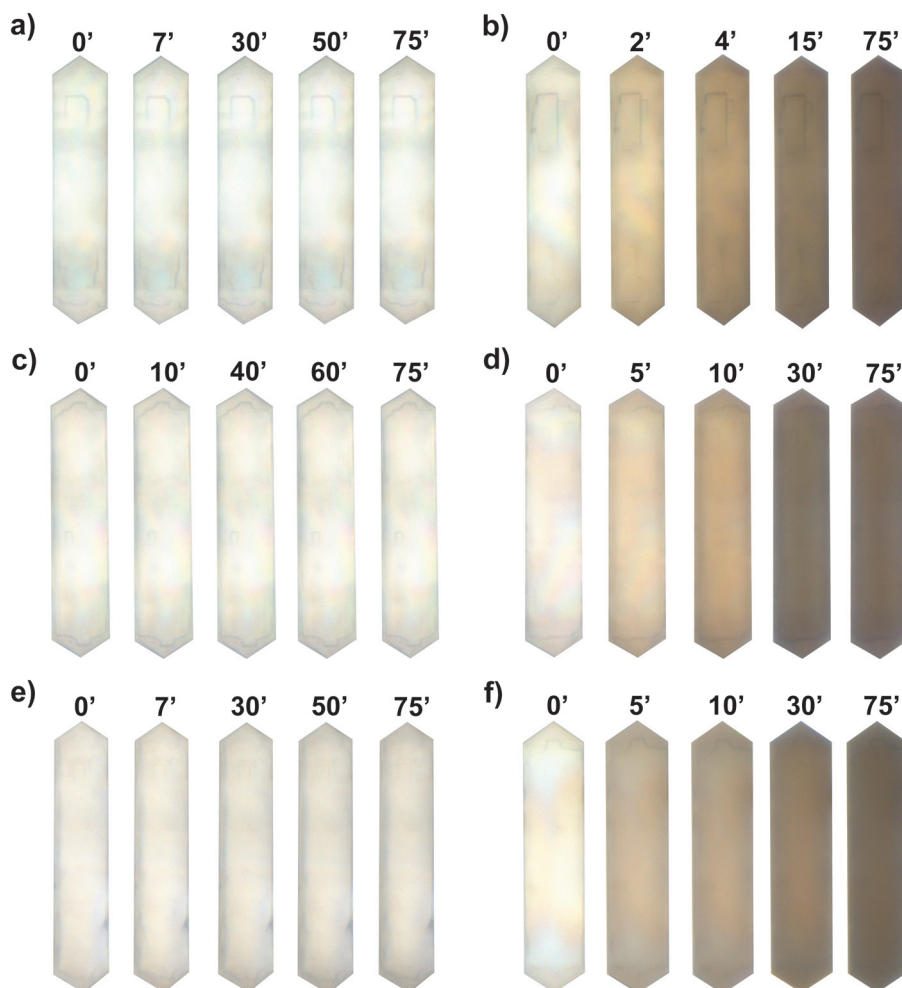


Figure 5.1: Selection of optical microphotographs of the H-ZSM-5 zeolite crystals taken during the aromatization process with (a) butane, (b) 1-butene, (c) pentane, (d) 1-pentene, (e) hexane and (f) 1-hexene at 773 K. The corresponding time is indicated in min.

These optically observed variations are reflected in the corresponding UV-Vis absorption spectra recorded from a 2 μm spot in the central region of the individual H-ZSM-5 zeolite crystal. A selection of the UV-Vis absorption spectra is given as a function of reaction time in Figure 5.2.

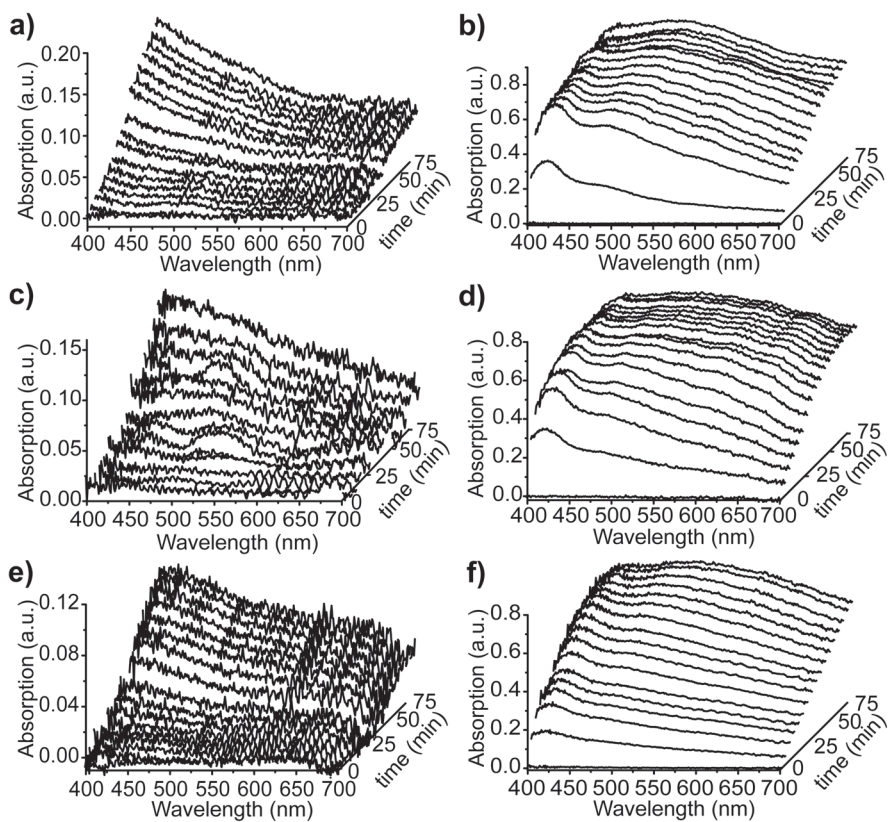


Figure 5.2: Selection of time-resolved in-situ UV-Vis absorption spectra taken from a spot in the middle of the H-ZSM-5 zeolite crystals during the aromatization process at 773 K of (a) butane, (b) 1-butene, (c) pentane, (d) 1-pentene, (e) hexane and (f) 1-hexene.

The conversion of linear paraffinic hydrocarbons causes the growth of an absorption band around 400 nm (Figures 5.2a, c and e). The absorption intensity of this band is low and further decreases in intensity with increasing reactant chain length. The absorption intensity in the olefinic counterparts, on the contrary, does not notably vary with different carbon number (Figures 5.2b, d and f). When the reactants reach the zeolite catalyst, the optically observed carbonaceous deposition results in the growth of an absorption band located at 420 nm. While this band formation is still progressing, a second band around 500 nm starts to form as well. During the conversion, this absorption band undergoes a red shift and with increasing reactant chain length it becomes less distinctive as broadening occurs. The assignment of

these absorption bands is not trivial as a variety of similar compounds are being formed during the process. However, based on previous studies these bands can be assigned to the π - π^* transitions of conjugated species.^[39-43] The first absorption band located at 420 nm originates from mainly oligomers and alkylated mono-aromatics. The band formed around 500 nm is due to larger conjugated compounds, such as linear polyaromatic carbocations. The growth of this second band lags behind the 420 nm band formation and ends at about equal intensity. The additional red shift combined with broadening furthermore advocate for the growth of small conjugated hydrocarbons towards more extended carbonaceous deposits.

5.3.2 Conversion of branched paraffins and olefins

Similar experiments as explained above are performed with analogous paraffin and olefin reactants containing an additional methyl branched group. An overview of the optical microphotographs taken upon exposure of these branched hydrocarbons at 773 K is given in Figure 5.3.

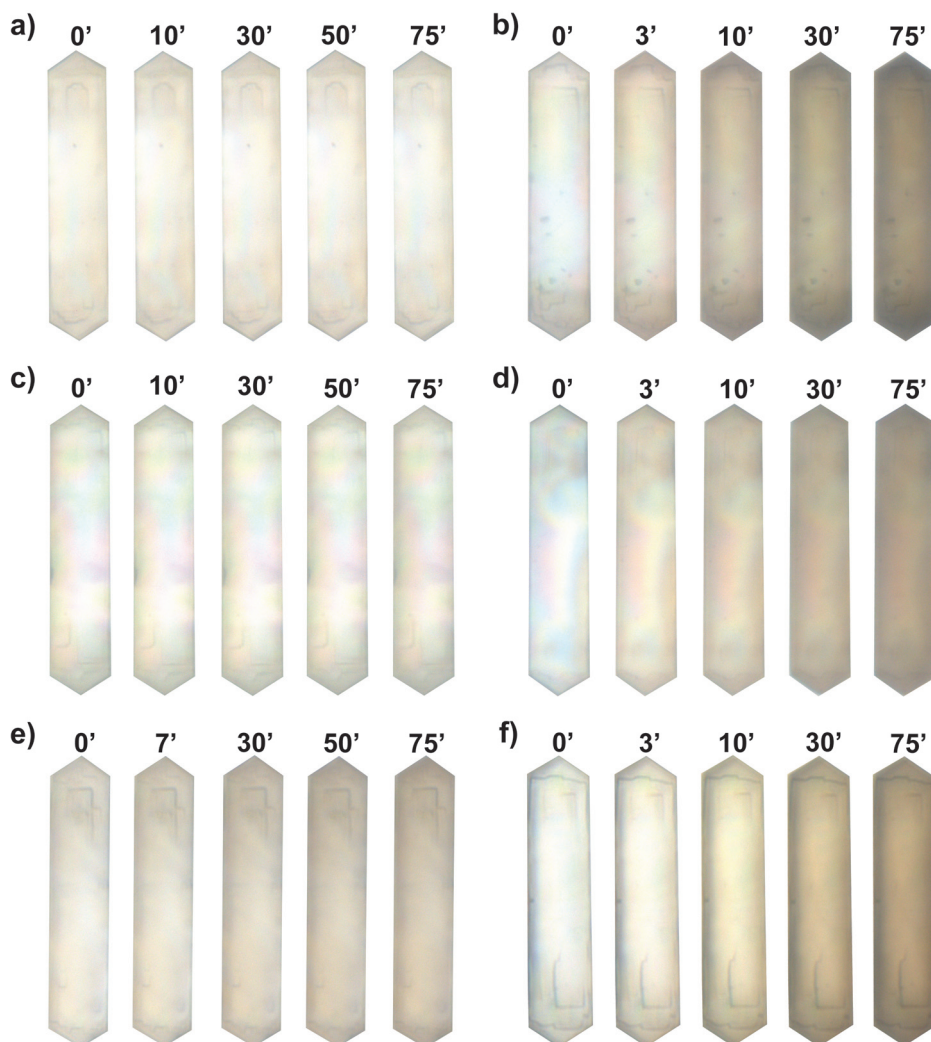


Figure 5.3: Selection of optical microphotographs of the H-ZSM-5 zeolite crystals taken during the aromatization process at 773 K with (a) 2-methylbutane, (b) 2-methyl-2-butene, (c) 2-methylpentane, (d) 2-methyl-2-pentene, (e) 2-methylhexane and (f) 2-methyl-2-hexene. The corresponding time is indicated in min.

Analysis of Figure 5.3 illustrates that branched hydrocarbons cause coke formation patterns that are similar to the case of linear reactants. The branched paraffinic species induce mild catalyst coloration, whereas pronounced darkening of the zeolite crystals occurs during the conversion of the complementary olefins. However, in contrast to the linear alkenes,

branched olefins generate an overall less distinct darkening of the H-ZSM-5 zeolite and an increasing reactant chain length results in alleviated crystal coloration. A selection of the time-resolved UV-Vis absorption spectra, taken during the aromatization process with the branched C5-C7 reactants, is shown in Figure 5.4.

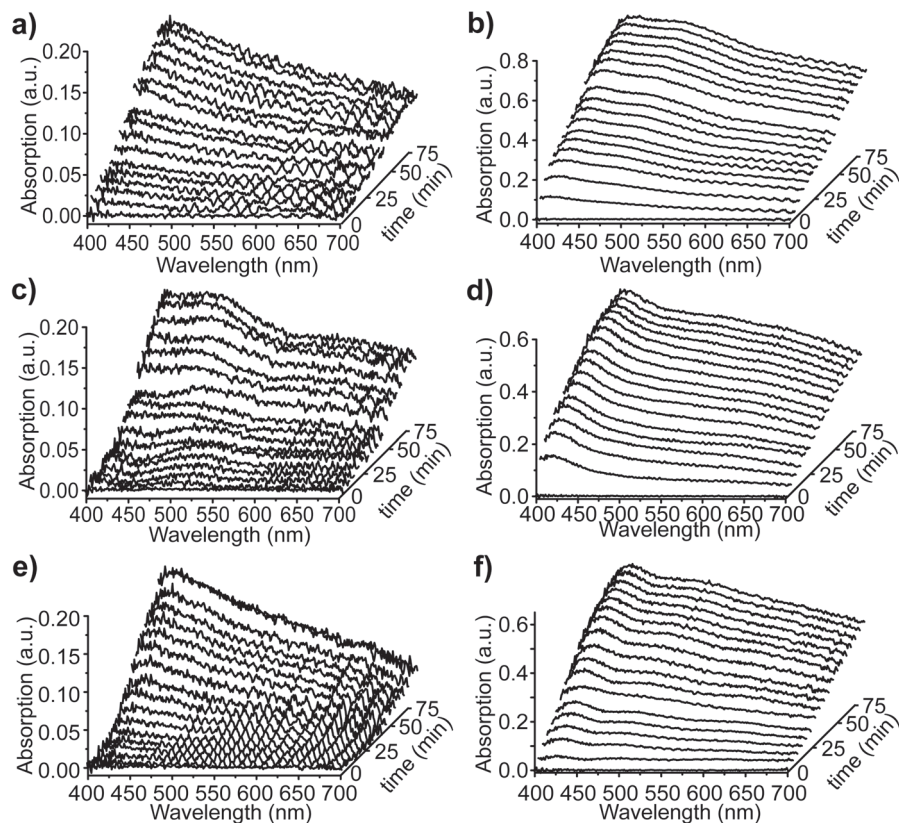


Figure 5.4: Selection of time-resolved in-situ UV-Vis absorption spectra taken from a spot in the middle of the H-ZSM-5 zeolite crystals during the aromatization process at 773 K with (a) 2-methylbutane, (b) 2-methyl-2-butene, (c) 2-methylpentane, (d) 2-methyl-2-pentene, (e) 2-methylhexane and (f) 2-methyl-2-hexene.

Likewise the linear hydrocarbons, branched paraffins cause weak absorption intensity with a maximum around 400 nm, while branched olefinic reactants give rise to more intense absorption with bands located at 420 nm and 500 nm. In comparison with linear hydrocarbons, this second absorption band undergoes a less pronounced red shift and broadening, and throughout the entire period of the reaction the 420 nm absorption band remains most

indicative for the formation of coke. The limited red shift with minor broadening indicates that the coke deposits generated by the branched olefins undergo a limited growth and throughout the reaction remain rather confined in size. Their prominent absorption at lower wavelengths furthermore advocates that the majority of the retained products is of oligomeric or mono-aromatic character. These findings are in line with the alleviated crystal darkening observed.

Many reactions simultaneously take place during the aromatization of light naphtha derivatives. In general, the aromatics are considered to form either directly via alkane dehydrocyclization or indirectly through alkane dehydrogenation into alkene with subsequent rearrangements. For both routes, successive reactions, such as cracking, oligomerization, cyclization and hydrogen transfer, can result in the undesired coke compounds.^[5, 6, 10-15, 44-50] The minute zeolite darkening, along with weak UV-Vis absorption, suggests a limited reactivity and consequently limited coke growth of the paraffin reactants. This process is facilitated by the introduction of methyl-branching as the tertiary substituted carbocations induce a lower activation energy that results in more intense UV-Vis absorption spectra. During alkene transformation, the pronounced zeolite darkening and the intense UV-Vis absorption advocate for a more facile reactivity that, in the zeolite pores, generates marked carbonaceous deposits. Here, the growth of low-condensed conjugated compounds into larger delocalized polyaromatics is noted and increases with increasing olefin carbon number.^[11, 20, 44, 51] Alkyl-branching induces a less severe catalyst darkening with coke compounds that have more restricted molecular dimensions.

5.3.3 In-situ polarization dependent UV-Vis micro-spectroscopy

A selection of the reactants under investigation, more precisely 1-pentene and 2-methyl-2-pentene, has been further analyzed in a separate set of experiments where the formation of carbonaceous deposits was monitored by applying polarization dependent UV-Vis micro-spectroscopy. Previous chapters indicated that the use of polarized light in optical micro-spectroscopy enables the visualization of UV-Vis absorbing species, which are aligned within the straight channels of the H-ZSM-5 zeolite.^[32, 33, 52] For that reason, the mentioned C5 and C6 olefins were converted, while using a polarizer orientation that was horizontal (along the straight channels) and vertical (perpendicular to the straight channels) with respect to the examined zeolite. The obtained results are shown in Figure 5.5.

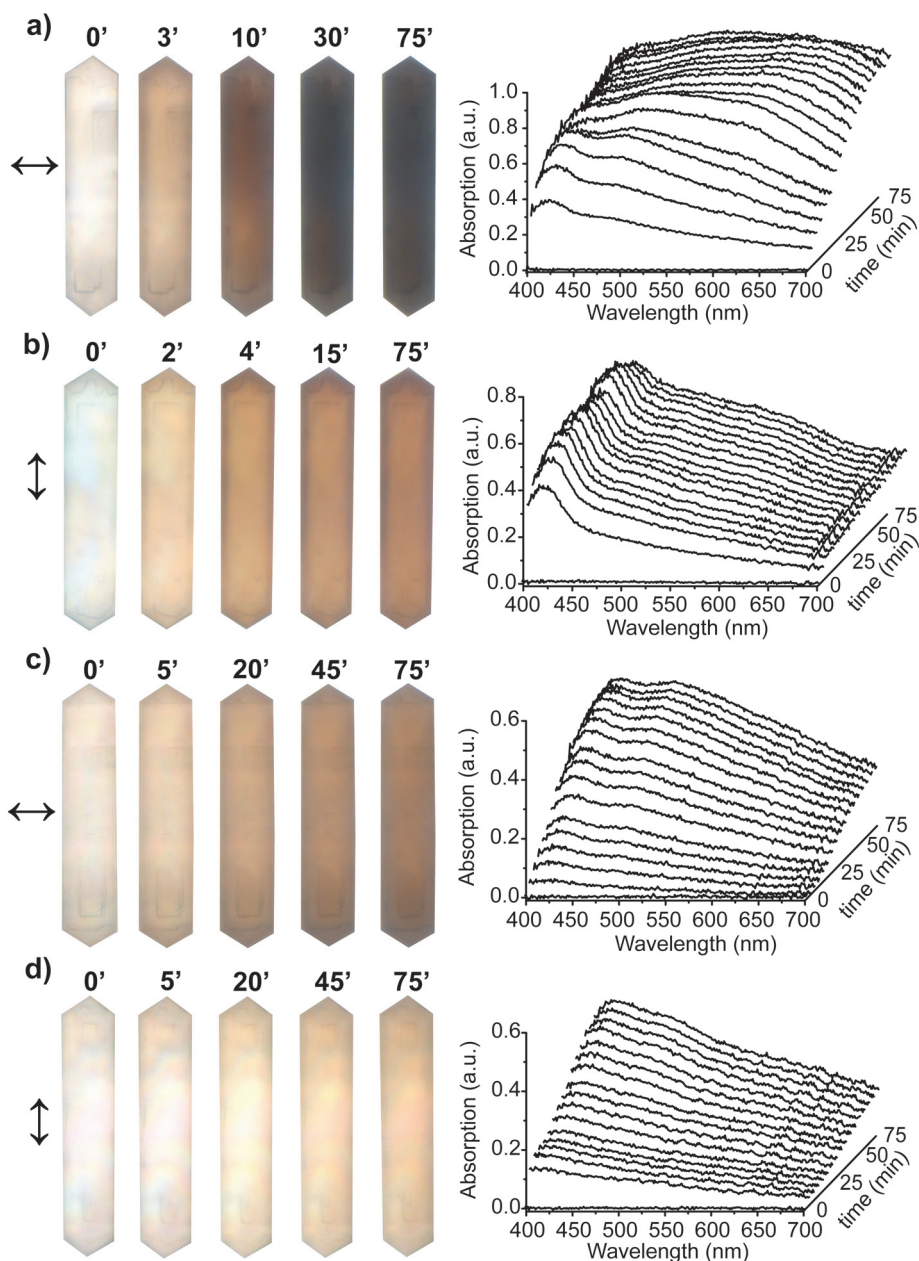


Figure 5.5: Selection of polarization dependent microphotographs with corresponding UV-Vis absorption measurements taken during aromatization at 773 K with 1-pentene (a, b) and 2-methyl-2-pentene (c, d). The polarization direction is indicated with the arrows.

When the polarizer is aligned with the straight channels (Figure 5.5a and c) a strong zeolite darkening is obtained, whereas a 90° rotation of the polarizer (Figure 5.5b and d) results in a remarkable lighter tint of the zeolite crystal. The corresponding time-resolved UV-Vis absorption measurements reflect these observations. In case of the linear 1-pentene (Figure 5.5a), a horizontal polarization alignment results in an intense UV-Vis absorption band at 500 nm that broadens towards 600 nm with progressing reaction time. As this band is assigned to the π - π^* transitions of extended coke molecules, their pronounced absorption with this polarizer orientation suggests their macroscopic alignment within the straight zeolite pores. With a 90° rotation of the polarizer (Figure 5.5b), the lack of alignment with the straight pores introduces a larger contribution from the smaller sinusoidal channels and channel intersections. Here, the large coke molecules no longer provide a prominent contribution to the overall UV-Vis absorption spectrum and the 420 nm band, originating from small aromatic species, is most dominant. Methylation of the olefinic reactant gives similar results. Again a limited red-shift with minor broadening suggests a restricted coke growth. Interestingly, a relatively intense 500 nm absorption band with respect to the 400 nm is detected with both polarization directions. The use of polarized light indicates that the growth of small coke species towards larger carbonaceous deposits occurs in the straight channels. The coke species build up in the case of linear olefins, whereas branched olefins generate coke compounds of similar molecular dimension that more homogeneously locate throughout the zeolite pores.

5.3.4 In-situ confocal fluorescence microscopy study

To elucidate the spatial development of the coke compounds within an individual H-ZSM-5 zeolite crystal, an in-situ confocal fluorescence microscopy study has been performed. The fluorescent coke molecules and their precursors that form during the conversion of pentane, 1-pentene, 2-methylpentane and 2-methyl-2-pentene are thereby investigated. A selection of the obtained images is displayed in Figure 5.6. These confocal images were collected during reaction from the crystal middle plane section by using a 561 nm laser excitation wavelength with detection window at 575-635 nm.

All reactants cause the formation of fluorescent coke compounds at the zeolite edge as soon as the reaction is initiated. With the further addition of paraffin hydrocarbons (Figures 5.6a and c), the presence of fluorescent species near the zeolite surface is most evident. For both pentane and 2-methylpentane, the moderate fluorescence detected in the inner region of the H-ZSM-5

crystal indicates a rather unaffected internal hourglass subunit. This result is interesting as it shows that despite the lack of visible coke formation, these paraffin hydrocarbons do react near the catalyst surface.

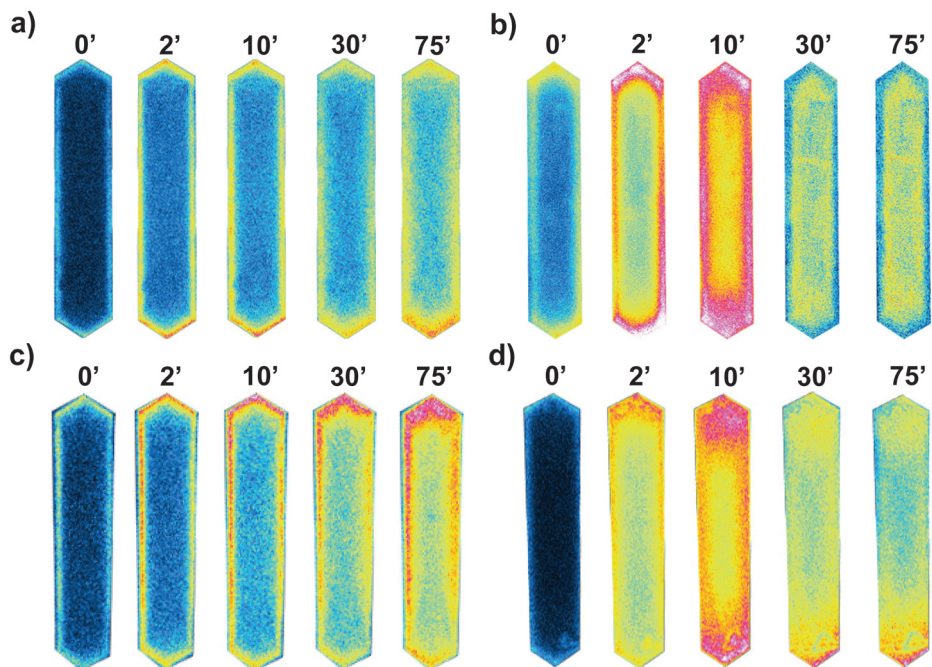


Figure 5.6: In-situ confocal fluorescence microscopy images of the H-ZSM-5 crystals taken during the aromatization process at 773 K of (a) pentane, (b) pentene, (c) 2-methylpentane and (d) 2-methyl-2-pentene. The pictures are displayed in false color (intensity mode) and the corresponding time is indicated in min.

In the case of 1-pentene and 2-methyl-2-pentene (Figures 5.6b and d), strong fluorescence starts at the crystal edge and with time-on-stream fluorescent species spread inside the crystal too. The fluorescence build-up remains dominant near the crystal surface area and diminishes with progressing conversion. This finding might be the result of internal secondary reactions or external pore blocking. The less fluorescent edge, obtained with 1-pentene, advocates for the accumulation of extended coke molecules that, due to their size, are outside the detection region and might cause pore blockage. The absence of distinctive crystal subunits furthermore suggests that cracking and rearrangement reactions take place, which mask a well-known channel mismatch at their interfaces.^[35, 38, 51, 53]

5.3.5 Ex-situ confocal fluorescence microscopy study of deactivated H-ZSM-5

As coke species grow, their absorption intensity at higher wavelengths increases. Different laser excitation wavelengths can therefore excite different coke species that vary in molecular size.^[27, 54] To accomplish this, a set of ex-situ confocal fluorescence microscopy experiments have been performed on the individual H-ZSM-5 zeolite crystal after 75 min of reaction. Four separate excitation wavelengths have thereby been applied. These are 405 nm (with detection region 425-475 nm), 488 nm (with detection region 510-550 nm), 561 nm (with detection region 570-620 nm) and 637 nm (with detection range 662-737 nm). The results are shown in Figures 5.7 and 5.8 for the linear and branched reactants, respectively.

The 405 nm laser excitation wavelength detects the smallest fluorescent species. With increasing wavelength, more extended carbonaceous compounds are excited and hence spatially detected within the H-ZSM-5 zeolite crystal. The coke species formed by the linear paraffins (Figures 5.7a, c and e) are, in line with previous measurements, primarily present near the crystal edge. With increasing excitation wavelength, the characteristic hourglass pattern becomes more distinctive and the same observation is made with increasing reactant size. This illustrates how the reactants transform at the crystal surface area and larger hydrocarbons experience more diffusion limitations when migrating towards the crystal centre. Linear olefinic hydrocarbons (Figures 5.7b, d and f) on the contrary generate fluorescent carbonaceous deposits that are predominantly situated within the zeolite. Small fluorescent species are hardly detected and mainly located inside the hourglass subunits. Larger compounds end up both in and around the internal hour-glass subunits together with a non-fluorescent crystal edge that indicates the former mentioned presence of delocalized conjugated molecules at the zeolite surface.

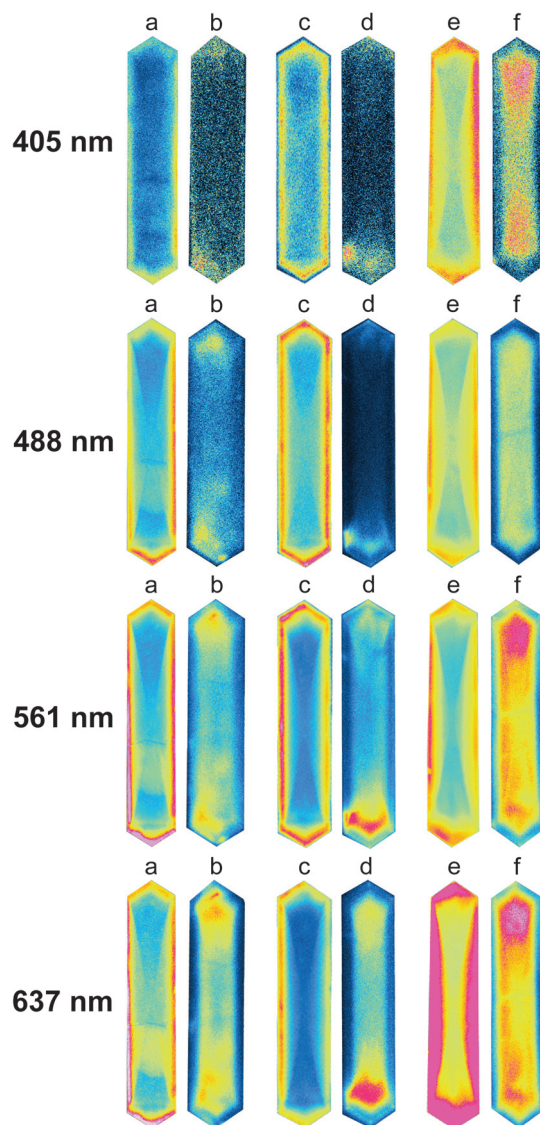


Figure 5.7: Ex-situ confocal fluorescence microscopy images of the H-ZSM-5 crystals taken after the aromatization process at 773 K with (a) butane, (b) 1-butene, (c) pentane, (d) 1-pentene, (e) hexane and (f) 1-hexene. The pictures are displayed in false color (intensity mode). The applied wavelengths are 405 nm (detection region 425-475 nm), 488 nm (detection region 510-550 nm), 561 nm (detection region 570-620 nm) and 637 nm (detection range 662-737 nm).

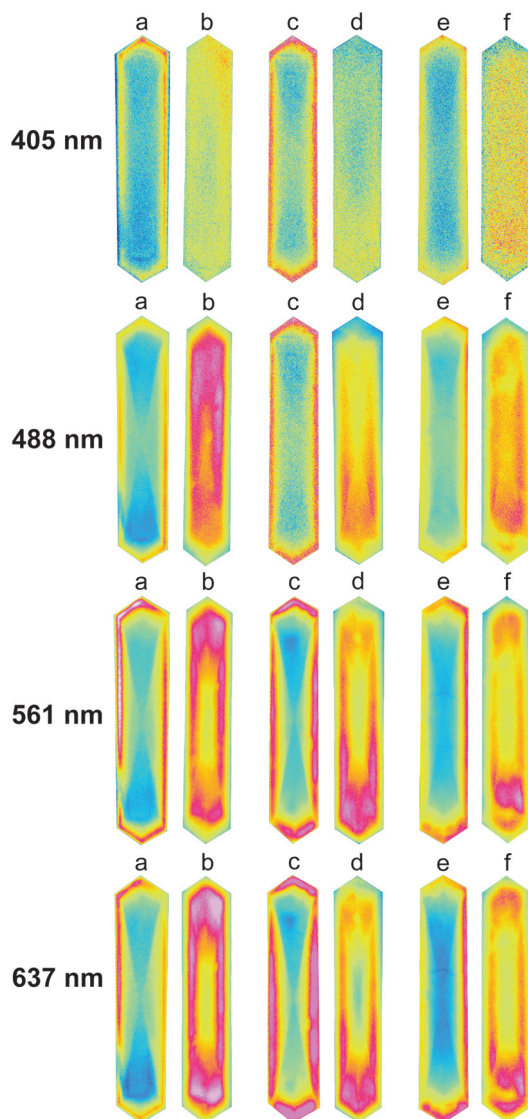


Figure 5.8: Ex-situ confocal fluorescence microscopy images of the H-ZSM-5 zeolite crystals taken after the aromatization process at 773 K with (a) 2-methylbutane, (b) 2-methyl-2-butene, (c) 2-methylpentane, (d) 2-methyl-2-pentene, (e) 2-methylhexane and (f) 2-methyl-2-hexene. The pictures are displayed in false colour (intensity mode). The applied wavelengths are 405 nm (detection region 425-475 nm), 488 nm (detection region 510-550 nm), 561 nm (detection region 570-620 nm) and 637 nm (detection range 662-737 nm).

Both branched paraffin and olefin hydrocarbons cause, compared to the linear counterparts, overall enhanced fluorescence intensity. The paraffinic reactants remain, likewise the linear alkanes, predominantly located near the zeolite surface albeit limited fluorescence is also detected inside the H-ZSM-5 crystal (Figures 5.8a, c and e). Branched olefins (Figures 5.8b, d and f) generate small fluorescent species that are rather homogeneously distributed throughout the zeolite. Increasing the laser excitation wavelength indicates that larger species are located more towards the external surface. No internal subunit mismatch is notably observed that together with the missing non-fluorescent surface illustrates the effect of the facilitated reactivity of branched olefins.

5.4. Conclusions

The coke formation that occurs during the aromatization of paraffin and olefin hydrocarbons has been investigated in a space- and time-resolved manner over individual H-ZSM-5 zeolite crystals. The conversion of paraffin reactants forms minor carbonaceous deposition, whereas pronounced coke formation is detected during olefin aromatization. Two absorption bands, located at 420 and 500 nm and assigned to aromatic and polyaromatic species, characterize the coke growth profile. During linear alkene conversion, these bands undergo a red shift and broadening thereby advocating the growth towards more extended carbonaceous deposits. Both broadening and red-shift are restricted during the conversion of branched olefins, indicating the formation of more confined coke species. Polarization dependent in-situ UV-Vis micro-spectroscopy additionally shows how large polyaromatics mainly grow within the zeolite straight channels. Confocal fluorescence microscopy reveals spatial heterogeneities of the photo-excited coke compounds. Paraffinic hydrocarbons mainly convert near the zeolite surface. Aromatization of olefinic hydrocarbons generates fluorescent species that are located within the zeolite core. The linear olefins additionally cause a non-fluorescent crystal edge that indicates the presence of extended coke compounds near the crystal external surface.

Acknowledgements

Dr. Young-Min Chung (SK Energy, South-Korea) is thanked for fruitful discussions and his active participation in this project. Dr. Machteld Mertens (ExxonMobil, Belgium) is acknowledged for providing the H-ZSM-5 zeolite crystals.

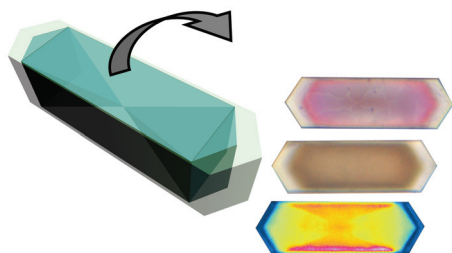
References

- [1] D.E. Gantz, J. W. Hellwege, US Patent 3756942, **1973**.
- [2] Y. Nagamori, M. Kawase, *Microporous Mesoporous Mater.* **1998**, *21*, 439-445.
- [3] Z. Musilova, N. Zilkova, S. E. Park, J. Cejka, *Top. Catal.* **2010**, *53*, 1457-1469.
- [4] S. B. He, C. L. Sun, X. Yang, B. Wang, X. H. Dai, Z. W. Bai, *Chem. Eng. J.* **2010**, *163*, 389-394.
- [5] Y. Q. Song, H. B. Li, Z. J. Guo, X. X. Zhu, S. L. Liu, X. L. Niu, L. Y. Xu, *Appl. Catal. A* **2005**, *292*, 162-170.
- [6] Y. Q. Song, X. X. Zhu, L. Y. Xu, *Catal. Comm.* **2006**, *7*, 218-223.
- [7] C. L. Yin, R. Y. Zhao, C. G. Liu, *Fuel* **2005**, *84*, 701-706.
- [8] J. M. Lopes, F. Lemos, F. R. Ribeiro, E. G. Derouane, P. Magnoux, M. Guisnet, *Appl. Catal. A* **1994**, *114*, 161-172.
- [9] M. Guisnet, P. Magnoux, *Appl. Catal. A* **2001**, *212*, 83-96.
- [10] M. Guisnet, P. Magnoux, *Appl. Catal.* **1989**, *54*, 1-27.
- [11] M. Guisnet, N. S. Gnep, F. Alario, *Appl. Catal. A* **1992**, *89*, 1-30.
- [12] M. Guisnet, N. S. Gnep, D. Aittaleb, Y. J. Doyemet, *Appl. Catal. A* **1992**, *87*, 255-270.
- [13] M. Guisnet, N. S. Gnep, *Appl. Catal. A* **1996**, *146*, 33-64.
- [14] N. S. Gnep, J. Y. Doyemet, A. M. Seco, F. R. Ribeiro, M. Guisnet, *Appl. Catal.* **1987**, *35*, 93-108.
- [15] N. S. Gnep, J. Y. Doyemet, A. M. Seco, F. R. Ribeiro, M. Guisnet, *Appl. Catal.* **1988**, *43*, 155-166.
- [16] P. Andy, N. S. Gnep, M. Guisnet, E. Benazzi, C. Travers, *J. Catal.* **1998**, *173*, 322-332.
- [17] N. Viswanadham, A. R. Pradhan, N. Ray, S. C. Vishnoi, U. Shanker, T. S. R. P. Rao, *Appl. Catal. A* **1996**, *137*, 225-233.
- [18] D. Z. Wang, X. D. Lu, X. Y. Dou, W. B. Li, C. H. Yang, *Appl. Catal.* **1990**, *59*, 75-88.
- [19] D.B. Luk'yanov, *Zeolites* **1992**, *12*, 287.
- [20] P. Magnoux, H. S. Cerqueira, M. Guisnet, *Appl. Catal. A* **2002**, *235*, 93-99.
- [21] P. C. Mihindou-Koumba, H. S. Cerqueira, P. Magnoux, M. Guisnet, *Ind. Eng. Chem. Res.* **2001**, *40*, 1042-1051.
- [22] E. E. Wolf, F. Alfani, *Catal. Rev. Sci. Eng.* **1982**, *24*, 329-371.
- [23] S. Bhatia, J. Beltramini, D. D. Do, *Catal. Rev. Sci. Eng.* **1989**, *31*, 431-480.
- [24] S. Fukase, *J. Japan Petrol. Inst.* **2000**, *43*, 1-9.
- [25] B. M. Weckhuysen, *Angew. Chem. Int. Ed.* **2009**, *48*, 4910-4943.
- [26] B.M. Weckhuysen (Ed.), *In-Situ Spectroscopy of Catalysts*, American Scientific Publishers, Stevenson Ranch, **2004**.
- [27] G. De Cremer, B. F. Sels, D. E. De Vos, J. Hofkens, M. B. J. Roeffaers, *Chem. Soc. Rev.* **2010**, *39*, 4703-17.
- [28] L. Espinosa-Alonso, K. P. de Jong, B. M. Weckhuysen, *Phys. Chem. Chem. Phys.* **2010**, *12*, 97-107.
- [29] Y. J. Jiang, J. Huang, V. R. R. Marthala, Y. S. Ooi, J. Weitkamp, M. Hunger, *Microporous Mesoporous Mater.* **2007**, *105*, 132-139.

- [30] E. Stavitski, M. H. F. Kox, I. Swart, F. M. F. de Groot, B. M. Weckhuysen, *Angew. Int. Ed.* **2008**, *47*, 3543-3547.
- [31] H. Topsøe, *J. Catal.* **2003**, *216*, 155-164.
- [32] M. H. F. Kox, E. Stavitski, B. M. Weckhuysen, *Angew. Chem. Int. Ed.* **2007**, *46*, 3652-3655.
- [33] M. H. F. Kox, E. Stavitski, J. C. Groen, J. Perez-Ramirez, F. Kapteijn, B. M. Weckhuysen, *Chem. Eur. J.* **2008**, *14*, 1718-1725.
- [34] L. Karwacki, E. Stavitski, M. H. F. Kox, J. Kornatowski, B. M. Weckhuysen, *Angew. Chem. Int. Ed.* **2007**, *46*, 7228-7231.
- [35] L. Karwacki, H. E. van der Bij, J. Kornatowski, P. Cubillas, M. R. Drury, D. A. M. de Winter, M. W. Anderson, B. M. Weckhuysen, *Angew. Chem. Int. Ed.* **2010**, *49*, 6790-6794.
- [36] E. Stavitski, M. H. F. Kox, B. M. Weckhuysen, *Chem. Eur. J.* **2007**, *13*, 7057-7065.
- [37] E. Stavitski, M. R. Drury, D. A. M. de Winter, M. H. F. Kox, B. M. Weckhuysen, *Angew. Chem. Int. Ed.* **2008**, *47*, 5637-5640.
- [38] L. Karwacki, M. H. F. Kox, D. A. M. de Winter, M. R. Drury, J. D. Meeldijk, E. Stavitski, W. Schmidt, M. Mertens, P. Cubillas, N. John, A. Chan, N. Kahn, S. R. Bare, M. Anderson, J. Kornatowski, B. M. Weckhuysen, *Nature Mater.* **2009**, *8*, 959-965.
- [39] G. Spoto, F. Geobaldo, S. Bordiga, C. Lamberti, D. Scarano, A. Zecchina, *Top. Catal.* **1999**, *8*, 279-292.
- [40] P. Sazama, J. Dedecek, V. Gabova, B. Wichterlova, G. Spoto, S. Bordiga, *J. Catal.* **2008**, *254*, 180-189.
- [41] C. Paze, B. Sazak, A. Zecchina, J. Dwyer, *J. Phys. Chem. B* **1999**, *103*, 9978-9986.
- [42] I. Kiricsi, G. Tasi, H. Forster, P. Fejes, *J. Mol. Struct.* **1990**, *218*, 369-374.
- [43] D. Lesthaeghe, V. Van Speybroeck, M. Waroquier, *Phys. Chem. Chem. Phys.* **2009**, *11*, 5222-6.
- [44] F. Geobaldo, G. Spoto, S. Bordiga, C. Lamberti, A. Zecchina, *J. Chem. Soc. Faraday Trans.* **1997**, *93*, 1243-1249.
- [45] H. Y. Long, X. S. Wang, W. F. Sun, *Microporous Mesoporous Mater.* **2009**, *119*, 18-22.
- [46] D. B. Lukyanov, N. S. Gnep, M. R. Guisnet, *Ind. Eng. Chem. Res.* **1995**, *34*, 516-523.
- [47] D. B. Lukyanov, N. S. Gnep, M. R. Guisnet, *Ind. Eng. Chem. Res.* **1994**, *33*, 223-234.
- [48] D. Shee, A. Sayari, *Appl. Catal. A* **2010**, *389*, 155-164.
- [49] A. de Klerk, R. J. J. Nel, *Ind. Eng. Chem. Res.* **2007**, *46*, 7066-7072.
- [50] K. R. Devoldere, G. F. Froment, *Ind. Eng. Chem. Res.* **1999**, *38*, 2626-2633.
- [51] O. C. Gobin, S. J. Reitmeier, A. Jentys, J. A. Lercher, *J. Phys. Chem. C* **2009**, *113*, 20435-20444.
- [52] F. Marlow, K. Hoffmann, G. G. Lindner, I. Girnus, G. van de Goor, J. Kornatowski, J. Caro, *Micropor. Mater.* **1996**, *6*, 43-49.
- [53] J. Huang, Y. J. Jiang, V. R. R. Marthala, A. Bressel, J. Frey, M. Hunger, *J. Catal.* **2009**, *263*, 277-283.
- [54] L. Karwacki, B. M. Weckhuysen, *Phys. Chem. Chem. Phys.* **2011**, *13*, 3681-3685.

Chapter 6

Catalyst Deactivation of Core-Shell H-ZSM-5/Silicalite-1 Composites as studied at the Individual Particle Level



Silicalite-1 covering H-ZSM-5 zeolite crystals affects the coke formation process. This influence is investigated in a space- and time-resolved manner during the styrene oligomerization, the methanol-to-olefin conversion and the aromatization of light-naphtha derivatives with in-situ optical and confocal fluorescence microscopy.

6.1 Introduction

Zeolites are commonly used catalysts in the petrochemical industry. The acid sites in these crystals account for their catalytic activity, whereas the well-defined pore architecture is responsible for size and shape selectivity.^[1-3] H-ZSM-5 is a frequently used zeolite that contains the MFI-type structure, which is characterized by $5.6 \times 5.3 \text{ \AA}$ straight channels intersected with $5.3 \times 5.1 \text{ \AA}$ sinusoidal pores.^[3-5] This inner channel architecture greatly determines the catalytic activity and selectivity properties. The influence of external surface properties, like an acidic pore-mouth environment or external acid sites, can however not be neglected.^[6-11] These surface characteristics can promote side reactions and the absence of pore restrictions can influence the catalyst selectivity. Therefore, many studies currently aim at reducing undesired external surface contributions. The alteration of acidic properties and the introduction of mesoporosity are thereby mostly explored and mainly involve post-synthetic modification of the catalyst.^[12-17]

Recent progress demonstrated that the zeolite surface can be modified via a one-step synthesis in which core-shell H-ZSM-5/silicalite-1 composites are obtained.^[18] This MFI-type crystalline material contains an acidic H-ZSM-5 zeolite core covered with a catalytically inactive silicalite-1 shell, as illustrated in Figure 6.1. The employed fluoride based crystallization process results in well-defined crystals and the size of these crystallites, as well as the thickness of the external layer, can be varied by tuning the synthesis solution composition.^[18]

Surface modifications like the external coverage can however influence the zeolite molecular transport properties and several analytical tools are currently employed to examine this effect.^[19-24] In order to elucidate how the external silicalite-1 shell affects the catalytic behavior of the core H-ZSM-5 crystals, the use of in-situ micro-spectroscopic techniques, featuring micrometer spatial resolution, can be very valuable.^[25-33] In this Chapter we investigate core-shell H-ZSM-5/silicalite-1 composites during styrene oligomerization, methanol-to-olefin (MTO) conversion and light naphtha aromatization (LNA) using in-situ UV-Vis and confocal fluorescence micro-spectroscopic techniques. It will be shown that an inactive external shell reduces the formation of extended carbonaceous deposits, while the internal structural mismatch causes molecular diffusion barriers that allow the build-up of coke species.

6.2 Experimental

6.2.1 Methods

UV-Vis micro-spectroscopy

As described in previous Chapters, the UV-Vis micro-spectroscopic setup is based on an Olympus BX41 upright research microscope with a 50×0.5 NA high-working-distance microscope objective lens.^[26, 32] A 75 W Xenon lamp was used for illumination. The microscope was equipped with a 50/50 double viewport tube, which accommodated a CCD video camera (ColorView Illu, Soft Imaging System GmbH) and an optical fiber mount. A 200 μm-core fiber connected the microscope to a CCD UV/Vis spectrometer (AvaSpec-2048TEC, Avantes BV). A rotatable polarizer was introduced between the objective lens and detector to separate the desirable light polarization.

Confocal fluorescence microscopy

In-situ confocal fluorescence microscopy studies were performed with a Nikon Eclipse LV150 upright microscope equipped with Nikon D-Eclipse C1 head connected to the laser light sources (488 and 561 nm). The emission was detected with a photomultiplier tube in the 510-550 nm and 575-635 nm range, respectively.^[34] Confocal fluorescence microscopy measurements were carried out at the middle horizon plane parallel to the upper plane in the crystal center. Ex-situ confocal fluorescence microscopy studies were performed using a Nikon Eclipse 90i upright microscope with a 50×0.55 NA dry objective lens. Confocal fluorescence microscopy images were collected by a Nikon A1-SHR A1 R scan head connected to laser light sources with emission wavelengths of 405, 488, 561 and 637 nm. The emission was detected by an A1-DU4 4 detector unit. The used detection ranges were 425-475 nm, 510-550 nm, 570-620 nm and 662-737 nm, respectively.

In-situ cell

All experiments were performed in an in-situ cell (Linkam FTIR 600) equipped with a temperature controller (Linkam TMS 93). The calcined crystals were heated to 773 K at the rate of 10 K·min⁻¹ and kept at this temperature for 1 h under inert atmosphere in order to remove retained water. Subsequently, the temperature was brought to the desired reaction temperature at the rate of 10 K·min⁻¹ after which the N₂ flow was diverted through a bubbler containing the reactant under investigation, thereby acting as carrier gas.

6.2.2 Materials

The core-shell H-ZSM-5/silicalite-1 composite material were synthesized according to a previous reported procedure.^[18] The sample under investigation (Figure 6.1) has 50×15×15 μm dimensions and a Si/Al ratio of 88.

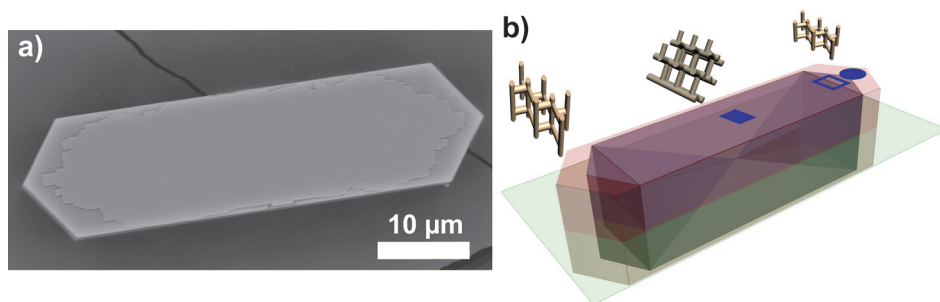


Figure 6.1: Scanning Electron Micrograph (SEM) of the core-shell H-ZSM-5/silicalite-1 zeolite crystal under study (a). The proposed intergrowth structure, the corresponding pore orientations, the middle plane at which confocal fluorescence microscopy measurements have been performed and the three regions measured by UV-Vis micro-spectroscopy i.e. the H-ZSM-5 core (-■-), the H-ZSM-5/silicalite-1 boundary (-□-) and the silicalite-1 external shell (-●-), are schematically illustrated in (b).

The silicalite-1 layer thickness is close to 3 μm on the c-axis as revealed by Si and Al X-ray emission mappings obtained by SEM analysis. XRD confirms the well-defined MFI-type structure.^[18] Pentane (99%, Acros Organics), 1-pentene (98%, Acros Organics), 2-methylpentane (99%, Sigma-Aldrich), 2-methyl-2-pentene (99%, Fluka), 2-chlorostyrene (99%, Acros Organics), 3-chlorostyrene (98%, Acros Organics), 4-chlorostyrene (97%, Acros Organics), 3,4-dichlorostyrene (97%, Acros Organics), 4-methoxystyrene (96%, Acros Organics), 4-fluorostyrene (98%, Acros Organics) and methanol (98%, Interchem) were used as received without further purification.

6.3 Results and discussion

6.3.1 Brønsted acidity and reactivity

The investigation of styrene oligomerization with micro-spectroscopic methods allows the mapping of carbocationic intermediates at the individual particle level.^[25, 26] This sensitive probe reaction is applied to detect spatial inhomogeneities regarding catalyst activity and selectivity, which allow to comprehend the crystal characteristics.^[25, 26, 32] In this work, the exposure of the micron-sized core-shell H-ZSM-5/silicalite-1 composites crystals to different liquid styrene derivatives occurs at room temperature for 5 min. Consecutive heating of the crystal, up to 373 K, allows the monomers to enter the acidic zeolite core and to oligomerize. After 10 min, the sample is cooled down to room temperature and subjected to micro-spectroscopic analysis. The use of the probe molecules 2-chlorostyrene, 3-chlorostyrene, 4-chlorostyrene

and 3,4-dichlorostyrene allows to verify the accessibility and reactivity of the H-ZSM-5 core. The use of 4-methoxystyrene and 4-fluorostyrene additionally allows investigating the zeolite acidic properties, as the different substituents have different reactivity and 4-fluorostyrene requires stronger Brønsted acid sites compared to 4-methoxystyrene.^[25, 26, 32, 33]

The formation of the oligomeric carbocations in the zeolite results in characteristic color changes that depend on the styrene substituent. An overview of the measured UV-Vis absorption bands is given in Table 6.1 and a selection of the optical microphotographs are shown in Figure 6.2.

Table 6.1: Position of the absorption bands of the styrene derivatives under study. These absorption bands are measured at the silicalite edge, the H-ZSM-5/silicalite-1 boundary and the H-ZSM-5 core, as indicated in Figure 6.1.

Compound	Band position (nm)		
	ZSM-5 center	ZSM-5/silicalite-1 boundary	silicalite-1 shell
2-chlorostyrene	525, 575	525, 575	N/A
3-chlorostyrene	480	450, 480, 550	N/A
4-chlorostyrene	425, 540, 590, 630	540, 590, 630	N/A
3,4-dichlorostyrene	525, 570	570	N/A
4-fluorostyrene	515, 560, 605	515, 560, 605	N/A
4-methoxystyrene	425, 575, 630	425, 585, 630	585, 630

Figure 6.2 shows that the formation of styrene oligomers does not uniformly occur throughout the entire crystal. The coloration of the H-ZSM-5 core combined with the relative colorless silicalite-1 shell confirms reactant accessibility towards the zeolite core and its intrinsic conversion once in an acidic environment. The addition of ortho-, meta- and para-substituted chlorostyrene gives similar results. Bulky 3,4-dichlorostyrene has more difficulty to penetrate through the silicalite-1 layer that, together with minor reactivity, gives less intense crystal coloration.

In line with previous studies, a 0° polarizer orientation (perpendicular to the long axis of the crystals, denoted by the horizontal arrow) gives stronger coloration compared to the 90° orientation of the polarizer (denoted by the vertical arrow).^[25, 26, 32] This polarization dependency can be explained by the alignment of the oligomeric reaction products within the straight H-ZSM-5 channels. The polarization behavior of the core-shell composites is similar to that of the previously studied MFI-type crystals lacking the silicalite-1 coating thereby suggesting a comparable crystal architecture.^[25, 26, 32]

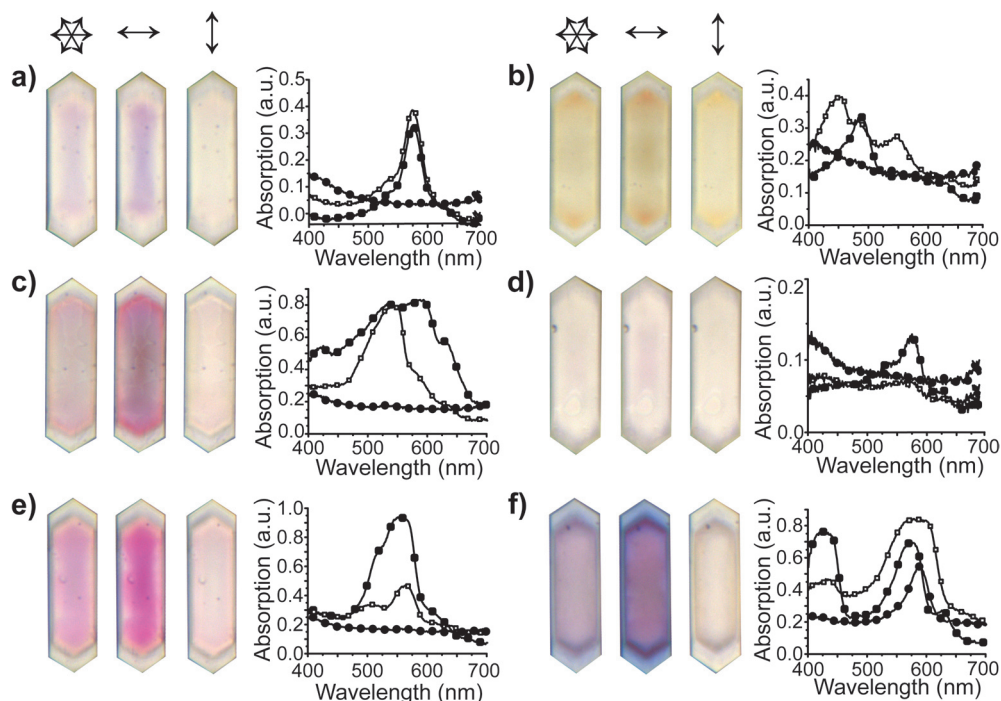


Figure 6.2: Optical microphotographs of the core-shell H-ZSM-5/silicalite-1 crystals after oligomerization at 373 K of (a) 2-chlorostyrene, (b) 3-chlorostyrene, (c) 4-chlorostyrene, (d) 3,4-dichlorostyrene, (e) 4-fluorostyrene and (f) 4-methoxystyrene. The images were taken with and without the use of polarized light. The polarization directions are indicated by the arrows. The corresponding UV-Vis absorption spectra are measured with the 0 degree (\leftrightarrow) light polarization at the H-ZSM-5 core (\blacksquare), the H-ZSM-5/silicalite-1 boundary (\square) and the silicalite-1 external shell (\bullet), as illustrated in Figure 6.1b.

For further verification, UV-Vis absorption spectra have been measured at three separate positions in the H-ZSM-5/silicalite-1 composite as outlined in Table 6.1 and Figure 6.2. These three regions are the H-ZSM-5 zeolite core, the H-ZSM-5/silicalite-1 interface and the external silicalite-1 shell as schematically illustrated in Figure 6.1b. The measured absorption bands originate from the oligomer π - π^* transitions and are mainly assigned to the dimeric and trimeric carbocations where an increasing wavelength is explained in terms of a larger conjugated system.^[25, 26, 32, 35]

Upon oligomerization of 4-chlorostyrene (Figure 6.2c), the characteristic hour-glass shaped internal crystal subunit colors purple. This region generates an intense absorption with bands located at 540 nm, 590 nm and 630 nm. These bands equal those measured earlier on MFI-type zeolites

lacking the silicalite-1 shell, although differences in relative band intensity are observed.^[25, 26, 32] The first two absorption bands are therefore assigned to the cyclic and linear carbocationic dimer, while higher wavelengths originate from larger trimeric species. The apparent pink interface between the core H-ZSM-5 and the external silicalite-1 shell, is characterized by oligomers that are predominantly dimeric in nature. This is also in agreement with former studies, while the absence of conjugated oligomers in the external shell is due to a deficiency of Brønsted acid sites. Changing the styrene substituent permits to analyze changes in conversion reactivity. As methoxystyrene is less electronegative, it can be more reactive compared to the chloro and fluoro counterparts.^[25, 26, 32] The strong electron-withdrawing fluoride (Figure 6.2e) provides results that are in reasonable agreement with previous studies.^[25, 26, 32] Here, the characteristic absorptions at 515, 560 and 605 nm, assigned to dimeric and trimeric oligomers, are dominant in the zeolite core. At the H-ZSM-5/silicalite-1 boundary, the presence of oligomers containing a 560 nm absorption band coincides with measurements performed on H-ZSM-5 lacking the silicalite-1 shell. From Figure 6.2f it is noted that the less electronegative 4-methoxystyrene also oligomerizes within the silicalite-1 layer. This is likely the result of a small amount of Brønsted acid sites located in the external shell. Their presence might be related to the one-step synthesis of the core-shell composites that results in a major presence of aluminum in the acid H-ZSM-5 core although with possible minor aluminum amounts in the external shell as well. As a consequence of this aluminum zoning, an acidity gradient occurs that allows oligomerization of the highly reactive 4-methoxystyrene in this overall non-catalytic external layer. The purple core provides absorption bands at around 575 and 630 nm, confirming previous oligomerization data.^[25, 26, 32] The interface region has an intense absorption, while the 585 nm band detected at the external silicalite-1 layer advocates for the presence of dimeric oligomer species.

In a next series of experiments we have examined the core-shell H-ZSM-5/silicalite-1 composites that are exposed to the various styrene derivatives with confocal fluorescence microscopy. The application of four different excitation wavelengths i.e. 405, 488, 561 and 637 nm, assists the distinction of oligomers varying in their size since their absorption band positions correlate with the product molecular dimensions. The results are shown in Figure 6.3.

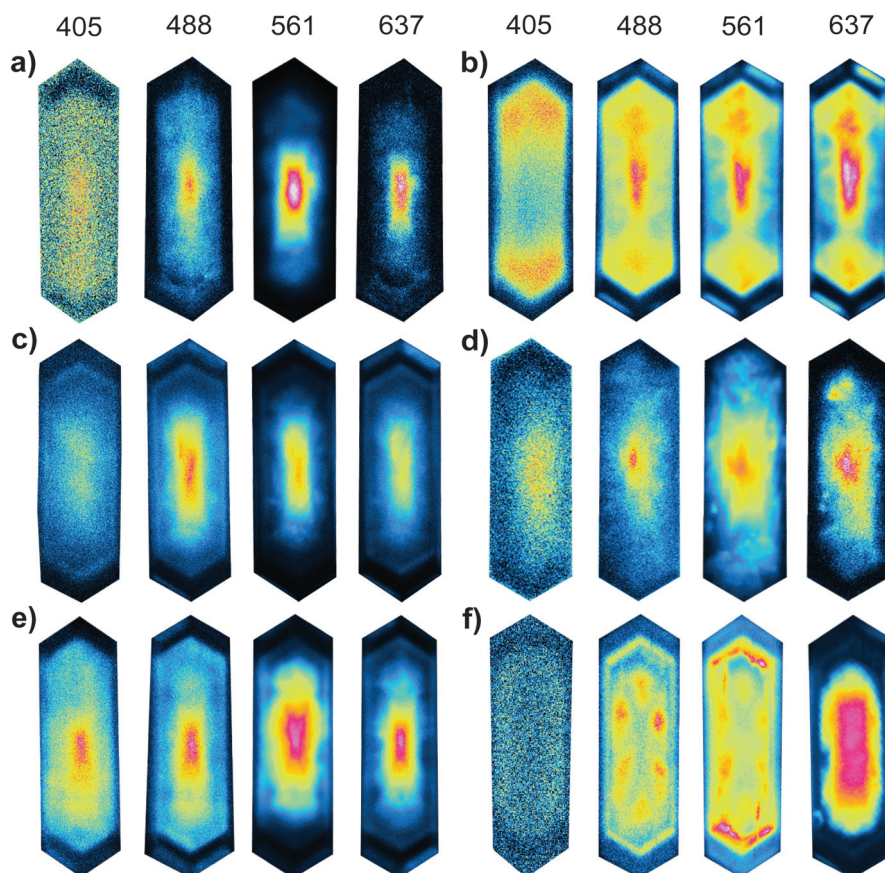


Figure 6.3: Confocal fluorescence microphotographs of the core-shell H-ZSM-5/silicalite-1 crystals after oligomerization at 373 K with (a) 2-chlorostyrene, (b) 3-chlorostyrene, (c) 4-chlorostyrene, (d) 3,4-dichlorostyrene, (e) 4-fluorostyrene and (f) 4-methoxystyrene. The images are taken at the middle slide plane as schematically illustrated in Figure 6.1b and the corresponding excitation wavelengths are indicated in nm.

Figure 6.3 shows a general presence of fluorescent oligomers located within the H-ZSM-5 zeolite core. Their fluorescent profile furthermore indicates that products with larger molecular size, i.e. increasing excitation wavelength, have a higher localization at the zeolite inner core. This could, in line with the previous discussion, be the result of an aluminum zoning. Small fluorescent oligomers, excited with the 405 and 488 nm laser wavelength, are more delocalized and positioned throughout the acid H-ZSM-5 core. In agreement with optical observations, no major fluorescence is detected in the external silicalite-1 layer. However, careful analysis show a fluorescent external area

of the silicalite-1 shell. The internal silicalite-1 layer remains however non-fluorescent, while additionally a pronounced core-shell interface is observed. The reasons for the non-homogeneous fluorescence of the silicalite-1 shell are speculative and could be an indication of molecular diffusion variations. The pronounced core-shell boundary is distinctive and noted for all samples. At this interface, a structural mismatch could cause diffusion barriers, which permit product build-up. Therefore, in combination with the optical findings, this noted interface region is ascribed to the accumulation of oligomers. The behavior of the H-ZSM-5/silicalite-1 composite observed with the oligomerization of 4-methoxystyrene (Figure 6.3f) is somewhat different from the oligomerization of the other probe molecules. Indeed, in the case of 4-methoxystyrene inner boundaries, located both at the H-ZSM-5 subunits and the core-shell interface, cause the pronounced accumulation of fluorescent compounds. In addition, the external silicalite-1 shell is more homogeneously fluorescent. The differences are considered the result of the higher reactivity of 4-methoxystyrene as similar observations are made on H-ZSM-5 crystals without an external silicalite-1 layer.^[25, 26, 32] Their marked detection with 488 and 561 nm excitation wavelength is furthermore in agreement with the corresponding absorption profile shown in Figure 6.2f. All findings combined confirm a rather uniform styrene conversion despite the different substituents. These oligomerizations on their turn demonstrate the ability of reactants to diffuse through the external silicalite-1 layer and to convert once inside the acid H-ZSM-5 core. A moderate acidity gradient is observed, while the structural mismatch causes the build-up of products both at the H-ZSM-5/silicalite-1 interface as well as at the internal subunit boundaries.^[22, 28-30, 34, 36]

6.3.2 Catalyst deactivation

In hydrocarbon processing, the formation of carbonaceous deposits on working catalysts is usually inevitable. These undesired coke compounds generally hamper activity and cause changes in selectivity. Previous chapters illustrated how in-situ micro-spectroscopic techniques can be valuable tools to study coke formation in a space- and time-resolved manner.^[25, 26, 31, 37, 38] These techniques are therefore applied to investigate the influence of the inactive crystalline external layer on the formation of carbonaceous deposits during the methanol-to-olefin (MTO) conversion and the conversion of light naphtha derivatives. The MTO conversion is interesting as it allows obtaining valuable chemical building blocks from oil alternative feedstocks.^[39] Here, methanol enters the acid zeolite where it forms an active catalytic scaffold. To these reaction intermediates, methanol is added and

olefins are formed in a closed catalytic cycle. However, due to secondary reactions, larger hydrocarbons form as well. These can remain retained in the zeolite pores with consequences for the catalyst performance. Aromatization of paraffins and olefins on the other hand, occurs via dehydrocyclization or via alkene rearrangements. This process is considered a promising method that allows the upgrade of low-value hydrocarbons into valuable aromatics.^[11, 40] Secondary reactions, such as cracking and oligomerization, generate undesired carbonaceous deposits and their formation vary depending on the applied reactant.

Coke formation during the Methanol-to-Olefin Conversion

Chapters 2 and 3 indicated how the nature and rate with which coke species form generally depends on the crystal framework topology, catalyst acidity and applied reaction conditions.^[37-39, 41-43] Increasing acid site density or reaction temperature usually results in the enhanced formation of larger carbonaceous deposits that, to a certain extent, are considered to be of graphite-like character located at the external zeolite surface.^[43, 45-51] The inactive external silicalite-1 layer could alleviate the generation of these deactivating compounds. Therefore, the core-shell H-ZSM-5/silicalite-1 composites were exposed to methanol vapor at 573 and 773 K. During reaction, the formation of carbonaceous deposits was temporally monitored and the results are shown in Figure 6.4.

The initially translucent crystals undergo darkening upon exposure of methanol flow, indicating the growth of undesired carbonaceous species. Comparison of Figure 6.4a and 6.4b indicates an enhanced coke formation rate with increasing reaction temperature. The increase in reaction temperature does however not notably influence the coke formation process as it ends up in comparable darkening. The formation of the carbonaceous species starts at the center of the H-ZSM-5 zeolite core and with time-on-stream the coke deposits grow towards the outer zeolite surface. These observations are somewhat contrary to the previous described studies performed on H-ZSM-5 crystals lacking an external silicalite-1 shell. Here, a coke front moving from the external surface towards the center of the zeolite was observed and an increase of the reaction temperature provided pronounced darkening.^[37, 38] Throughout the entire conversion little darkening of the external silicalite-1 layer is observed although the high reaction temperature causes a mild grayish coloration of the initially colorless shell. This advocates for a limited coke growth in the outer silicalite-1 layer. An evident H-ZSM-5/silicalite-1 boundary furthermore suggests the accumulation of coke species at this interface. The current results are explained by the presence of an

inactive external silicalite-1 layer. This shell regulates the migration of small reactants towards the zeolite core, while it limits the growth of extended coke compounds at the near surface region. A Brønsted acidity gradient causes the coke growth to initiate at the zeolite centre and channel mismatch allows the build-up of coke at the H-ZSM-5/silicalite-1 boundary region.

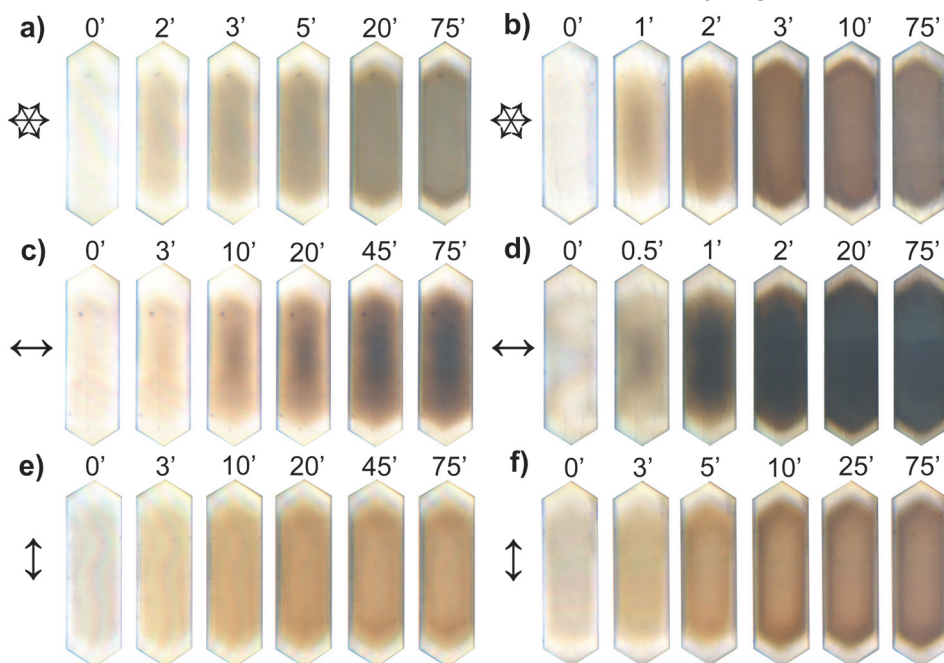


Figure 6.4: Selection of the optical microphotographs taken during the methanol-to-olefin conversion over core-shell H-ZSM-5/silicalite-1 composites at 573 K (a, c and e) and at 773 K (b, d and f). The orientation of the polarizer is noted by the arrows.

The gradual formation of carbonaceous deposits was additionally examined in a separate set of experiments by using polarization dependent optical microspectroscopy (Figures 6.4c-f). Chapter 3 showed how the use of polarized light enables to visualize coke species that are aligned within the straight channels of the MFI-type structure.^[32, 38] Therefore, a horizontal (along the straight channels) and a vertical (perpendicular to the straight channels) orientation of the polarizer, with respect to the examined zeolite crystal, were applied during the MTO conversion. Figures 6.4c and 6.4d indicate that when the light polarization coincides with the alignment of the straight pores, a strong coloration of the zeolite composite is obtained. A result that is moreover valid for both reaction temperatures. With 90° rotation (Figures 6.4e and 6.4f), the coke formation process does not start from the zeolite centre and a rather homogeneous coke growth progress is observed that ends in a

remarkable alleviated crystal coloration with a marked H-ZSM-5/silicalite-1 interface. These observations pinpoint to the macroscopic alignment of coke molecules along the short axis of the zeolite crystal. The distinct dark H-ZSM-5/silicalite-1 boundary additionally confirms the previously suggested crystallographic mismatch that results in the accumulation of carbonaceous deposits. The corresponding time-resolved UV-Vis absorption measurements, taken from a 2 μm spot in the middle of the zeolite crystal (Figure 6.1b), are shown in Figure 6.5.

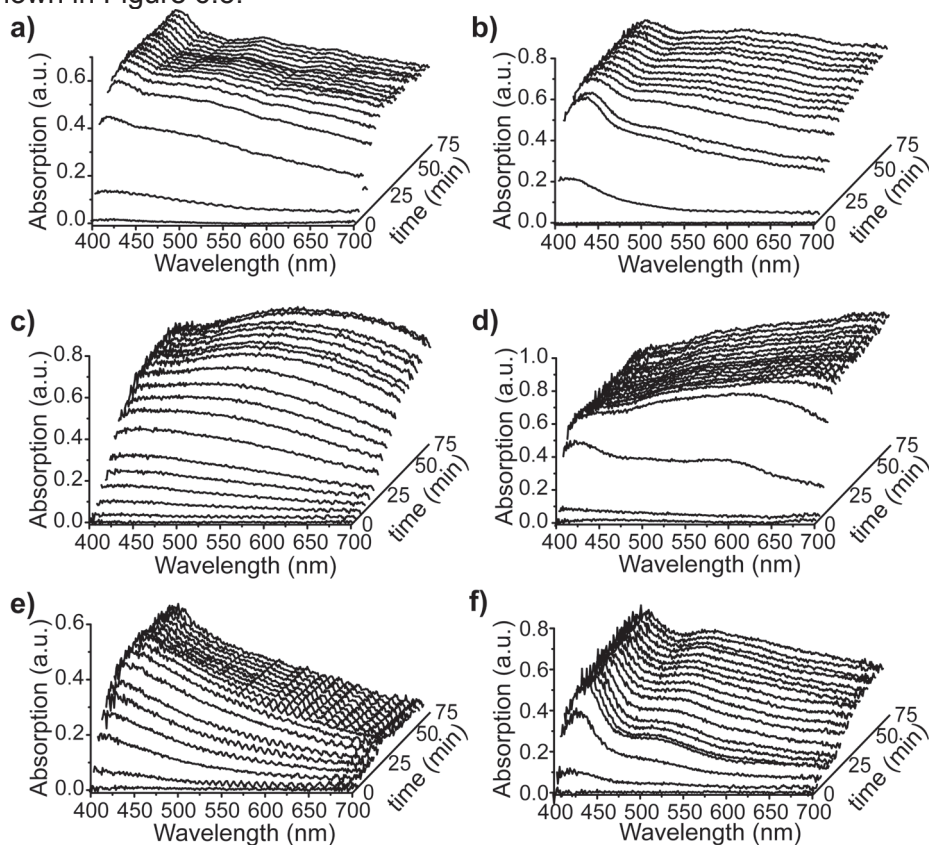


Figure 6.5: Time-resolved UV-Vis absorption spectra taken from a 2 μm spot in the middle of the core-shell H-ZSM-5/silicalite-1 composite during the MTO conversion at 573 K with (a) no polarizer, (c) horizontal polarization, (e) vertical polarization and at 773 K with (b) no polarizer, (d) horizontal polarization, (f) vertical polarization, as shown in Figure 6.4.

The coke formation generates at both temperatures an absorption band at 400 nm. This band is assigned to methyl-substituted aromatic species that constitute the active catalytic scaffold of the hydrocarbon pool

mechanism.^[35, 41, 52-58] With time on stream, this band undergoes a red shift towards 420 nm, while the formation of a second absorption band occurs at 550 nm. This second band, starts as a shoulder of the former mentioned 400 nm band and indicates the growth of coke molecules towards larger conjugated systems, that are most probably linear polyaromatic in character.^[35, 43, 59-61] With increasing reaction temperature, a faster growth of a more intense overall absorption is obtained. However, the 400 nm band remains most pronounced and the overall background absorption that stretches throughout the entire visible region remains comparable with that observed under mild reaction conditions. This illustrates that despite a more pronounced coke formation, the overall nature of the retained coke deposits is similar as the reaction temperature is raised. The marked zeolite darkening obtained with the horizontal light polarization alignment (Figures 6.4c and 6.4d) is reflected in a major UV-Vis absorption above 500 nm that, in addition, undergoes a severe red shift (Figures 6.5c and 6.5d). These bands, assigned to the π - π^* transitions of large coke molecules, indicate the growth of extended coke species in the straight pores of the zeolite crystal. These large coke molecules, on the other hand, no longer provide a prominent contribution to the absorption spectrum in case the polarizer is rotated 90° (Figures 6.5e and 6.5f). Here, the 420 nm absorption band, originating from smaller methyl-substituted aromatic species, is dominant. Although less prominent, the 500 nm absorption band is obtained with this vertical alignment, in particular when the reaction temperature is increased. The lack of alignment with the straight channels introduces a larger contribution of the zeolite sinusoidal pores and the channel intersections and the faster formation of coke deposits, as temperature is raised, induce the presence of larger compounds in these parts of the zeolite. The use of polarized light confirms the growth of small molecules towards larger deactivating coke compounds. This transformation pushes the large conformations towards the zeolite outer surface where channel mismatch at the H-ZSM-5/silicalite-1 boundary results in the build-up of carbonaceous deposits.

The zeolite composite has been subjected to an in-situ confocal fluorescence microscopy study in order to elucidate the internal spatial distribution of fluorescent coke species and their precursors during the methanol conversion at 573 K. The results are displayed in Figure 6.6 where the confocal fluorescence microscopy images of the middle plane section of the H-ZSM-5/silicalite-1 crystals (Figure 6.1b) taken during reaction are shown. These images were collected using 488 and 561 nm laser excitation wavelength with a detection window at 510-550 and 575-635 nm, respectively.

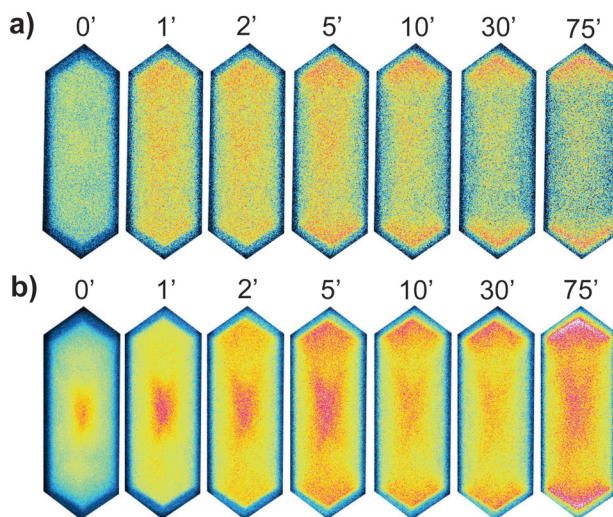


Figure 6.6: Confocal fluorescence microscopy images obtained during the methanol-to-olefin conversion at 573 K with (a) 488 nm and (b) 561 nm laser excitation. The images are taken from the middle plane section of the zeolite as schematically illustrated in Figure 6.1b.

Fluorescent compounds are detected throughout the acid H-ZSM-5 core as soon as the reaction is started. Small fluorescent species, detected with 488 nm laser excitation wavelength, are initially rather homogeneously spread throughout the catalyst and with progressing conversion, their presence becomes more pronounced inside the hourglass sub-unit. Larger compounds, detected with the 561 nm excitation wavelength, readily illustrate an intensity gradient with a maximum at the core. With the further addition of methanol, a fluorescent front moves towards the zeolite external surface while the fluorescent compounds predominantly locate within the internal hourglass sub-unit. This process terminates with high fluorescence activity in the roof-edged ends of the acid H-ZSM-5 core. Moreover, throughout the methanol conversion process, minor fluorescence of the external silicalite-1 shell is observed. The sharp edge that separates the fluorescent acid H-ZSM-5 core from the less-fluorescent silicalite-1 shell confirms the coke growth mechanism, originating from the zeolite centre, that results in coke deposits accumulated at the H-ZSM-5/silicalite-1 boundary.

Coke formation during light cracked naphtha aromatization.

Naphtha consists of a large variety of paraffinic and olefinic hydrocarbons. To assess the effect of the different reactants onto the coke formation, a selection of light cracked naphtha components, i.e. pentane, 1-pentene,

2-methylpentane and 2-methyl-2-pentene, have been individually exposed to the core-shell H-ZSM-5/silicalite-1 composites at 773 K.

The exposure of both linear and branched C5 paraffin reactants provides negligible darkening of the zeolite composite. A slight absorption around 400 nm with minor broadening towards higher wavelengths is thereby obtained. These results are shown in Figure 6.7 and in accordance to the data illustrated in Chapter 5.^[62]

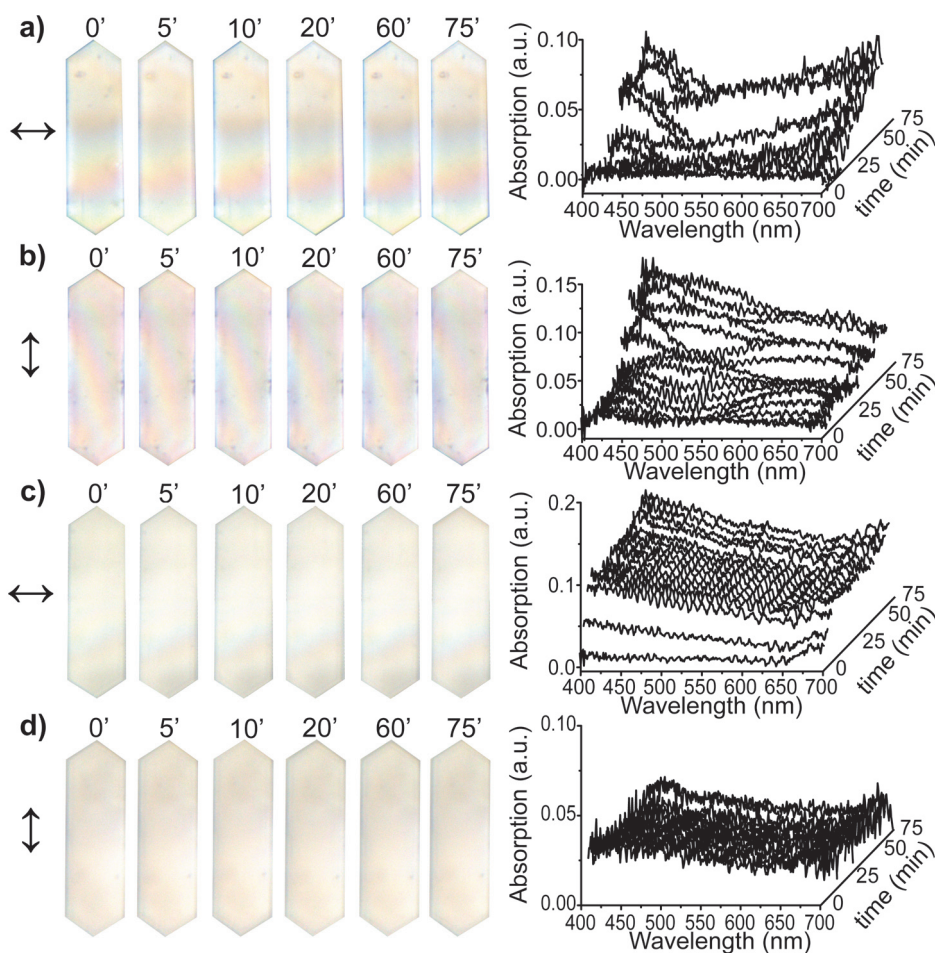


Figure 6.7: Selection of polarization dependent optical microphotographs of the core-shell H-ZSM-5/silicalite-1 zeolite crystals taken during the aromatization process at 773 K with: pentane (a, b) and 2-methylpentane (c, d). The orientation of the polarizer is noted by the arrows. The corresponding time-resolved absorption measurements are taken from a 2 μm spot in the middle of the zeolite.

The olefin counterparts cause pronounced coloration of the catalyst. This darkening is strongly polarization dependent as illustrated in Figure 6.8.

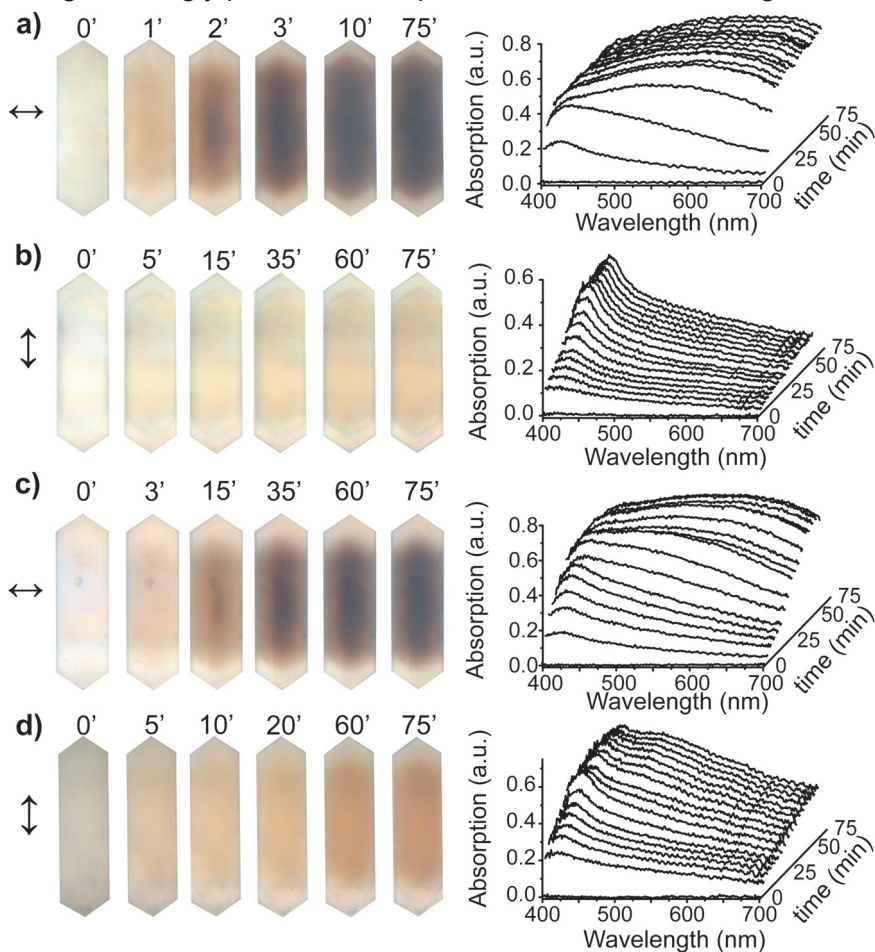


Figure 6.8: Selection of polarization dependent optical microphotographs of the core-shell H-ZSM-5/silicalite-1 zeolite crystals taken during the aromatization process at 773 K with: 1-pentene (a, b) and 2-methyl-2-pentene (c, d). The orientation of the polarizer is noted by the arrows. The corresponding time-resolved absorption measurements are taken from a 2 μm spot in the middle of the zeolite.

Linear alkenes cause a fast darkening of the acidic H-ZSM-5 core. In alignment with the straight zeolite pores, illustrated by the horizontal arrow in Figure 6.8a, a pronounced coke formation starts at the centre of the zeolite composite and quickly spreads towards the external silicalite-1 layer. A 90° rotation of the polarizer (Figure 6.8b) results in reduced homogeneous coloration of the

H-ZSM-5 core, suggesting the absence of extended carbonaceous compounds in the sinusoidal pores. Similar results are obtained with the introduction of methyl-branching although here the formation of carbonaceous deposits occurs at a reduced rate (Figures 6.8c and 6.8d). Throughout the conversion, a limited darkening of the H-ZSM-5/silicalite-1 interface is observed for both alkene reactants and especially for the branched hydrocarbons. The absence of a distinct core-shell boundary suggests that, in contrast to the MTO conversion, a restricted accumulation of coke deposits occurs in this area. The time-resolved absorption measurements taken from the middle of the zeolite reflect these observations. It is noted that when the polarizer is aligned with the straight zeolite pores, the olefin hydrocarbons give rise to intense UV-Vis absorption. The 420 nm absorption band initiates the coke formation process and the growth of a second band follows at around 500 nm. This 500 nm band intensifies and undergoes a major red-shift towards 650 nm in case of linear reactants (Figure 6.8a). Branched olefins however generate less severe broadening with a more restricted red-shift that ends around 600 nm (Figure 6.8c). A 90° rotation of the light polarization (Figures 6.8b and 6.8d) results in a prominent 420 nm absorption band. The branched alkenes additionally allow the growth of larger coke species in the sinusoidal pores and channel intersections, as detected by the distinct shoulder at around 500 nm. Here, the 500 nm band undergoes a limited broadening and the 420 nm absorption band remains most indicative throughout the entire conversion. The introduction of methyl-branching introduces tertiary substituted carbocations, which facilitate the olefin conversion by lowering the activation energy. The intensity of the absorption bands is however similar to that obtained with linear reactants. This advocates for a minor influence of the external silicalite-1 layer on the accessibility of the branched alkenes. The slow coke formation rate combined with the confined broadening of the UV-Vis absorption bands furthermore suggests that the coke deposits formed during the aromatization of branched hydrocarbons are more constrained in size, even though larger deposits spread-out in the sinusoidal pores of the zeolite.

The confocal fluorescence microscopy images, that are taken after aromatization, show distinct coke patterns between alkane and alkene feeds. These results are shown in Figure 6.9.

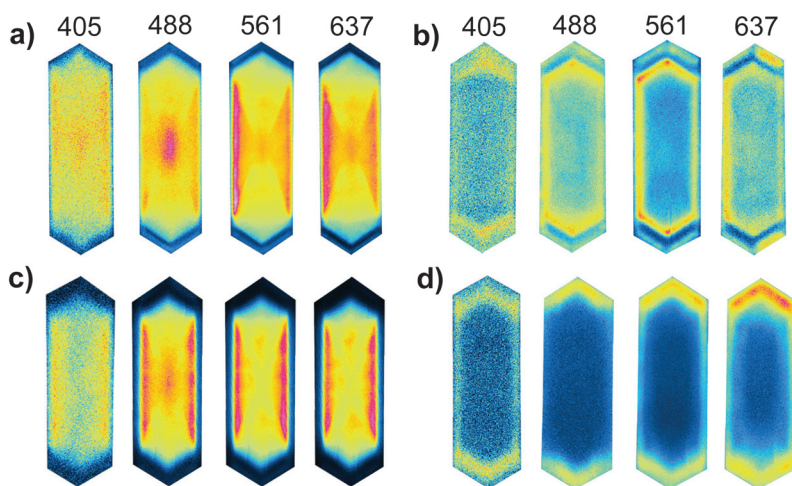


Figure 6.9 Ex-situ confocal fluorescence microscopy images of the core-shell H-ZSM-5/silicalite-1 crystals. The middle plane slice is recorded as schematically illustrated in Figure 6.1b. The images are taken after the aromatization process at 773 K with (a) pentane, (b) 1-pentene, (c) 2-methylpentane and (d) 2-methyl-2-pentene. The pictures are displayed in false color (intensity mode). The applied wavelengths are 405 nm (detection region 425–475 nm), 488 nm (detection region 510–550 nm), 561 nm (detection region 570–620 nm) and 637 nm (detection range 662–737 nm).

From Figures 6.9a and 6.9c, it is noted that although paraffin reactants do not cause optically visible crystal darkening, these hydrocarbons do form fluorescent species. Here, both pentane and 2-methylpentane show a fluorescent H-ZSM-5 core and minor fluorescence is detected in the outer silicalite-1 shell. These results differ from previous observations, described in Chapter 5, in which paraffin reactants on H-ZSM-5 lacking an inactive silicalite-1 shell, caused fluorescent coke species primarily present near the crystal edge.^[62] However, in line with these former experiments, varying excitation wavelength illustrates the difficulty for larger coke species to migrate towards the crystal core and the most intense fluorescence is detected outside the hour-glass subunit. In the case of olefins (Figure 6.9b and 6.9d), the most intense fluorescent region is at the boundary between the H-ZSM-5 and the silicalite-1 shell, while fluorescent coke species and their precursors are mildly detected inside the zeolite core. Introduction of methyl-branching enhances this process thereby increasing the presence of fluorescent species within the external silicalite-1 shell. These results provide a correlation between the function of the silicalite-1 shell and reactant conversion activity. Alkanes, which are more difficult to activate on the zeolite acid sites, can diffuse into the acid H-ZSM-5 core where they react. The

lower activation barrier of olefins causes their rapid conversion as soon as they reach this acid core. Due to this, the build-up of long-chained species at the interface can block further access towards the H-ZSM-5 center, an effect that is more pronounced for the branched olefins.

6.4 Conclusions

UV-Vis and confocal fluorescence micro-spectroscopic techniques have been applied to investigate the crystallographic properties and catalyst deactivation of H-ZSM-5/silicalite-1 zeolite composites at the individual particle level. Oligomerization of styrene derivatives causes different crystal colorations that are characteristic for each individual styrene substituent. It shows that the external silicalite-1 shell does not affect the accessibility of the reactants to the catalytic active core, the presence of a Brønsted acidity gradient and pore mismatch at the zeolite internal interfaces.

The formation of carbonaceous deposits during the methanol-to-olefin (MTO) conversion and the light naphtha aromatization (LNA) process is hardly observed within the external silicalite-1 layer. The outer shell does however influence the nature of the coke deposits and their growth process in the neighboring H-ZSM-5 core. More specifically, during MTO reaction, the silicalite-1 shell prevents the formation of extended graphite-like coke and despite high reaction temperatures, similar absorption bands, as obtained under mild reaction conditions, indicate the formation of comparable coke species. The growth of carbonaceous compounds initiates at the center of the H-ZSM-5 zeolite core and, with time on stream, spreads throughout the entire zeolite material. This coke build-up starts with a 400 nm absorption band assigned to methyl-substituted aromatic species. A second band, starting as a shoulder of the 400 nm band, point towards the growth of larger coke systems.

Aromatization of linear and branched C5 alkanes results in a negligible darkening of the zeolite composites, whereas olefinic hydrocarbons cause pronounced coke deposition. These retained species are strongly light polarization dependent advocating an alignment of extended coke molecules within the straight zeolite pores. Introduction of methyl-branching slows down the coke formation rate and produces more confined coke compounds. Confocal fluorescence microscopy illustrates that despite the absence of visible coke deposits, an active H-ZSM-5 core results from alkane conversion. Alkene aromatization however causes an intense fluorescent H-ZSM-5/silicalite-1 boundary that prevents diffusion of these species towards the zeolite centre and causes the formation of a fluorescent silicalite-1 external shell.

Acknowledgements

Suzanna Verkleij and Dr. Eli Stavitski are thanked for their contribution to this project as well as for fruitful discussions. Dr. Antoinette Lombard, Prof. Angélique Simon-Masseron (IS2M, France) and Dr. Amandine Cabiac, Dr. Loïc Rouleau and Prof. Joël Patarin (IFP, France) are acknowledged for providing the zeolite composites.

References

- [1] A. Corma, *Chem. Rev.* **1995**, *95*, 559-614.
- [2] H. van Bekkum, E.M. Flanigen, P.A. Jacobs, J.C. Jansen (Eds.), *Introduction to Zeolite Science and Practice*, Elsevier, Amsterdam, **2001**.
- [3] H. van Bekkum, F. Bauer (Eds.), *Molecular Sieves*, Springer-Verlag, Berlin Heidelberg, **2007**.
- [4] www.iza-structure.org/database.
- [5] C. Baerlocher, W.M. Meier, D.H. Olson (Eds.), *Atlas of Zeolite Framework Types*, Elsevier, Amsterdam, **2001**.
- [6] T. Armaroli, L. J. Simon, M. Digne, T. Montanari, M. Bevilacqua, V. Valtchev, J. Patarin, G. Busca, *Appl. Catal. A* **2006**, *306*, 78-84.
- [7] A. Corma, *Micropor. Mater.* **1995**, *94*, 736-747.
- [8] F. Bleken, M. Bjorgen, L. Palumbo, S. Bordiga, S. Svelle, K. P. Lillerud, U. Olsbye, *Top. Catal.* **2009**, *52*, 218-228.
- [9] A. G. Gayubo, P. L. Benito, A. T. Aguayo, M. Olazar, J. Bilbao, *J. Chem. Technol. Biotechnol.* **1996**, *65*, 186-192.
- [10] S. Melson, F. Schuth, *J. Catal.* **1997**, *170*, 46-53.
- [11] Z. Musilova, N. Zilkova, S. E. Park, J. Cejka, *Top. Catal.* **2010**, *53*, 1457-1469.
- [12] R. W. Weber, J. C. Q. Fletcher, K. P. Moller, C. T. OConnor, *Microporous Mesoporous Mater.* **1996**, *7*, 15-25.
- [13] J. C. Groen, J. A. Moulijn, J. Perez-Ramirez, *J. Mater. Chem.* **2006**, *16*, 2121-2131.
- [14] A. B. Halgeri, J. Das, *Catal. Today* **2002**, *73*, 65-73.
- [15] J. Juan-Alcaniz, E. V. Ramos-Fernandez, U. Lafont, J. Gascon, F. Kapteijn, *J. Catal.* **2010**, *269*, 229-241.
- [16] L. Sommer, D. Mores, S. Svelle, M. Stocker, B. M. Weckhuysen, U. Olsbye, *Microporous Mesoporous Mater.* **2010**, *132*, 384-394.
- [17] J. Sun, G. S. Zhu, Y. L. Chen, J. X. Li, L. F. Wang, Y. Peng, H. Li, S. L. Qiu, *Microporous Mesoporous Mater.* **2007**, *102*, 242-248.
- [18] A. Lombard, A. Simon-Masseron, L. Rouleau, A. Cabiac, J. Patarin, *Microporous Mesoporous Mater.* **2010**, *129*, 220-227.
- [19] B. M. Weckhuysen, *Angew. Chem. Int. Ed.* **2009**, *48*, 4910-4943.
- [20] J. Andanson, A. Baiker, *Chem. Soc. Rev.* **2010**, *39*, 4571-4584.
- [21] A. M. Beale, S. D. Jacques, B. M. Weckhuysen, *Chem. Soc. Rev.* **2010**, *39*, 4656-4672.
- [22] G. De Cremer, B. F. Sels, D. E. De Vos, J. Hofkens, M. B. J. Roeffaers, *Chem. Soc. Rev.* **2010**, *39*, 4703-4717.

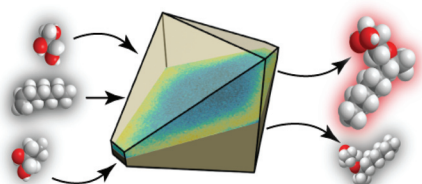
- [23] E. Stavitski, B. M. Weckhuysen, *Chem. Soc. Rev.* **2010**, *39*, 4615-4625.
- [24] H. Topsøe, *J. Catal.* **2003**, *216*, 155-164.
- [25] M. H. F. Kox, E. Stavitski, B. M. Weckhuysen, *Angew. Chem. Int. Ed.* **2007**, *46*, 3652-3655.
- [26] M. H. F. Kox, E. Stavitski, J. C. Groen, J. Perez-Ramirez, F. Kapteijn, B. M. Weckhuysen, *Chem. Eur. J.* **2008**, *14*, 1718-1725.
- [27] M. H. F. Kox, A. Mijovilovich, J. J. H. B. Sattler, E. Stavitski, B. M. Weckhuysen, *ChemCatChem.* **2010**, *2*, 564-571.
- [28] L. Karwacki, E. Stavitski, M. H. F. Kox, J. Kornatowski, B. M. Weckhuysen, *Angew. Chem. Int. Ed.* **2007**, *46*, 7228-7231.
- [29] L. Karwacki, M. H. F. Kox, D. A. M. de Winter, M. R. Drury, J. D. Meeldijk, E. Stavitski, W. Schmidt, M. Mertens, P. Cubillas, N. John, A. Chan, N. Kahn, S. R. Bare, M. Anderson, J. Kornatowski, B. M. Weckhuysen, *Nature Mater.* **2009**, *8*, 959-965.
- [30] L. Karwacki, H. E. van der Bij, J. Kornatowski, P. Cubillas, M. R. Drury, D. A. M. de Winter, M. W. Anderson, B. M. Weckhuysen, *Angew. Chem. Int. Ed.* **2010**, *49*, 6790-6794.
- [31] A. N. Parvulescu, D. Mores, E. Stavitski, C. M. Teodorescu, P. C. A. Bruijninx, R. J. M. K. Gebbink, B. M. Weckhuysen, *J. Am. Chem. Soc.* **2010**, *132*, 10429-10439.
- [32] E. Stavitski, M. H. F. Kox, B. M. Weckhuysen, *Chem. Eur. J.* **2007**, *13*, 7057-7065.
- [33] E. Stavitski, M. H. F. Kox, I. Swart, F. M. F. de Groot, B. M. Weckhuysen, *Angew. Chem. Int. Ed.* **2008**, *47*, 3543-3547.
- [34] L. Karwacki, B. M. Weckhuysen, *Phys. Chem. Chem. Phys.* **2011**, *13*, 3681-3685.
- [35] G. Spoto, F. Geobaldo, S. Bordiga, C. Lamberti, D. Scarano, A. Zecchina, *Top. Catal.* **1999**, *8*, 279-292.
- [36] O. C. Gobin, S. J. Reitmeier, A. Jentys, J. A. Lercher, *J. Phys. Chem. C* **2009**, *113*, 20435-20444.
- [37] D. Mores, E. Stavitski, M. H. F. Kox, J. Kornatowski, U. Olsbye, B. M. Weckhuysen, *Chem. Eur. J.* **2008**, *14*, 11320-11327.
- [38] D. Mores, J. Kornatowski, U. Olsbye, B. M. Weckhuysen, *Chem. Eur. J.* **2011**, *17*, 2874-2884.
- [39] M. Stöcker, *Microporous Mesoporous Mater.* **1999**, *29*, 3-48.
- [40] Y. Nagamori, M. Kawase, *Microporous Mesoporous Mater.* **1998**, *21*, 439-445.
- [41] M. Bjorgen, S. Akyalcin, U. Olsbye, S. Benard, S. Kolboe, S. Svelle, *J. Catal.* **2010**, *275*, 170-180.
- [42] P. L. Benito, A. G. Gayubo, A. T. Aguayo, M. Olazar, J. Bilbao, *Ind. Eng. Chem. Res.* **1996**, *35*, 3991-3998.
- [43] H. Schulz, *Catal. Today* **2010**, *154*, 183-194.
- [44] P. L. Benito, A. G. Gayubo, A. T. Aguayo, M. Olazar, J. Bilbao, *J. Chem. Technol. Biotechnol.* **1996**, *66*, 183-191.
- [45] D. M. Bibby, R. F. Howe, G. D. Mclellan, *Appl. Catal. A* **1992**, *93*, 1-34.
- [46] M. Bjorgen, U. Olsbye, S. Kolboe, *J. Catal.* **2003**, *215*, 30-44.
- [47] G. F. Froment, J. Demeyer, E. G. Derouane, *J. Catal.* **1990**, *124*, 391-400.

- [48] J. F. Haw, D. M. Marcus, *Top. Catal.* **2005**, *34*, 41-48.
- [49] K. Hemelsoet, A. Nollet, M. Vandichel, D. Lesthaeghe, V. Van Speybroeck, M. Waroquier, *ChemCatChem.* **2009**, *1*, 373-378.
- [50] B. P. C. Hereijgers, F. Bleken, M. H. Nilsen, S. Svelle, K. P. Lillerud, M. Bjorgen, B. M. Weckhuysen, U. Olsbye, *J. Catal.* **2009**, *264*, 77-87.
- [51] I. Kiricsi, H. Forster, G. Tasi, J. B. Nagy, *Chem. Rev.* **1999**, *99*, 2085-2114.
- [52] M. Bjorgen, F. Bonino, S. Kolboe, K. P. Lillerud, A. Zecchina, S. Bordiga, *J. Am. Chem. Soc.* **2003**, *125*, 15863-15868.
- [53] M. Bjorgen, F. Joensen, K. P. Lillerud, U. Olsbye, S. Svelle, *Catal. Today* **2009**, *142*, 90-97.
- [54] U. Olsbye, M. Bjorgen, S. Svelle, K. P. Lillerud, S. Kolboe, *Catal. Today* **2005**, *106*, 108-111.
- [55] A. Sassi, M. A. Wildman, H. J. Ahn, P. Prasad, J. B. Nicholas, J. F. Haw, *J. Phys. Chem. B* **2002**, *106*, 2294-2303.
- [56] S. Svelle, M. Bjorgen, S. Kolboe, D. Kuck, M. Letzel, U. Olsbye, O. Sekiguchi, E. Uggerud, *Catal. Lett.* **2006**, *109*, 25-35.
- [57] S. Svelle, F. Joensen, J. Nerlov, U. Olsbye, K. P. Lillerud, S. Kolboe, M. Bjorgen, *J. Am. Chem. Soc.* **2006**, *128*, 14770-14771.
- [58] S. Svelle, U. Olsbye, K. P. Lillerud, S. Kolboe, M. Bjorgen, *J. Am. Chem. Soc.* **2006**, *128*, 5618-5619.
- [59] Y. Q. Song, X. X. Zhu, L. Y. Xu, *Catal. Comm.* **2006**, *7*, 218-223.
- [60] C. Paze, B. Sazak, A. Zecchina, J. Dwyer, *J. Phys. Chem. B* **1999**, *103*, 9978-9986.
- [61] L. Palumbo, F. Bonino, P. Beato, M. Bjorgen, A. Zecchina, S. Bordiga, *J. Phys. Chem. C* **2008**, *112*, 9710-9716.
- [62] Y-M Chung, D. Mores, B.M. Weckhuysen, *Appl. Catal. A* **2011**, in press (doi:10.1016/j.apcata.2011.06030).

Chapter 7

Etherification of Biomass-Based Polyols with Alkenes over H-Beta Zeolites

Spatial and Temporal Mapping of Coke within Individual Zeolite Catalysts



Confocal fluorescence microscopy imaging illustrates the substrate interaction and the coke distribution caused by the etherification of biomass-based polyols with long α -olefins. Physicochemical properties of the reactants affect the formation of undesired compounds as visualized on individual H-Beta zeolite crystals.

7.1 Introduction

Catalyst deactivation caused by coke deposition is an important topic in heterogeneous catalysis and for zeolites in particular.^[1, 2] The formation of these heavy by-products is associated with side reactions that occur during the catalytic reaction. These compounds can cover catalytic active sites or block the zeolite pore network. As a consequence, loss of activity and selectivity invariably imply the loss of valuable organic substrates and costly catalyst regeneration. Understanding the coke formation mechanisms is therefore important, as the identification of the steps that control the deactivation of the catalyst can provide solutions that avoid coke generation.^[3-12]

Nowadays, the pursuit for oil-alternative feedstocks directs towards the use of coal, natural gas or biomass.^[13-16] The direct conversion of biomass in particular implies a marked change in the chemical nature of the feedstock. Petroleum-based feeds contain little functionalities, while the biomass-based feedstocks are rich in functionalities and the transition may therefore give rise to new challenges in the development of stable catalysts. Furthermore, as biomass-derived conversions generally take place in the liquid phase at relatively low reaction temperatures, these rather unusual reaction conditions can additionally influence the coke formation processes.^[17-19]

H-Beta is a promising zeolite catalyst for the conversion of biomass-based alcohols. This molecular sieve proved, for instance, to be an adequate catalyst for the etherification of glycols with long linear alkenes.^[20-25] Figure 7.1 illustrates as an example the etherification of 1,2-propylene glycol (1,2PG) with 1-octene. This particular conversion yielded, under solvent-free conditions, more than 90 % selectivity for the *mono*- (C8) and the *di*-ether (C16).

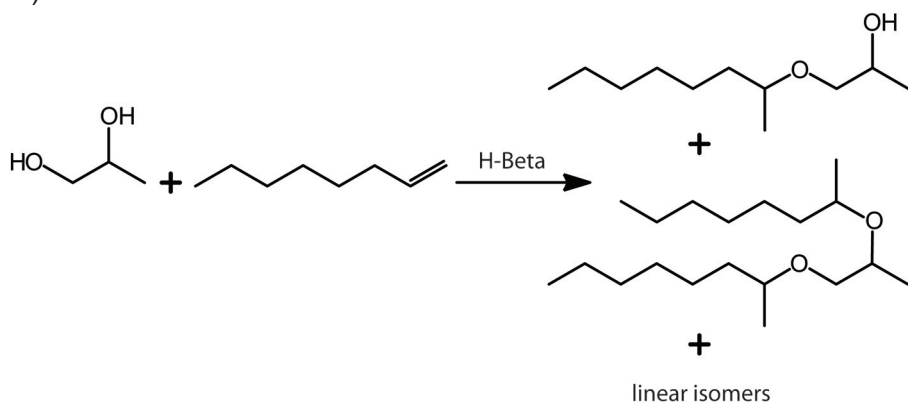


Figure 7.1: Schematic illustration of the etherification of 1,2-propylene glycol (1,2PG) with 1-octene over H-Beta zeolite.

Various substrates can provide promising product selectivity. However, the specific influence of the polyol substrate on the conversion is noted. Glycols and alcohols, for instance, provide more than 50% conversion yield, whereas catalyst deactivation is more severe with glycerol reactants, yielding a maximum of 20% under optimized reaction conditions. In addition, the use of different alkenes generates significant variations in both conversion activity as well as product selectivity. This outcome is indicative for the influence of the hydrophilic-hydrophobic relationship between the substrates and characteristic for liquid phase reactions that involve both a polar and an apolar phase. Understanding the actions that take place during these processes is essential for their further progress and micro-spectroscopic techniques can thereby be of assistance. These analytical methods allow following the events that take place at the individual catalyst particle level and provide information in a time- and space-resolved manner, thereby offering details on the distribution and diffusion of reactant species.^[26-37] In this work, we apply micro-spectroscopic tools to evaluate the etherification of alcohols with long-chain linear alkenes, under solvent-free conditions. The examination of individual alcohols and alkenes as well as reaction mixtures thereof, is performed to investigate substrate reactivity and the propensity towards coke formation. This enables to further understand the etherification processes that take place at one zeolite particle and to localize the formation as well as the source of the deactivating species.

7.2 Experimental

7.2.1 Materials

Large zeolite Beta crystallites were synthesized according to the method of Sano et al.^[38] For the synthesis of Beta (Si/Al ratio of 45), 2.40 g of silica (Sipernat 50, Evonik Degussa), 0.078 g of Al(OH)₃ (0.079) (> 63.5 % Al₂O₃, Acros), and 0.592 g of NH₄F (> 98%, Sigma-Aldrich) were added to 7.57 g of tetraethylammonium hydroxide solution (TEAOH, 35 wt%, Sigma-Aldrich), which resulted in a gel with a molar composition of 1.0 SiO₂: 0.0125 Al₂O₃: 0.225 TEAOH: 0.4 NH₄F: 7.14 H₂O. The mixture was stirred at room temperature for 1 h and then transferred into a Teflon-lined steel autoclave with a full capacity volume of 50 ml (inner diameter of the Teflon bottle is 34 mm and 55 mm high). The autoclave was placed in a preheated oven at 445 K for 7 days, and afterwards quenched with tap water. The precipitated product was triply washed with hot water (340 ~ 350 K) and consecutive filtration, provided the microcrystalline product, which was additionally dried

overnight at 330 K and calcined before testing. Glycerol (> 99 %, Acros), 1,2-propylene glycol (> 99 %, Acros), 1,3-propylene glycol (> 99 %, Fluka), ethylene glycol (> 99 %, Fluka), 1-octene (99 +%, Acros), 1-decene (99 +%, Acros) and 1-dodecene (99 +%, Acros) were used as received.

7.2.2 Methods

X-ray powder diffraction (XRD) was performed using a Bruker-AXS D8 Advance powder X-ray diffractometer, equipped with automatic divergence slit, Vântec-1 detector and Cobalt $K\alpha_{1,2}$ ($\lambda = 1.79026 \text{ \AA}$) source. Scanning Electron Microscopy (SEM) measurements were performed using a FEI XL30 FEG electron microscope equipped with an EDX detector. The results are illustrated in Figure 7.2.

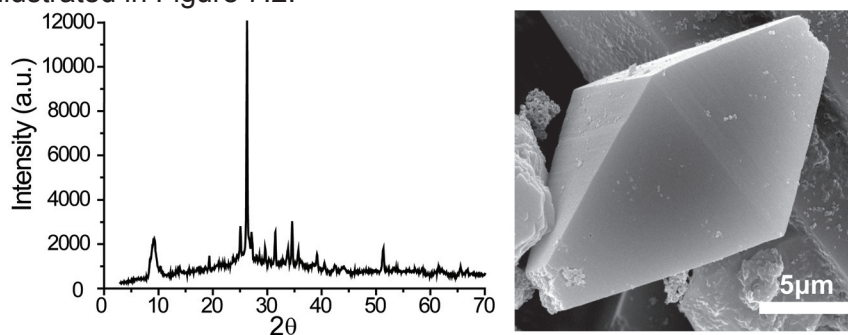


Figure 7.2: XRD pattern of the micron-sized H-Beta zeolite material (left) and a Scanning Electron Micrograph (SEM) picture of H-Beta zeolite.

Samples of the micron-sized H-Beta were taken from the reaction mixture at different reaction times, washed several times with solvents (ethanol and dichloromethane (DCM)) and separated by centrifugation. The resulting samples were dried under N_2 flow at room temperature for 1 h and analyzed. Confocal fluorescence microscopy measurements were performed on a Nikon Eclipse LV150 upright microscope with 50×0.55 NA dry objective. The confocal images were acquired with a Nikon D-Eclipse C1 head connected to the laser light sources (488 nm and 561 nm). The emission was detected in the ranges 510-550 and 575-635 nm, with PMT.

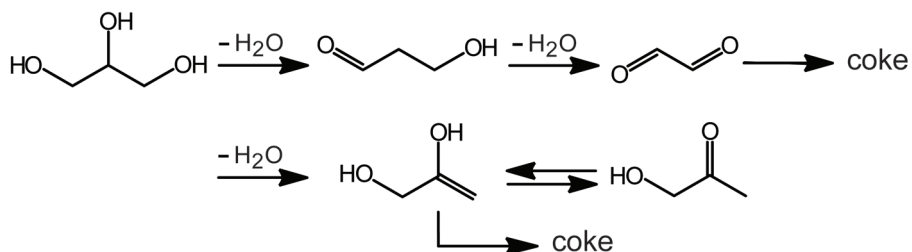
FT-IR measurements were performed on a Perkin-Elmer 2000 FTIR spectrometer. For this, a data point resolution of 4 cm^{-1} using a DTGS detector and an accumulation of 16 scans per spectrum was applied. The samples were diluted prior measurements with KBr in a 5/95 mixture ratio. Diffuse reflectance (DR)UV-Vis measurements were done on a Cary 500 UV-Vis-NIR instrument in the 250-800 nm region. The samples were diluted with MgO in a 20/80 mixture ratio.

7.3 Results and discussion

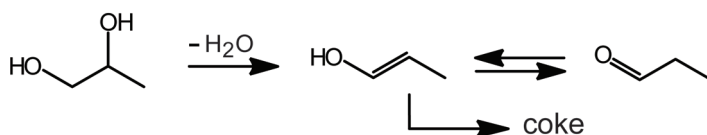
7.3.1 Deactivation during etherification

The etherification of biomass-based polyols with long linear alkenes is studied under solvent-free conditions over individual H-Beta zeolite of 9 μm size. After catalytic reaction, the recovered zeolite catalysts show a change in coloration that is ascribed to coke deposits retained within the crystals. Both the polyol and the alkene can direct to the formation of coke species. Alkene side reactions are known to lead towards higher molecular weight products that are difficult to remove from the solid acid catalysts. Dehydration of alcohols can on the other hand direct to the formation of highly reactive alkenes. These unsaturated intermediates can consequently polymerize and produce coke compounds.^[39-42] A schematic illustration of these processes is given in Figure 7.3.

glycerol dehydration



1,2-propylene glycol dehydrogenation



alkene

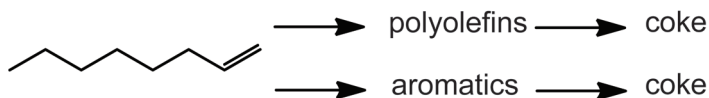


Figure 7.3: Schematic illustration on sources for coke formation during the etherification of biomass-based alcohols with long linear alkenes.

7.3.2 Influence of the alcohol reactants

In a first set of experiments, the interaction of the alcohol with the H-Beta zeolite is investigated. The absence of alkene reactant and the use of standard etherification reaction conditions i.e. reaction temperature of 413 K and argon pressure, cause the coloration of the zeolite crystals. Different alcohols have been examined. The corresponding catalytic crystals were taken out of the reaction mixture and analyzed with diffuse reflectance (DR)UV-Vis and FT-IR spectroscopy. The results of these measurements are shown in Figure 7.4.

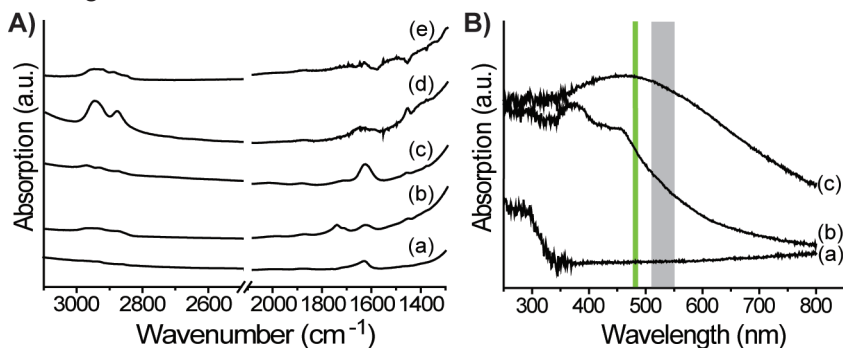


Figure 7.4: (A) FT-IR spectra of the H-Beta zeolite samples taken after 3 h of reaction at 413 K with: a) blank zeolite, b) glycerol, c) 1,2-propylene glycol, d) ethylene glycol and e) 1,3-propylene glycol. (B) (DR)UV-Vis spectra of the H-Beta zeolite samples taken after 3 h of reaction at 140 °C with: a) blank zeolite, b) 1,2-propylene glycol and c) glycerol. The green bar indicates the laser excitation wavelength located at 488 nm and the grey area represents the corresponding detection region at 510-550 nm.

Figure 7.4 points out how the color change during reaction of the alcohols with the zeolite is caused by the formation of carbonaceous species within the catalyst. For all glycols (Figure 7.4A (c-e)), the FT-IR spectra of the catalyst show vibrations at 2863, 2930 and 2958 cm⁻¹, which correspond to $\nu_s(\text{CH}_3)$, $\nu_{\text{as}}(\text{CH}_2)$ and $\nu_{\text{as}}(\text{CH}_3)$ vibrations, respectively.^[31, 43, 44] No bands above 3000 cm⁻¹, corresponding to aromatic (CH) bonds, are observed. The band at 1634 cm⁻¹, can principally originate from both water adsorbed on the zeolite as well as $\nu(\text{C}=\text{C})$ of coke compounds. Finally, the band at 1460 cm⁻¹ is assigned to (CH₃) asymmetrical bending. For glycerol (Figure 7.4A (b)), two additional bands, located at 1714 and 1749 cm⁻¹, are obtained and assigned to adsorbed oxygenated species, such as aldehydes.^[43, 45]

The UV-Vis measurements assist in further understanding the nature of these retained coke species. The 1,2-propylene glycol treated zeolite (Figure

7.4B (b)) provides two bands with absorption maxima at 370 and 460 nm. The band at 370 nm has been previously associated with polyenilic cations and therefore suggests the presence of soft poly-olefinic coke.^[44, 46-48] The band at 460 nm is attributed to unsaturated species with a higher degree of conjugation. The zeolite samples removed from the glycerol reaction mixture give a broad absorption band with maxima at 470 nm (Figure 7.4B (c)). This, combined with the more pronounced catalyst coloration, grounds to assign the observations to highly conjugated coke species.^[10, 49-53]

The UV-Vis and FT-IR measurements give initial insights on the nature of the coke compounds that are caused by the polyol side reactions. These tools are however unable to supply information at the individual particle level or to further differentiate between the different polyols. Throughout this PhD thesis it is reported that coke possesses fluorescent properties that allow mapping their spatial distribution within an individual catalyst particle.^[28-30, 54] H-Beta zeolite crystals exhibit minor fluorescence in the absence of any organic impurity. Therefore, monitoring fluorescent coke products formed in the etherification reaction permits to further understand the nature of the reactant's interaction with the zeolite and to determine their distribution at the individual particle level. The discussed zeolite samples have for that reason been analyzed with confocal fluorescence microscopy.

Figure 7.5 illustrates the confocal fluorescence intensity maps of the middle plane of the bipyramidal H-Beta zeolites after reaction. The measurements are taken using the 488 nm laser excitation wavelength, which based on the UV-Vis absorption, displayed in Figure 7.4B, ensures excitation of the formed coke species. With increasing reaction time, a raise in fluorescence intensity suggests a progressing formation of coke species. More importantly, a strong relation between the polyol-reactant type and the distribution of fluorescent species is observed. These species are strongly attached to the zeolite crystal as vigorous washing, performed before the fluorescence measurements, did not remove them.

In the case of glycerol (Figure 7.5a), the most polar of the alcohols studied, the fluorescent coke species predominantly concentrate at the center of the zeolite crystal and compared to other glycols, a higher fluorescence intensity is obtained. The distribution of the fluorescent species originating from the glycols varies between the separate polyols.

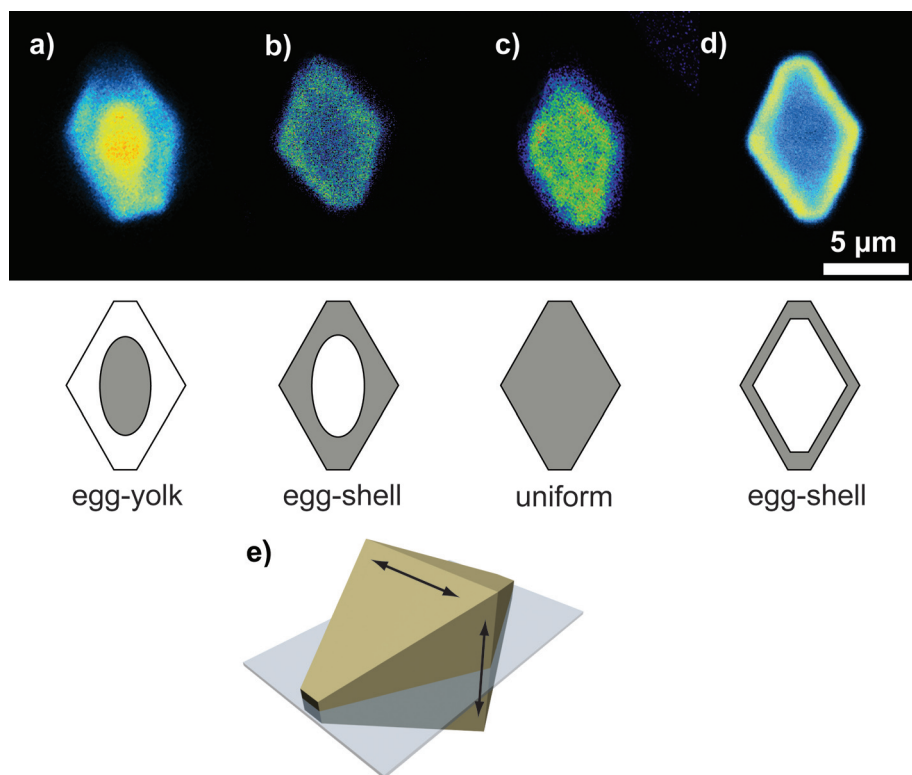


Figure 7.5: Confocal fluorescence microscopy images of individual H-Beta zeolite crystals recorded after 3 h of reaction at 413 K with: (a) glycerol; (b) ethylene glycol; (c) 1,3-propylene glycol and (d) 1,2-propylene glycol. The measurements are performed using a 488 nm laser excitation wavelength (detection at 510-550 nm). The images are displayed in false color (intensity mode). The schematic representation of the slice at which the confocal fluorescence measurements have been performed is illustrated in (e), with the arrows indicating the direction of the catalyst pores.

Ethylene glycol (EG) provides mild fluorescent coke products that are mainly concentrated at the surface area of the crystal (Figure 7.5b). A similar concentration profile is obtained with 1,2-propylene glycol (1,2-PG). Here, the fluorescence is more pronounced and located near the external surface of the zeolite, while almost no fluorescence is observed in the center of the crystal (Figure 7.5d). The isomeric 1,3-propylene glycol (1,3-PG), on the other hand, forms fluorescent species that rather uniformly distribute over the entire zeolite crystal (Figure 7.5c). The obtained spatial distribution profiles are schematically depicted in Figure 7.5. These illustrations strongly resemble the well-known metal ion solid support impregnation distributions hence inviting the assignment of common ‘egg-yolk’, ‘egg-shell’ and ‘uniform’

classification.^[55-58] Following this analogy, coke formation from glycerol resembles an egg-yolk distribution, whereas EG and 1,2PG produce an egg-shell distribution. Most importantly, this distribution indicates a different adsorption of the alcohol in the zeolite crystal. The more hydrophilic alcohol, i.e. glycerol, seems able to enter the interior of the zeolite and transforms there into coke-like products. Less hydrophilic glycols, like EG and 1,2PG, remain more concentrated on the external catalyst surface. XPS measurements indicated that the H-Beta zeolite crystal has a higher Al concentration on its external surface (Si/Al of 12) as compared to the bulk composition (Si/Al of 45). For that reason, besides a higher number of Brønsted acid sites, the external surface is regarded more hydrophilic. Under these conditions, the hydrophilic properties of the zeolite catalyst correlate with those of the examined alcohols and explain the observed activity trend.

7.3.3 Influence of the alkene reactants

A second set of experiments, similar to those described in section 7.3.2, investigates the interaction between alkene reactants and the H-Beta zeolite. In this work, linear C6-to-C12 α -olefins are used to study the effect of the reactant chain length on the zeolite deactivation. The FT-IR and (DR)UV-Vis spectra of the recovered zeolite samples are presented in Figure 7.6.

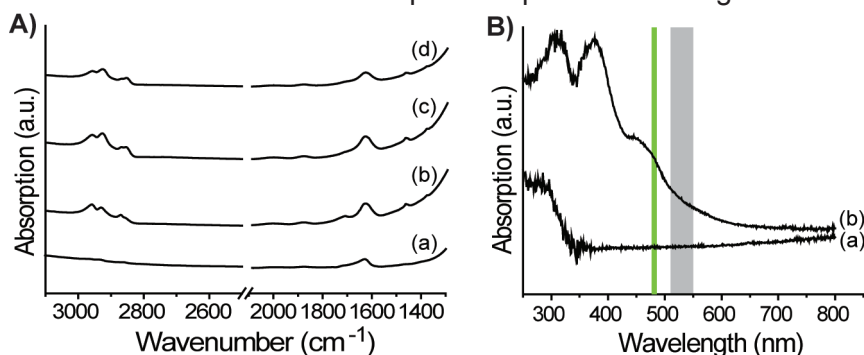


Figure 7.6: (A) FT-IR spectra of the H-Beta zeolite samples taken after 3 h of reaction at 413 K with: a) blank zeolite, b) 1-hexene, c) 1-octene and d) 1-dodecene. (B) (DR) UV-Vis spectra of the H-Beta zeolite sample taken after 3 h of reaction at 413 K with: a) blank zeolite and b) with 1-octene. The green bar indicates the laser excitation wavelength at 488 nm and the grey area is the corresponding detection region at 510-550 nm.

The alkene chain length slightly affects the position and the intensity ratio of the IR bands located in the CH stretching region. The 1-hexene treated sample (Figure 7.6A (b)) provides $\nu_{\text{as}}(\text{CH}_3)$ vibration band at 2965 cm⁻¹ that is more intense compared to its $\nu_{\text{as}}(\text{CH}_2)$ band located at 2930 cm⁻¹. On the other

hand, 1-octene and 1-dodecene treated samples cause the opposite and the $\nu_{\text{as}}(\text{CH}_2)$ band at 2930 cm^{-1} is more intense compared to the $\nu_{\text{as}}(\text{CH}_3)$ band. This observation is directly correlated to the longer alkyl chain. Increasing alkene molecular size furthermore introduces a new band that evolves at 2859 cm^{-1} and is assigned to asymmetric (CH_3) group vibration.^[44, 49, 59] Additional bands, attributed to the presence of adsorbed alkyl species, appear at 1460 and 1370 cm^{-1} , while the 1640 cm^{-1} band is associated to adsorbed water. Additional information on the type of species that form during the reaction of the alkene with the zeolite catalyst is provided by UV-Vis. Figure 7.6B shows the UV-Vis spectra of the 1-octene treated H-Beta zeolite. Here, three bands located at 307 , 375 and 460 nm are observed and associated with polyolefin coke type formation.^[1]

The interaction of the alkenes with the acid catalyst is mapped with confocal fluorescence microscopy likewise the previously discussed alcohol interaction with the zeolite. The results are shown in Figure 7.7.

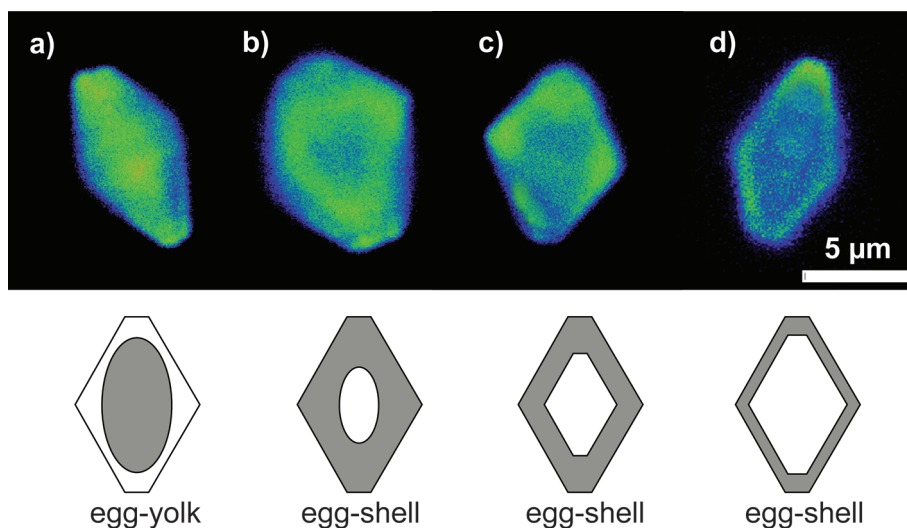


Figure 7.7: Confocal fluorescence microscopy images of individual H-Beta zeolite crystals recorded after 3 h of reaction at 413 K with: (a) 1-hexene; (b) 1-octene; (c) 1-decene and (d) 1-dodecene. The measurements are performed using a 488 nm laser excitation wavelength (detection at $510\text{--}550\text{ nm}$). The images are displayed in false color (intensity mode). The confocal fluorescence images were taken from the middle plane of the zeolite crystal as illustrated in Figure 7.5e.

As in the case of alcohol-reactants, different alkene substrates cause different fluorescent coke distribution profiles. For 1-octene, 1-decene and 1-dodecene, the fluorescence is more pronounced at the surface area of the zeolite as

illustrated by the egg-shell distributions (Figure 7.7b-d). Both hydrophobic properties and possible steric constraints can influence the alkene interaction with the zeolite. As a result, when going from the C8 to C12 alkenes, an increasing reactant chain length causes the retained material to be more concentrated near the external surface of the zeolite crystal. Once in acidic medium, these reactants can undergo oligomerization or other reactions that lead to the formation of carbonaceous products. These can slowly diffuse through the H-Beta crystallographic network and block the zeolite pores thereby explaining the minor fluorescence detected inside the zeolite crystal.^[60-63] The obtained profiles show that the smaller the alkene, the further it can diffuse into the zeolite, resulting in shells of increasing thickness from C12 to C8. Further exemplification is provided by 1-hexene, a smaller and more hydrophilic alkene. This reactant readily enters the H-Beta zeolite pores causing intense fluorescence that is detected in the center of the crystal.

7.3.4 Etherification in H-Beta zeolite

With this knowledge, the successive step is to combine the two reactants. Consequently, the etherification process was investigated using confocal fluorescence microscopy on individual H-Beta zeolites. The rather polyolefinic nature of the coke species is again confirmed by the FT-IR and the UV-Vis spectra and the results obtained for the etherification of glycerol and 1,2PG with 1-octene are illustrated in Figure 7.8.

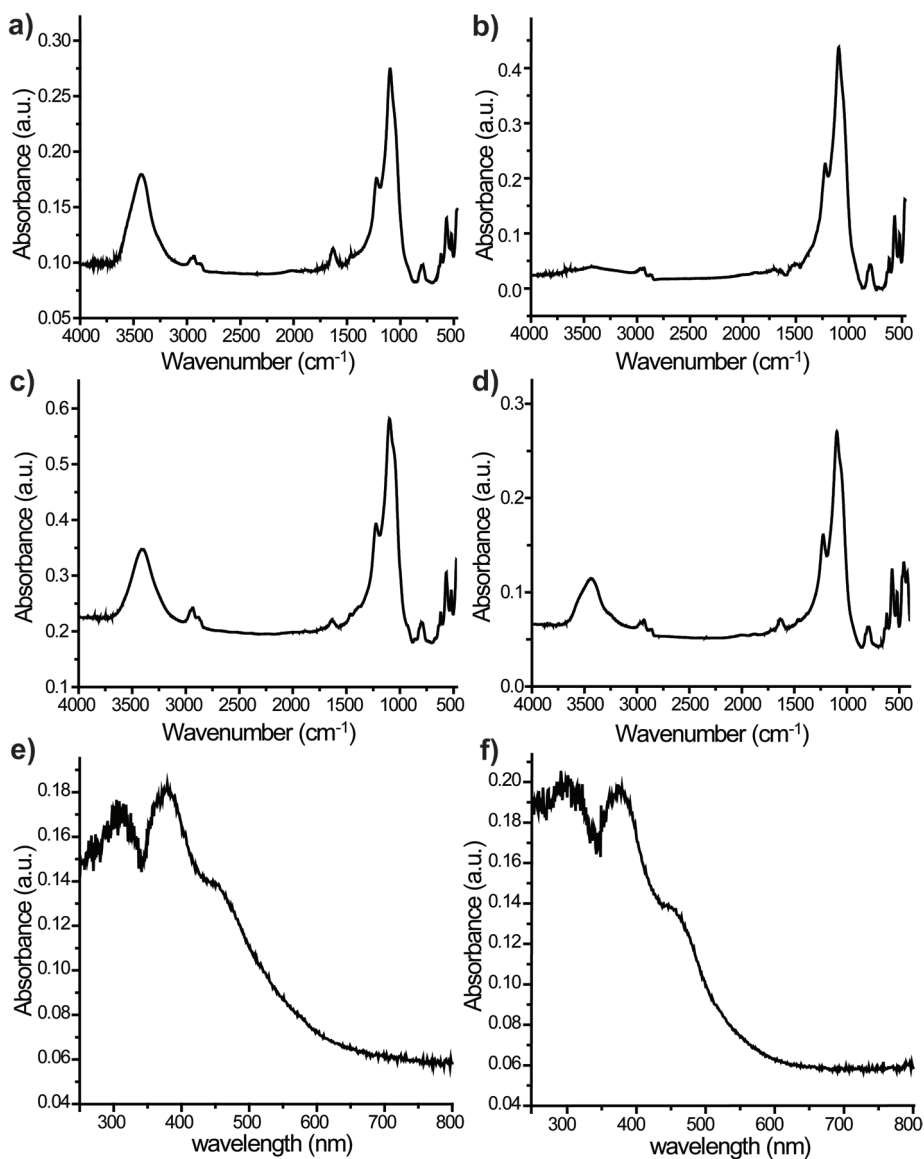


Figure 7.8: FT-IR spectra of the H-Beta zeolite recovered after etherification of (a) glycerol with 1-octene (30 min); (b) 1,2-propylene glycol with 1-octene (1 h); (c) glycerol with 1-octene (5 h) and (d) 1,2-propylene glycol with 1-octene (3 h). The corresponding (DR)UV-Vis spectra of the spent H-Beta catalysts recovered after etherification are shown for (e) glycerol with 1-octene (3h) and (f) 1,2-propylene glycol with 1-octene (3h).

Figure 7.9 shows, as a showcase, the results obtained for the conversion of glycerol with 1-octene. During the etherification of glycerol with 1-octene, the detection of fluorescent coke species occurs within 30 min of reaction. These compounds are moreover homogeneously distributed throughout the zeolite crystal being present both in the centre and on the edges of the catalyst grain.

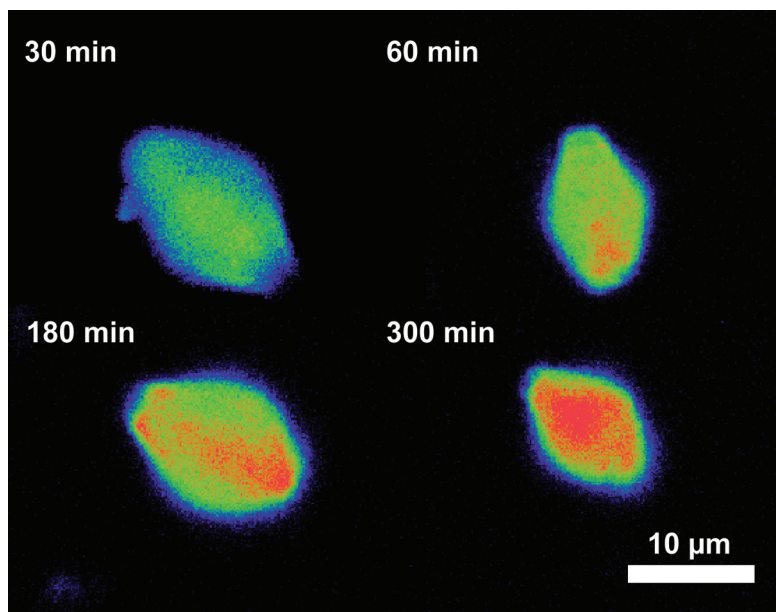


Figure 7.9: Confocal fluorescence images of individual H-Beta zeolite crystal during the etherification of glycerol with 1-octene at 413 K as a function of time: (a) 30 min; (b) 60 min; (c) 180 min and (d) 300 min. The images are displayed in false color (intensity profile). The measurements are performed using a 488 nm laser excitation wavelength (detection at 510-550 nm). The confocal fluorescence images were taken from the middle plane of the zeolite crystal as illustrated in Figure 7.5e.

Based on the previous results obtained for the glycerol interaction with the H-Beta zeolite, it is reasonable to assign the fluorescence at the zeolite center to glycerol-derived by-products. Figure 7.9 demonstrates how the fluorescence intensity increases with reaction time thereby following the edges of the truncated bipyramidal zeolite. These H-Beta crystals contain a pore orientation that is perpendicular to the edge of the crystal (Figure 7.5e).^[64] The growth of fluorescent species at the crystal edge in this direction is therefore likely caused by 1-octene. This alkene can easily enter the short length pores that are present on the edge of H-Beta crystal and block them, a process that can be associated with a pore-mouth mechanism. The confocal

fluorescence data evidences how after 5h of reaction, the entire zeolite crystal is covered with coke and illustrate how the rapid and extensive coke formation cause the low conversion activity and severe catalysts deactivation previously reported for the etherification of glycerol with 1-octene.^[22, 23, 39, 40]

1,2PG proved to be a much better substrate for etherification and indeed provides a different fluorescence profile. This is illustrated in Figure 7.10. The distribution of fluorescent coke-like species in this etherification reaction followed the same trend as their individual reactants and an overall egg-shell distribution was subsequently obtained (Figures 7.5 and 7.7).

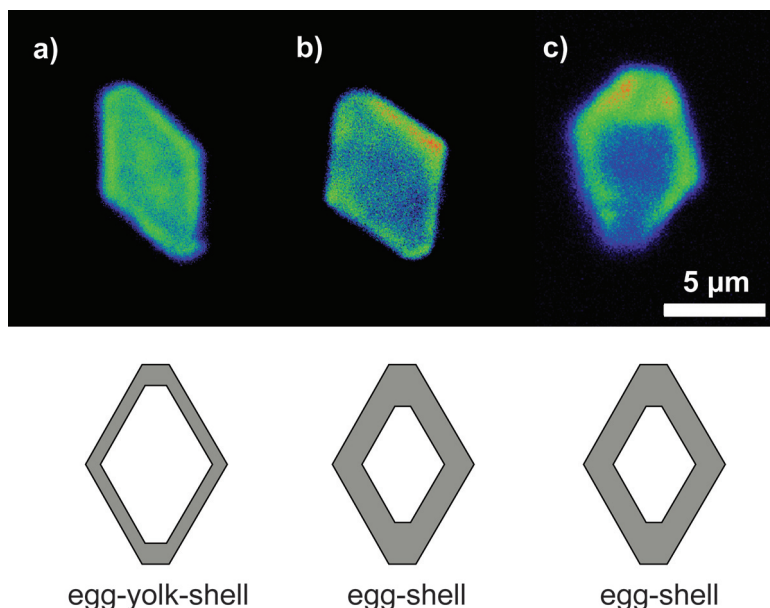


Figure 7.10: Confocal fluorescence microscopy images of individual H-Beta zeolite crystal taken after 3h of etherification at 413 K of (a) glycerol with 1-octene; (b) 1,2-propylene glycol with 1-octene and (c) 1,2-propylene glycol with 1-dodecene. The images are displayed in false color (intensity profile). The measurements are performed using a 488 nm laser excitation wavelength (detection at 510-550 nm). The confocal fluorescence images were taken from the middle plane of the zeolite crystal as illustrated in Figure 7.5e

The fluorescent species are mainly detected at the catalyst surface and no fluorescence is observed in the center of the zeolite particle. Both the alcohol and alkene thus adsorb preferentially on the external surface of the zeolite. The enhanced ether formation at the zeolite near-surface area consequently facilitates its desorption as the reactants may act as solvents as well. This

micro-spectroscopic data therefore indicates why higher conversions are obtained for 1,2PG etherification and why the deactivation of the zeolite is reduced. The fluorescence intensity is more pronounced after etherification of 1,2PG with 1-dodecene. Given the steric constraints of 1-dodecene compared to 1-octene, diffusion through the pores of the H-Beta zeolite crystal is more difficult for the larger substrate. In case pore blockage occurs close to the pore mouth area, the adsorption of other reactant molecules will be inhibited by the long alkyl tail of the alkene.

7.4 Conclusions

Bulk spectroscopic techniques and confocal fluorescence microscopy are used to investigate the coke formation on large micron-sized H-Beta zeolite crystals during the etherification of biomass-based alcohols with long linear alkenes under solvent-free conditions. The application of confocal fluorescence microscopy proved useful and indicated, in a space-resolved manner, that the physicochemical properties of the separate reactants (i.e. alcohol and alkene) have a strong influence on the formation of coke products in the zeolite crystal.

The hydrophobic/hydrophilic properties of both the reactants and the zeolite affect the nature and location of the undesired compounds. An external surface area, containing a high concentration of framework aluminum, was found to be essential. This area is more hydrophilic compared to the centre of the H-Beta zeolite. Hydrophobic reactants, such as glycols (particularly 1,2-propylene glycol) and long alkenes (such as 1-octene and 1-dodecene), therefore have difficulty to penetrate towards the crystal core and interact in the surface area of the zeolite crystal. As a result of this close contact, a facilitated transformation into reaction products and corresponding desorption occurs. The hydrophilic glycerol, on the other hand, reacts on the active sites located within the center of the zeolite crystal. As the long alkenes preferentially locate at the zeolite surface region, their etherification is constrained. The use of shorter alkenes, such as 1-hexene, which interacts with the H-Beta zeolite in a similar mode as glycerol, improves the conversion.

The etherification reaction studied here can be seen as an example typical for a biomass conversion process in the liquid phase, where the physicochemical properties of the reactants strongly influence the activity and stability of the heterogeneous catalyst.

Acknowledgements

Dr. A. Parvulescu is thanked for synthesizing the H-Beta zeolite material and performing the etherification reactions. Dr. E. Stavitski and Dr. P. Bruijninx are thanked for their contribution to this work and fruitful discussions.

References

- [1] H. van Bekkum, E.M. Flanigen, P.A. Jacobs, J.C. Jansen (Eds.), *Introduction to Zeolite Science and Practice*, Elsevier, Amsterdam, **2001**.
- [2] R.A. van Santen, P.W.N.M. van Leeuwen, J.A. Moulijn, B.A. Averil (Eds.), *Catalysis an Integrated Approach*, Elsevier, Amsterdam, **2000**.
- [3] H. Schulz, *Catal. Today* **2010**, *154*, 183-194.
- [4] P. L. Benito, A. G. Gayubo, A. T. Aguayo, M. Olazar, J. Bilbao, *Ind. Eng. Chem. Res.* **1996**, *35*, 3991-3998.
- [5] S. Bhatia, J. Beltramini, D. D. Do, *Catal. Rev. Sci. Eng.* **1989**, *31*, 431-480.
- [6] D. M. Bibby, R. F. Howe, G. D. McLellan, *Appl. Catal. A* **1992**, *93*, 1-34.
- [7] G. F. Froment, J. Demeyer, E. G. Derouane, *J. Catal.* **1990**, *124*, 391-400.
- [8] G. F. Froment, *Cat. Rev. Sci. Eng.* **2008**, *50*, 1-18.
- [9] M. Guisnet, L. Costa, F. R. Ribeiro, *J. Mol. Catal. A* **2009**, *305*, 69-83.
- [10] M. Guisnet, P. Magnoux, *Appl. Catal. A* **2001**, *212*, 83-96.
- [11] M. Guisnet, P. Magnoux, *Appl. Catal.* **1989**, *54*, 1-27.
- [12] J. M. Lopes, F. Lemos, F. R. Ribeiro, E. G. Derouane, P. Magnoux, M. Guisnet, *Appl. Catal. A* **1994**, *114*, 161-172.
- [13] J. L. G. Fierro, *Catal. Lett.* **1993**, *22*, 67-91.
- [14] O. L. Eliseev, *Russian J. Gen. Chem.* **2009**, *79*, 2509-2519.
- [15] C. Okkerse, H. van Bekkum, *Green Chem.* **1999**, *1*, 107-114.
- [16] G. A. Olah, *Angew. Chem. Int. Ed.* **2005**, *44*, 2636-2639.
- [17] J. N. Chheda, G. W. Huber, J. Dumesic, *Angew. Chem. Int. Ed.* **2007**, *46*, 7164-7183.
- [18] J. N. Chheda, J. A. Dumesic, *Catal. Today* **2007**, *123*, 59-70.
- [19] J. N. Chheda, Y. Roman-Leshkov, J. A. Dumesic, *Green Chem.* **2007**, *9*, 342-350.
- [20] T. P. Vispute, H. Y. Zhang, A. Sanna, R. Xiao, G. W. Huber, *Science* **2010**, *330*, 1222-1227.
- [21] A. M. Ruppert, A. N. Parvulescu, M. Arias, P. J. C. Hausoul, P. C. A. Bruijninx, R. J. M. K. Gebbink, B. M. Weckhuysen, *J. Catal.* **2009**, *268*, 251-259.
- [22] A. N. Parvulescu, P. J. C. Hausoul, P. C. A. Bruijninx, R. J. M. K. Gebbink, B. M. Weckhuysen, *Catal. Today* **2010**, *158*, 130-138.
- [23] R. Palkovits, K. Tajvidi, A. M. Ruppert, J. Procelewska, *Chem. Com.* **2011**, *47*, 576-578.
- [24] Y. G. Zheng, X. L. Chen, Y. C. Shen, *Chem. Rev.* **2008**, *108*, 5253-5277.
- [25] W. Suprun, M. Lutecki, T. Haber, H. Papp, *J. Mol. Catal. A* **2009**, *309*, 71-78.
- [26] B.M. Weckhuysen (Ed.), *In-Situ Spectroscopy of Catalysts*, American Scientific Publishers, Stevenson Ranch, **2004**.

- [27] B. M. Weckhuysen, *Angew. Chem. Int. Ed.* **2009**, *48*, 4910-4943.
- [28] D. Mores, E. Stavitski, M. H. F. Kox, J. Kornatowski, U. Olsbye, B. M. Weckhuysen, *Chem. Eur. J.* **2008**, *14*, 11320-11327.
- [29] D. Mores, J. Kornatowski, U. Olsbye, B.M. Weckhuysen, *Chem. Eur. J.* **2011**, *17*, 2874-2884.
- [30] E. Stavitski, M. H. F. Kox, B. M. Weckhuysen, *Chem. Eur. J.* **2007**, *13*, 7057-7065.
- [31] E. Stavitski, B. M. Weckhuysen, *Chem. Soc. Rev.* **2010**, *39*, 4615-4625.
- [32] L. Sommer, D. Mores, S. Svelle, M. Stöcker, B. M. Weckhuysen, U. Olsbye, *Microporous Mesoporous Mater.* **2010**, *132*, 384-394.
- [33] M. H. F. Kox, E. Stavitski, B. M. Weckhuysen, *Angew. Chem. Int. Ed.* **2007**, *46*, 3652-3655.
- [34] M. H. F. Kox, A. Mijovilovich, J. J. H. B. Sattler, E. Stavitski, B. M. Weckhuysen, *ChemCatChem.* **2010**, *2*, 564-571.
- [35] L. Karwacki, B. M. Weckhuysen, *Phys. Chem. Chem. Phys.* **2011**, *13*, 3681-3685.
- [36] L. Karwacki, H. E. van der Bij, J. Kornatowski, P. Cubillas, M. R. Drury, D. A. M. de Winter, M. W. Anderson, B. M. Weckhuysen, *Angew. Chem. Int. Ed.* **2010**, *49*, 6790-6794.
- [37] J.W. Niemantsverdriet (Ed.), *Spectroscopy in Catalysis: An Introduction*, VCH, Weinheim, **2007**.
- [38] B. W. Lu, H. Jon, T. Kanai, Y. Oumi, K. Itabashi, T. Sano, *J. Mater. Sci.* **2006**, *41*, 1861-1864.
- [39] S. Pariente, N. Tanchoux, F. Fajula, *Green Chem.* **2009**, *11*, 1256-1261.
- [40] A. Parvulescu, M. Rossi, C. Della Pina, R. Ciriminna, M. Pagliaro, *Green Chem.* **2011**, *13*, 143-148.
- [41] M. Pagliaro, R. Ciriminna, H. Kimura, M. Rossi, C. Della Pina, *Angew. Chem. Int. Ed.* **2007**, *46*, 4434-4440.
- [42] A. Corma, G. W. Huber, L. Sauvanauda, P. O'Connor, *J. Catal.* **2008**, *257*, 163-171.
- [43] B. S. Williams, *Tetrahedron* **2002**, *58*, 2091-2094.
- [44] C. Paze, B. Sazak, A. Zecchina, J. Dwyer, *J. Phys. Chem. B* **1999**, *103*, 9978-9986.
- [45] L. Cheng, X. Philip Ze, *Catal. Lett.* **2009**, *130*, 100-107.
- [46] I. Kiricsi, G. Tasi, H. Forster, P. Fejes, *J. Mol. Struct.* **1990**, *218*, 369-374.
- [47] I. Kiricsi, H. Forster, G. Tasi, J. B. Nagy, *Chem. Rev.* **1999**, *99*, 2085-2114.
- [48] F. Geobaldo, G. Spoto, S. Bordiga, C. Lamberti, A. Zecchina, *J. Chem. Soc. Faraday Trans.* **1997**, *93*, 1243-1249.
- [49] M. Bjorgen, F. Bonino, S. Kolboe, K. P. Lillerud, A. Zecchina, S. Bordiga, *J. Am. Chem. Soc.* **2003**, *125*, 15863-15868.
- [50] M. Bjorgen, S. Akyalcin, U. Olsbye, S. Benard, S. Kolboe, S. Svelle, *J. Catal.* **2010**, *275*, 170-180.
- [51] H. Forster, J. Seebode, P. Fejes, I. Kiricsi, *J. Chem. Soc. Faraday Trans.* **1987**, *83*, 1109-1117.
- [52] M. Guisnet, N. S. Gnep, *Appl. Catal. A* **1996**, *146*, 33-64.
- [53] P. Magnoux, H. S. Cerqueira, M. Guisnet, *Appl. Catal. A* **2002**, *235*, 93-99.

- [54] L. Sommer, D. Mores, S. Svelle, M. Stocker, B. M. Weckhuysen, U. Olsbye, *Microporous Mesoporous Mater.* **2010**, *132*, 384-394.
- [55] J. A. Bergwerff, A. A. Lysova, L. Espinosa-Alonso, I. V. Koptuyug, B. M. Weckhuysen, *Chem. Eur. J.* **2008**, *14*, 2363-2374.
- [56] L. Espinosa-Alonso, A. A. Lysova, P. Peinder, K. P. de Jong, I. V. Koptuyug, B. M. Weckhuysen, *J. Am. Chem. Soc.* **2009**, *131*, 6525-6534.
- [57] L. Espinosa-Alonso, K. P. de Jong, B. M. Weckhuysen, *Phys. Chem. Chem. Phys.* **2010**, *12*, 97-107.
- [58] L. Espinosa-Alonso, A. M. Beale, B. M. Weckhuysen, *Acc. Chem. Res.* **2010**, *43*, 1279-1288.
- [59] L. Palumbo, F. Bonino, P. Beato, M. Bjorgen, A. Zecchina, S. Bordiga, *J. Phys. Chem. C* **2008**, *112*, 9710-9716.
- [60] A. Simon-Masseron, J. P. Marques, J. M. Lopes, F. R. Ribeiro, I. Gener, M. Guisnet, *Appl. Catal. A* **2007**, *316*, 75-82.
- [61] A. de Klerk, R. J. J. Nel, *Ind. Eng. Chem. Res.* **2007**, *46*, 7066-7072.
- [62] Z. Da, Z. Han, P. Magnoux, M. Guisnet, *Appl. Catal. A* **2001**, *219*, 45-52.
- [63] R. J. J. Nel, A. de Klerk, *Ind. Eng. Chem. Res.* **2007**, *46*, 2902-2906.
- [64] J. Sun, G. S. Zhu, Y. L. Chen, J. X. Li, L. F. Wang, Y. Peng, H. Li, S. L. Qiu, *Microporous Mesoporous Mater.* **2007**, *102*, 242-248.

Chapter 8a

Summary and Future Perspectives

In hydrocarbon processing, the formation of carbonaceous deposits is usually inevitable. These undesired by-products influence the performance of catalyst materials with possible consequences for their industrial application. The scope of this PhD thesis is to examine the coke formation processes in zeolite catalysts using in-situ micro-spectroscopic techniques. UV-Vis micro-spectroscopy and confocal fluorescence microscopy are hereby mainly employed and applied on large micron-sized zeolite crystals. With this approach, spatial heterogeneities in the coke growth processes can be observed, thereby revealing detailed insights in deactivation phenomena at the individual catalyst particle level.

In **Chapter 2**, two distinct micron-sized zeolite catalysts are used to unravel the influence of the zeolite framework topology on the coke formation process during the Methanol-to-Olefin (MTO) conversion. These two zeolite types are H-ZSM-5 and H-SAPO-34. In H-ZSM-5, the coke growth starts at the edges of the coffin-shaped crystal and homogeneously spreads throughout the entire zeolite. Time-resolved UV-Vis micro-spectroscopy illustrates how the reaction temperature strongly affects the formation of carbonaceous deposits. Mild reaction conditions cause a moderate crystal browning that largely consists of monoaromatic species. With increasing reaction temperature, the coke molecules form at a faster rate and the crystal darkening becomes more severe. These coke compounds grow towards larger conjugated systems with polyaromatic character and graphite-like species are located at the zeolite external surface. In H-SAPO-34 crystals, methylated monoaromatics are generated that mainly form at the near surface area of the crystal. Increasing reaction temperature results in a more pronounced coke growth. However, these larger carbonaceous deposits remain rather constrained in size and retained within the catalyst crystal. In-situ confocal fluorescence microscopy illustrates the migration of fluorescent coke species through the zeolite crystal. In H-ZSM-5, larger coke compounds experience higher diffusion limitations that are most distinct at the intra-crystalline subunit boundaries. In H-SAPO-34, the fluorescent by-products mainly locate near the crystal edge and larger coke species restrict the access towards the crystal core.

The influence of the Brønsted acid site density on the coke formation process during the MTO conversion is studied in **Chapter 3**. Here, a set of micron-sized H-ZSM-5 zeolites, containing different Si/Al ratio, is used. At mild reaction temperature similar coke compounds are generated and an increase in Brønsted acid site density enhances their formation rate. At elevated reaction temperatures more extended coke species form and their growth becomes more pronounced with higher Brønsted acid site density. Polarization dependent UV-Vis micro-spectroscopy indicates that the larger coke compounds preferably align within the zeolite straight pores, while smaller hydrocarbons homogeneously locate throughout the zeolite crystal. With confocal fluorescence microscopy, the use of different excitation wavelengths additionally allows to detect that larger hydrocarbons primarily locate near the crystal surface. It shows that both their formation as well as their migration towards the zeolite core is facilitated with increasing reaction temperature.

The catalytic properties of large micron-sized H-ZSM-5 crystals, during the MTO conversion, are investigated in **Chapter 4**. A fixed-bed reactor equipped with on-line gas-effluent GC analysis records the time-resolved activity and selectivity of the catalysts. Off-line GC-MS provides details on the chemical structure of the carbonaceous species retained within the catalytic crystals. The moderate coke formation that occurs at low reaction temperatures results in a slow progressing loss of activity. The coke deposits primarily consist of methyl-substituted mono-aromatics and the catalyst is active for a long time during which mainly C2 and C3 olefins are formed. With increasing reaction temperature, the enhanced coke formation rate induces a strong decline in conversion activity. During this process, the catalyst selectivity changes and C1 and C2 products form at the expense of larger C3 and C5 hydrocarbons. The micron-sized zeolites maintain a stable activity after 5 regeneration cycles.

Chapter 5 applies the micro-spectroscopic tools for the investigation of coke deposition during the aromatization process of paraffin and olefin hydrocarbons (LNA) over large H-ZSM-5 zeolites. Optical microphotograph image analysis shows how crystal color intensities and color change rates strongly depend on the reactant type and the related in-situ UV-Vis absorption measurements reflect these different coking trends. Fast coke formation occurs during olefin aromatization, whereas paraffin conversion induces minor carbonaceous deposition. Increasing chain length of linear reactants enhances the crystal darkening as more extended carbonaceous deposits are formed. However, methyl-branching of these starting products gives

opposite results generating coke species that are more confined in size. In-situ confocal fluorescence microscopy reveals that paraffinic hydrocarbons mainly convert near the zeolite surface area and methyl-branching of these alkanes facilitates their diffusion through the zeolite crystal. The conversion of linear olefins causes a non-fluorescent crystal edge, indicating the presence of a graphite-like external layer. Branched alkenes, on the contrary, do not form such non-fluorescent edge. These reactants form small fluorescent species that evenly spread throughout the zeolite crystal, while a front of larger coke compounds migrates towards the center of the zeolite.

The influence of a non-catalytic silicalite-1 shell covering the catalytically active H-ZSM-5 zeolite crystal, on the coke formation process is examined in **Chapter 6**. Optically active carbocationic oligomers, that form during the oligomerization of different styrene reactants, indicate the conversion ability of the acid core, a preferred alignment of the oligomers within the straight zeolite channels and a Brønsted acidity gradient within the zeolite composite. Limited carbonaceous deposition occurs within the external silicalite-1 layer and during both MTO and LNA conversion, this outer shell prevents the growth of extended coke species at the zeolite external surface. During MTO, the formation of carbonaceous compounds initiates at the center of the H-ZSM-5 zeolite core and expands towards the zeolite exterior. It is found that similar coke compounds are formed, regardless of the applied reaction temperature although the coke deposition occurs with a faster rate at more severe reaction conditions. Aromatization of linear and branched C5 paraffins causes negligible darkening of the zeolite composite. Fluorescent coke species are however detected throughout the H-ZSM-5 crystal. Olefin homologues cause a pronounced darkening of the zeolite composite. Methyl-branching of these reactants slows down the coke formation rate and produces more confined carbonaceous species. These compounds generate an intense fluorescent H-ZSM-5/silicalite-1 boundary that prevents the diffusion of fluorescent species towards the zeolite centre.

Chapter 7 describes the use of confocal fluorescence microscopy to study the coke formation on large micron-sized H-Beta zeolite crystals during the etherification of biomass-based alcohols with long linear alkenes. It indicates, in a space-resolved manner, that the physicochemical properties of both alcohol and alkene have a strong influence on the formation of byproducts within the zeolite crystal. Here, the hydrophobic/hydrophilic interplay between reactants and zeolites affects the location of the coke formation. An external zeolite surface area, having a higher content of framework aluminum, was found to be essential. This area is more hydrophilic compared to

the center of the H-Beta zeolite. Hydrophobic reactants, such as glycols and long alkenes, therefore have more difficulty to penetrate towards the crystal core and mainly interact near the zeolite outer surface. The more hydrophilic glycerol and shorter alkenes on the other hand also react with the active sites present within the center of the H-Beta crystal.

The combination of in-situ UV-Vis micro-spectroscopy and confocal fluorescence microscopy proved to be a valuable tool to probe the formation of carbonaceous deposits on individual zeolite crystals during various catalytic reactions. Characteristic UV-Vis absorption bands identify the chemical nature of the formed coke species, while their fluorescent properties allow following the migration of these compounds within the zeolite crystal. Based on the results presented in this PhD thesis some general conclusions can be drawn on coke formation processes in zeolite crystals.

1) The coke formation is influenced by the crystallographic architecture of the zeolite catalyst and this effect allows to detect inconsistencies in the zeolite crystallinity. Small coke compounds can migrate throughout the catalyst crystal. Intracrystalline boundaries cause the build-up of these coke deposits and larger carbonaceous species overall experience higher diffusion limitations. Introduction of a catalytically inactive shell around a catalytically active crystal prevents the growth of extended coke deposits at the zeolite external surface.

2) The reaction temperature strongly influences the nature and formation rate of the coke compounds. Mild reaction conditions generate coke deposits that are rather limited in size. With increasing reaction temperature their formation rate increases and larger carbonaceous species are formed. An increase in Brønsted acid site density further enhances this process. The larger coke deposits have a preferred alignment within the zeolite straight channels.

3) The coke growth depends on the chemical nature of the reactant molecules. Alkanes cause minor coke formation, while olefinic hydrocarbons produce a more pronounced coke deposition. Increasing reactant chain length results in larger carbonaceous species, whereas branched reactants generate coke compounds of more confined size. The physicochemical interplay between reactants and zeolite catalysts further affects the location of coke formation with consequences for the chemical conversion.

A particular strength of the analytical tools used in this work is their non-invasive nature. Different characterization techniques provide different pieces of information that, when combined, generate a more comprehensive picture of the studied system. It is therefore desirable that future work continues to combine analytical tools.

As these techniques have micrometer spatial resolution, the use of large model zeolite crystals allows to probe spatial heterogeneities at the individual catalyst particle level. The obtained findings can consequently be extrapolated to smaller zeolite catalysts applied in industry. However, the methods used have also restrictions in providing chemical information. Therefore, further development of improved analytical tools is valuable.

Resolution improvements direct towards super resolution microscopy. Some super resolution fluorescence microscopy methods apply advanced techniques that reconstruct an image with better resolution. Examples of this approach include for example stimulated or photoactivated microscopy (STED/PALM/STORM). Scanning Near-Field Optical Microscopy (SNOM) is another promising super resolution technique. Here, the detector is placed very close to the sample and this distance is smaller than the applied wavelength. The aperture is also smaller than the wavelength. This approach overcomes the Bragg diffraction limitation and allows a spatial resolution of ~ 20 nm. However, the chemical information provided by this optical technique remains limited. Therefore, extension towards other spectroscopical techniques is desired. This Scanning Near-Field (SN) technology can, for example be combined with the acquisition of spectral information using infrared spectroscopy. With this Scanning Near-Field Infrared Microscopy (SNIM), the vibrational fingerprint of the investigated sample can additionally be obtained. A related powerful vibrational technique is Surface Enhanced Raman Spectroscopy (SERS). This method enhances the otherwise weak Raman signal and has potential for single molecule detection. For spatially resolved measurements however, a combination of SERS and Atomic Force Microscopy (AFM) is required. In this approach, the AFM tip is coated with signal enhancing nanoparticles. Tip Enhanced Raman Spectroscopy (TERS) gives spatial information by scanning the sample surface, while the enhanced Raman signal provides chemical information of the surface species. Furthermore, besides spectroscopic techniques, recent advances in mass spectrometry indicate the ability of Laser Desorption Ionization Mass Spectrometry (LDI-MS) to detect the structure of large molecules, such as coke deposits, in a spatially resolved manner.

With an appropriate in-situ cell, many of the above mentioned characterization techniques could probably work under reaction conditions and provide detailed insights into deactivation phenomena that will hopefully lead to improved catalyst materials.

Chapter 8b

Samenvatting in het Nederlands

Chemicaliën worden vandaag de dag grotendeels verkregen uit op aardolie gebaseerde processen. Echter, de gelimiteerde oliereserves, de daaraan gekoppelde olieprijs en duurzaamheidsaspecten vragen om de ontwikkeling van nieuwe omzettingen waarbij chemicaliën geproduceerd worden met alternatieve grondstoffen. Zeolietkatalysatoren kunnen bij deze nieuwe transformaties een belangrijke rol spelen. Zeolieten zijn anorganische poreuze materialen die voornamelijk zijn opgebouwd uit silicium, aluminium en zuurstof. Het zijn sterke constructies met een goed gedefinieerde kristallijne structuur. Gedurende de chemische omzetting in een zeoliet kunnen echter, door toedoen van nevenreacties, koolstofhoudende bijproducten gevormd worden. Deze zogenaamde cokemoleculen bevinden zich in en rondom het zeolietkristal en kunnen de katalytische eigenschappen van de katalysator beïnvloeden. In een zeoliet wordt de katalytische omzetting verzorgd door zure plekken. Ongewenste cokemoleculen kunnen op deze plekken adsorberen en verhinderen daarmee een optimaal gebruik van de katalysator. Cokemoleculen kunnen ook uitgroeien tot grote componenten die de poriën van het zeolietkristal vullen. Dit heeft invloed op de katalytische omzetting, aangezien het blokkeren van de poriën verhindert dat reactanten en producten door het kristal diffunderen. Deze nadelige gevolgen van cokesvorming kunnen een belemmering zijn voor de toepassing van zeolieten op industriële schaal. Dit proefschrift bestudeert de vormingsprocessen van cokemoleculen met micro-spectroscopie, waarbij de ontwikkelingen in één individueel katalytisch kristal worden onderzocht op tijds- en plaatsafhankelijke wijze.

De omzetting van methanol naar olefine koolwaterstoffen (MTO) is een veelbelovende conversie waarbij alkenen verkregen kunnen worden uit alternatieve grondstoffen zoals biomassa, aardgas of kolen.

Hoofdstuk 2 onderzoekt de afzetting van de ongewenste koolstofhoudende bijproducten tijdens de MTO reactie. Twee zeolietkatalysatoren, met verschillende kristalopbouw worden daarbij bestudeerd, namelijk H-ZSM-5 en H-SAPO-34. Het bestuderen van deze twee zeolieten heeft als doel om de invloed van het kristalstructuur op de cokesvorming te verhelderen. In H-ZSM-5 begint de cokesvorming aan de randen van het zeolietkristal. Gedurende de

reactie verspreiden de ongewenste nevenproducten zich homogeen over het gehele katalysatordeeltje. De vorming van de coke-afzettingen hangt sterk af van de reactietemperatuur. Bij lage temperaturen veroorzaken de koolstofhoudende moleculen een lichte bruinkleuring van het zeolietkristal. Deze cokecomponenten bestaan voornamelijk uit mono-aromaten. Verhoging van de reactietemperatuur versnelt het cokesvormingsproces en de zeolieten worden dan donkerder van kleur. Deze coke-afzettingen bevatten grotere poly-aromaten alsook grafeen-achtige moleculen die zich aan het externe kristaloppervlak bevinden. In H-SAPO-34 ontstaan, bij lage reactietemperaturen, de mono-aromaten met name rondom de randen van de katalytische kristallen. Bij hogere reactietemperaturen neemt de groei van deze cokemoleculen geleidelijk toe waarbij ook grotere cokecomponenten vormen. De grootte van deze koolwaterstoffen blijft echter beperkt en de stoffen verblijven voornamelijk binnenin het zeolietkristal. Al deze verschillen zijn illustratief voor de invloed van de kristalstructuur op het cokesvormingsproces. Tijds- en plaatsafhankelijke confocale fluorescentie microscopie visualiseert hoe de fluorescente coke-afzettingen binnenin de zeolietkristallen migreren. In H-ZSM-5 ondervinden de grotere moleculen beperkingen in diffusie. Deze beperkingen zijn voornamelijk aanwezig bij de interne kristallijne grensvlakken. In H-SAPO-34 bevinden de fluorescente bijproducten zich hoofdzakelijk rondom de kristalrand. De grotere cokemoleculen verhinderen daarbij dat de kern van het zeoliet optimaal wordt gebruikt bij de katalytische omzetting.

Hoofdstuk 3 onderzoekt, tijdens de MTO omzetting, de invloed van de Brønsted zure dichtheid op de cokesvormingsprocessen in H-ZSM-5. Bij lage reactietemperaturen bestaan de cokemoleculen uit soortgelijke componenten en een toename in zuurdichtheid versnelt de vorming van deze koolstofhoudende bijproducten. Hogere reactietemperaturen resulteren in de vorming van grotere cokeproducten en het ontstaan ervan neemt toe naarmate de zuurdichtheid toeneemt. Polarisatie-afhankelijke microspectroscopie onthult hoe de grotere cokeproducten hoofdzakelijk in de rechte poriën van de zeolietkristallen vormen. De kleinere koolstofhoudende nevenproducten verdelen zich daarentegen homogeen over het kristal. De toepassing van verschillende excitatiegolflengtes in confocale fluorescentie microscopie maakt het mogelijk om coke-afzettingen, verschillend in grootte, te differentiëren in één zeolietdeeltje. Grotere bijproducten worden dan meer aan de rand van het zeoliet gedetecteerd.

In hoofdstuk 2 en 3 is er onderzoek gedaan op zeer grote zeolietkristallen. De forse afmetingen van deze katalysatoren zijn noodzakelijk om beperkingen in ruimtelijke resolutie, opgelegd door de diffractielimiet van de gebruikte

micro-spectroscopie technieken, te overbruggen. De zeolieten die op industriële schaal worden toegepast zijn echter kleiner, met afmetingen rondom de 0.5-3 μm en deze worden vooral onderzocht met enigszins 'gevestigde' bulk analysemethoden. In **hoofdstuk 4** worden daarom de katalytische eigenschappen van de grote modelkatalysatoren onderzocht met bulk analysemethoden, waarbij resultaten verkregen worden uit een grote hoeveelheid kristallen. De milde cokesvorming, die optreedt bij lage reactietemperaturen, vertaalt zich in een langzame constante afname van katalytische activiteit. De grote kristallen blijven zeer lang actief en gedurende dit proces worden voornamelijk C2 en C3 olefines geproduceerd. Een verhoging van de reactietemperatuur veroorzaakt een versnelde vorming van grote ongewenste bijproducten. Dit proces leidt ertoe dat er een verandering optreedt in de katalytische selectiviteit met als gevolg dat C1 en C2 producten worden gevormd ten koste van C3 en C5 koolwaterstoffen. De activiteit van de grote zeolietkatalysatoren blijft na 5 regeneraties stabiel.

De omzetting van olefine en paraffine koolwaterstoffen in aromatische materie (LNA) is belangrijk, omdat deze eindproducten een economische meerwaarde hebben. Dit proces is onderworpen aan vele studies waarbij vooral de cokesvorming tijdens de LNA omzetting een groot uitdaging vormt. **Hoofdstuk 5** past tijds- en plaatsafhankelijke micro-spectroscopie toe tijdens de aromatisatie van olefine en paraffine koolwaterstoffen in H-ZSM-5 katalytische kristallen. Optische beeld analyse illustreert dat de cokesvorming sterk afhangt van de gebruikte reactant. Aromatisatie van olefines genereert zeer veel koolstofhoudende bijproducten, terwijl de omzetting van paraffines beduidend minder donkere kristallen oplevert. Grotere lineaire reactanten vormen meer en grotere cokecomponenten. Vertakking van deze beginproducten geeft echter cokemoleculen van soortgelijke grootte. Confocale fluorescentie metingen tonen aan dat paraffine koolwaterstoffen voornamelijk aan de zeolietranden reageren. Vertakking van deze alkanen vergemakkelijkt het diffusieproces richting het midden van het kristal. Lineaire olefines veroorzaken een niet-fluorescerende kristalrand, wat aangeeft dat grote grafeen-achtige cokemoleculen aan het externe oppervlak van de katalysator groeien. Deze niet-fluorescente rand is niet waargenomen bij de omzetting van vertakte olefines.

Tot dusver wijzen de resultaten op het ontstaan van grote cokemoleculen rondom de externe randen van de zeolietkristallen. De invoering van een niet katalytische externe laag, rondom de actieve katalysator, kan dergelijke cokesvorming tegengaan. In **hoofdstuk 6** wordt onderzocht wat de invloed van een katalytisch inactieve silicaliet-1 schil, rondom het actieve H-ZSM-5 zeoliet is. De eigenschappen van het kristal worden bestudeerd

door middel van optisch actieve carbocationen die bij de oligomerisatie van styreenmoleculen gevormd worden. Verschillende styreensubstituenten laten daarbij zien dat de reactanten in staat zijn om door de externe schil heen te diffunderen en, eenmaal in de zure H-ZSM-5 kern, om te vormen. De ontstane oligomeren vertonen daarbij een voorkeursoriëntatie met de rechte kristalporiën en tonen een zuurgradiënt in het kristal aan. Tijdens de MTO en LNA omzettingen wordt amper cokesvorming binnenin de silicaliet-1 schil gedetecteerd en het omhulsel verhindert eveneens de vorming van grote cokemoleculen rondom de kristalranden. De ongewenste bijproducten zelf hebben eigenschappen die grote gelijkens vertonen met cokemoleculen die gevormd worden in een zeoliet zonder externe schil. Echter, de vorming van de koolwaterstoffen begint in deze zeolietcomposities in het midden van het kristal en groeit, tijdens reactie, richting de buitenkant ervan. Verder kan opgemerkt worden dat de reactietemperatuur een gering effect heeft op de chemische eigenschappen van de cokeneerslag en dat een verhoging van de temperatuur met name resulteert in een versnelde cokesvorming. Aromatisatie van lineaire en vertakte paraffine koolwaterstoffen geeft matige verkleuring van het zeoliet. Confocale fluorescentie microscopie illustreert dat, ondanks de afwezigheid van zichtbare cokecomponenten, fluorescente cokemoleculen zich binnenin de gehele zure H-ZSM-5 kern bevinden. De omzetting van alkenen maakt de katalysator donkerder met een sterk fluorescent grensvlak tussen de zure H-ZSM-5 kern en de inactieve silicaliet-1 schil. Deze ophoping van cokemoleculen verhindert daarbij dat de kern van het zeoliet wordt bereikt.

Confocale fluorescentie microscopie wordt in **hoofdstuk 7** toegepast tijdens de etherificatie van op biomassa gebaseerde alcoholen met lange alkenen. De resultaten laten op plaatsafhankelijke wijze zien dat de fysisch-chemische eigenschappen van zowel de alcoholen als alkenen grote invloed hebben op de vorming van cokeproducten in H-Beta zeolieten. Met name het effect van de hydrofobe/hydrofiele relatie tussen reactanten en kristal is daarbij van belang. Een grotere hoeveelheid aluminium aan de randen van de katalysator resulteert in een hoger hydrofiel karakter vergeleken met de zeolietkern. Hydrofobe reactanten, zoals glycolen en lange alkenen, hebben daarom moeite om door deze laag heen te diffunderen en reageren voornamelijk aan de zeolietrand. Hydrofiele glycerolen en kortere alkenen kunnen echter wel het midden van het zeolietkristal bereiken waar vervolgens omzetting plaatsvindt.

De combinatie van UV-Vis absorptie micro-spectroscopie en confocale fluorescentie microscopie is een nuttig instrument gebleken voor het bestuderen van cokesvorming in zeolieten tijdens verschillende chemische omzettingen. Op basis van de resultaten die beschreven staan in dit proefschrift kunnen enkele algemene conclusies worden getrokken:

1) De cokesvorming wordt beïnvloed door de kristallijne structuur van het zeoliet. Kleine cokemoleculen kunnen door het gehele kristal diffunderen. Bij intra-kristallijne grensvlakken hopen deze cokeproducten zich op en de grotere koolwaterstoffen hebben meer moeite om door een kristal te migreren. Een katalytisch inactieve schil voorkomt de groei van grote cokemoleculen aan het externe kristaloppervlak.

2) De grootte van de cokemoleculen en hun vormingssnelheid nemen toe naarmate de temperatuur toeneemt. Dit proces wordt verder versterkt door een toename in Brønsted zure dichtheid van het zeolietkristal. Grote cokemoleculen groeien voornamelijk in de rechte zeolietporiën.

3) De groei van de coke-afzettingen hangt sterk af van de chemische eigenschappen van de reactanten. Alkenen produceren meer cokesvorming dan alkanen. Grotere lineaire koolwaterstoffen genereren grotere cokeproducten ten opzichte van vertakte reactanten. De fysisch-chemische relatie tussen reactanten en zeolietkatalysator beïnvloedt de lokatie van de coke-afzetting met gevolgen voor de chemische omzetting.

Verschiedende analysetechnieken geven verschillende soorten informatie die, eenmaal gebundeld, een beter beeld opleveren van het bestudeerde systeem. Het is daarom wenselijk dat toekomstig onderzoek doorgaat met het combineren van meerdere analysemethoden.

De gebruikte micro-spectroscopie technieken hebben een ruimtelijke resolutie van enkele micrometers. Het gebruik van grote modelzeolieten maakt het mogelijk om ruimtelijke verschillen in één katalysatorkristal te detecteren. De uitkomsten ervan kunnen vertaald worden naar zeolieten met kleinere dimensies die op industriële schaal worden toegepast. Echter, deze analysemethoden hebben ook beperkingen in de chemische informatie die ze verschaffen.

Verbeteringen in resolutie leiden richting superresolutie microscopie. Een voorbeeld van een dergelijke methode is de zogenaamde Near-Field technologie (SN). Scanning Near-Field Optische Microscopie (SNOM) overbrugt de Bragg diffractielimiet en kan een resolutie van ~ 20 nm halen. Deze technologie kan ook gecombineerd worden met methoden die een beter chemisch oplossend vermogen hebben, zoals Scanning Near-Field Infrarood Microscopie (SNIM). De daaraan gerelateerde Raman

spectroscopie heeft, in de vorm van Tip Enhanced Raman Spectroscopie (TERS), ook potentie. Voor niet-spectroscopie gerelateerde technieken zijn de recente ontwikkelingen in massaspectrometrie belangrijk. Laser Desorptie Ionizatie Massaspectrometrie (LDI-MS) kan bijvoorbeeld de structuur van een molecuul met ruimtelijke resolutie verhelderen.

Met geschikte reactie-cellen kunnen vele van de bovengenoemde analysemethoden een nieuwe kijk geven op cokesvormingsprocessen in katalytische systemen, wat hopelijk zal leiden tot betere katalysatoren.

List of Publications

Catalytic Performance of Micron-sized H-ZSM-5 Zeolite Crystals during the Methanol-to-Olefin Conversion: Bridging the Gap between Single Particle Examination and Bulk Catalyst Analysis

D. Mores, S. Teketel, U. Olsbye, B.M. Weckhuysen; *Catal. Lett.* **2011**, submitted.

Core-Shell H-ZSM-5/Silicalite-1 Composites: Brønsted Acidity and Catalyst Deactivation at the Individual Particle Level

D. Mores, E. Stavitski, S.P. Verkleij, A. Lombard, A. Cabiac, L. Rouleau, J. Patarin, A. Simon-Masseron, B.M. Weckhuysen; *Phys. Chem. Chem. Phys.* **2011**, in press (doi: 10.1039/c1cp21324e).

Spatial and Temporal Mapping of Coke Formation during Paraffin and Olefin Aromatization in Individual H-ZSM-5 Crystals

Y-M. Chung, D. Mores, B.M. Weckhuysen; *Appl. Catal. A: Gen.* **2011**, in press (doi:10.1016/j.apcata.2011.06.030).

Porosity, Acidity and Reactivity of Dealuminated Zeolite ZSM-5 at the Single Particle Level: Influence of the Zeolite Architecture

L.R. Aramburo, L. Karwacki, P. Cubillas, S. Asahina, D.A.M. De Winter, M.R. Drury, I.L.C. Buurmans, E. Stavitski, D. Mores, M. Daturi, P. Bazin, P. Dumas, F. Thibault-Starzyk, N. Kahn, J.A. Post, S.R. Bare, M.W. Anderson, O. Terasaki, B.M. Weckhuysen; *Chem. Eur. J.* **2011**, accepted

Template Removal Process within Individual Micron-sized SAPO-34 Crystals: Effect of Gas Atmosphere and Crystal Size

Q. Qian, D. Mores, J. Kornatowski, B.M. Weckhuysen; *Microporous. Mesoporous. Mater.* **2011**, 246, 28-35.

Experimental and Theoretical IR Study of Methanol and Ethanol Conversion over H-SAPO-34

K. Hemelsoet, A. Ghysels, D. Mores, K. De Wispelaere, V. Van Speybroeck, B.M. Weckhuysen, M. Waroquier; *Catal. Today* **2011**, in press (doi: 10.1016/j.cattod.1011.05.040).

Coke Formation during the Methanol-to-Olefin Conversion: In-Situ Micro-spectroscopy on Individual H-ZSM-5 Crystals with Different Brønsted Acidity

D. Mores, J. Kornatowski, U. Olsbye, B.M. Weckhuysen; *Chem. Eur. J.* **2011**, 17, 2874-2884.

Chemical Imaging of Catalyst Deactivation during the Conversion of Renewables at the Single Particle Level: Etherification of Biomass-Based Polyols with Alkenes over H-Beta Zeolites

A.N. Parvulescu, D. Mores, E. Stavitski, C.M. Teodorescu, P.C.A. Bruijninx, R.J.M. Klein Gebbink, B.M. Weckhuysen; *J. Am. Chem. Soc.* **2010**, 132, 10429-10439.

Mesopore formation in Zeolite H-SSZ-13 by desilication with NaOH

L. Sommer, D. Mores, S. Svelle, M. Stöcker, B.M. Weckhuysen, U. Olsbye; *Microporous. Mesoporous. Mater.* **2010**, 132, 384-394.

Supramolecular Dendriphores: Anionic Organometallic Phosphors Embedded in Polycationic Dendritic Species

A.R. McDonald, D.Mores, C. De Mello Donega, C. A. Van Walree, R.J.M. Klein Gebbink, M. Lutz, A.L. Spek, A. Meijerink, G.P.M. Van Klink, G. Van Koten; *Organometallics* **2009**, 28, 1082-1092.

Space- and Time-Resolved In-Situ Spectroscopy on the Coke Formation in Molecular Sieves: Methanol-to-Olefin Conversion over H-ZSM-5 and H-SAPO-34

D. Mores, E. Stavitski, M.H.F. Kox, J. Kornatowski, U. Olsbye, B.M. Weckhuysen; *Chem. Eur. J.* **2008**, 14, 11320-11327.

Oral Presentations

In-Situ Micro-Spectroscopy during the Methanol-to-Olefin Conversion: Coke Formation on H-ZSM-5 Zeolite Crystals

12th NCCC, Noordwijkerhout, The Netherlands, 2-4 March **2011**

Coke Formation during the Methanol-to-Olefin Conversion: An In-Situ Micro-Spectroscopy Study on Individual H-ZSM-5 Crystals with Different Brønsted Acidity

12th Workshop of the IRTG "Structural analysis Spectroscopy and Reactivity of Porous materials" Utrecht, The Netherlands, 8-10 November **2010**

Chemical Imaging of Catalytic Reactions in Zeolites with CARS Microscopy

ACS 240th National Meeting, Boston, USA, 22-27 August **2010**

Coke Formation during the MTO Reaction, a Space- and Time- Resolved In-situ Spectroscopy Study

11th International Symposium on Catalyst Deactivation, Delft, The Netherlands, 25-28 October **2009**

Coke Formation during the Methanol-to-Olefin Conversion

NRSC-C Meeting, Utrecht, The Netherlands, 12 November **2008**

Space- and Time-resolved In-situ Spectroscopy on the Coke Formation on H-SAPO-34 and H-ZSM-5 during the Methanol-to-Olefin Conversion

Meeting of the NVvM, "Microscopy of catalyst and nanoparticles", Lunteren, The Netherlands, 10-11 November 2008

Poster Presentations

In-Situ Micro-Spectroscopy Study on the Coke Formation during the Methanol-to-Olefin Conversion on Individual H-ZSM-5 Crystals

ACS 240th National Meeting, Boston, USA, 22-27 August 2010

In-situ Micro-Spectroscopy Study on the Coke Formation during the Methanol-to-Olefin Conversion on Individual H-ZSM-5 crystals with Different Acidity

IZC-IMMS 2010, Sorrento, Italy, 4-9 July 2010

Coke Formation during the Methanol-to-Olefin Conversion - In-Situ Spectroscopy on Single H-ZSM-5 and H-SAPO-34 Crystals

COST Chemistry D36 3rd Workshop, Benahavis, Spain, 21-24 October 2009

Coke Formation during the Methanol-to-Olefin Conversion - In-Situ Spectroscopy on Single H-ZSM-5 and H-SAPO-34 Crystals

Operando III, Rostock-Warnemünde, Germany, 19-23 April 2009

Coke Formation during the Methanol-to-Olefin Conversion - In-Situ Spectroscopy on Single H-ZSM-5 and H-SAPO-34 Crystals

10th NCCC, Noordwijkerhout, The Netherlands, 2-4 March 2009

Acknowledgements

Tijdens mijn dagelijkse fietstocht richting universiteitswijk De Uithof voelde de ‘Weg tot de Wetenschap’ vaak lang en eenzaam aan. Echter, aangekomen bij het meest gelezen onderdeel van mijn proefschrift, besef ik dat niets minder waar is. Ik wil iedereen die de afgelopen jaren heeft bijgedragen aan de totstandkoming van dit werk hartelijk danken en enkele personen in het bijzonder:

Ik ben in de eerste plaats mijn promotor Prof. Weckhuysen zeer erkentelijk. Bert, de gelegenheid om onder jouw begeleiding te promoveren was voor mij een buitenkans. Het mogen deelnemen aan uitdagende projecten met vooruitstrevende apparatuur is niet iedereen gegeven en heb ik persoonlijk als een groot voorrecht ervaren. Je steun om mijn werk internationaal te mogen presenteren heb ik bijzonder geapprecieerd. Maar bovenal hebben de afgelopen jaren een zeer grote bijdrage geleverd aan mijn persoonlijke en wetenschappelijke ontplooiing. Wat mij altijd zal bijblijven is hoe jouw interesse en creatieve inzicht als katalysator hebben gefungeerd voor dit werk en mij hebben gemotiveerd. Jouw energie, vertrouwen en geduld zijn voor mijn ontwikkeling erg belangrijk geweest. Bert, ontzettend bedankt!

Een bijzonder dankjewel gaat naar Dymph en Monique. Dames, ik heb de afgelopen jaren moeite gehad om mij strikt aan de “secretariële openingstijden” te houden. Desondanks kon ik iedere keer weer met een lach jullie kantoor verlaten. Bedankt voor de fijne samenwerking en alle hulp bij het administratieve geregel.

Beste Ad^M, Vincent^K, Marian^{VH}, Ad^E en Rien^{VZ}: Ik heb met jullie gewerkt, gelachen, geklaagd, gerookt, gebarbecued, geverhuisd, genoten en veel gebruik gemaakt van jullie kennis en hulp. Dank voor jullie inzet!

I am grateful to my co-workers from Norway: Dr. Linn Sommer, Shewangizaw Teketel and Prof. Unni Olsbye. Working together with you has been very educative and most enjoyable. Many thanks for all the nice collaborations.

I want to thank Dr. Young-Min Chung for the pleasant collaboration. I appreciated our fruitful and versatile discussions very much.

Beste Dr. Karen Hemelsoet, ik vond het fijn om met jouw hulp te mogen proeven aan de wondere wereld van de theoretische chemie. Onze samenwerking was weliswaar kort maar zeer intensief en bovenal plezierig. Ik wens jou het allerbeste met je toekomstige onderzoek.

Dr. Eli Stavitski, during these years we experienced that both life and science can be quite a rollercoaster. This thesis would have been quite different without your contribution. Thanks for everything Yankee!

Ik heb vele prettige uren mogen doorbrengen met Dr. Arjan Mank, Dr. Tom Visser en Fouad Soulimani (Dr. in spé). De gezonde dosis humor en de nodige leermomenten waren bijzonder te waarderen. De niet-spectroscopie gerelateerde lessen zullen mij wellicht nog het meest bijblijven.

I would like to thank Dr. Andrei Parvulscu and Dr. Pieter Bruijninx for the numerous hours we spent together. I took pleasure in working with you on biomass-based conversions. They were a welcome distraction from my daily work and I learned a lot!

Beste Prof. Krijn De Jong en Dr. Harry Bitter: Ondergrondse CO₂ opslag, begeleiding van talentvolle studenten en worteltjes...zomaar een selectie van onze wetenschappelijke en minder-wetenschappelijke gesprekken. Mede hierdoor heeft mijn verblijf in Utrecht verder gereikt dan "slechts" het microscopie lab. Mijn dank is groot.

A special experience during my PhD was the establishment of the NIOK PhD Platform (NPP). Dear Dr. Dirk Renckens and Dr. Sergio Pacheco, during these years we became more than just co-founders and gifted board-members of the NPP. Our moments together were creative, constructive and erg gezellig!

Ik wil Dr. Paul Pijzel en Dr. Kees van Walree bedanken voor hun assistentie tijdens mijn avontuurlijke onderwijstaken. Het vergaren van chemische vaardigheden is niet vanzelfsprekend. Het anderen bijbrengen is een kunst op zich en vereist naast moed ook veel geduld. Dank voor al jullie hulp daarbij, ik ben er een beter docent van geworden.

De afgelopen jaren heb ik enkele studenten tijdens hun bachelor- of master-traject mogen begeleiden: Bas Reijers, Pieter Biewenga, Sander de Brouwer, Arno Veldhorst, Hendrik v/d Bij, Didier Cornelissen, en Suzanne Verkleij. Het leerproces was in alle gevallen een zeer fijn tweerichtingsverkeer. Heel veel succes met het afronden van jullie studie en wat erop volgen gaat.

I want to thank Sauro Sassari and Sara Davis for all the pleasant moments during their stay in Utrecht.

There is no micro-spectroscopy without the Nanorangers!

Dear Marianne, Lukasz, Inge, Qingyun, Clare, Luis, Javi, Evelien, Zoran, Hendrik, Jan Philipp and Sophie, many thanks to all of you! I enjoyed the many hours we spent together in the lab, they were in many ways most rewarding.

Inge, met het afronden van onze PhD studie komt er helaas ook een eind aan onze memorabele woensdag middag uit-je-dip-tip. Ik ga ze missen! We hebben de afgelopen jaren veel meegemaakt samen. Het was bijzonder fijn om al die tijd een maatje te hebben waar ik, ook buiten de studie om, op kon rekenen. Ik wil je daarvoor ontzettend bedanken.

Qingyun, my Chinese dragon! Together we experienced how a PhD-path has many similarities with running a marathon. It requires endurance, commitment and an athletic mate to keep the pace. You were a great lab-pal!

Clare, my Great Britain! Our teamwork required some activation energy but, like with a proper catalyst, it all quickly improved. You are a gifted borrel-lady and I wish you all the best with your PhD, cake baking and health!

My procrastination-skills expended enormously throughout these years and I am grateful to all colleagues for helping me achieving this elusive goal. Some of them however need a special note: My roommates: Rob, Peter^N, Evelien, Marianne and my open-office buddies: Upakul, Ilona, Annelie, Luis, Piter, Bart, Hirsa, Peter^H and Dilek. Thanks for all the nice moments and good luck with your research. Carlo, besides joking whether or not the Italian border actually covers the other side of the river Po, I must say that I am proud and more than happy with you, as my Italian successor in the group. Buona fortuna ragazzo!

Beste vrienden, vriendinnen en volleybal-maatjes. Jullie wil ik allemaal bijzonder bedanken voor alle gezellige momenten samen de afgelopen jaren. Dat er nog vele mogen volgen!

L'ultimo paragrafo di questa tesi lo dedico ai miei cari.

Papa è mamma, grazie di tutto cuore per il vostro appoggio ed amore. Anna, Andrea, Marco, Filippo, Giulia, Giacomo, Maria, Mores-junior, Elisabetta, Paolo, Raffaele, Noemi, Santin-junior, Marta, Emmanuele, Miriam, Giovanni, Daniele, Francesco, Maddalena e Chiara... vi voglio bene!

Davide

About the Author

Davide Mores was born on the 25th of April 1982 in Pordenone, Italy. After graduating from secondary school (O.S.G. Het Baken (Almere) and C.S.G. Willem de Zwijger (Schoonhoven)), he started his undergraduate studies in Chemistry at Utrecht University in 2001. He obtained his bachelor degree in 2004 after writing a thesis on colloidal chemistry under the supervision of Prof. A.P. Philipse at the Van 't Hoff Laboratory for Physical Colloidal Chemistry. After that, he began the master Chemistry & Physics at Utrecht University. There he specialized in organic chemistry and homogeneous catalysis. He wrote his master thesis on dendritic supported OLEDs under the supervision of Dr. A.R. McDonald, Prof. R.J.M. Klein Gebbink and Prof. G. Van Koten. He spent 6 months at Quest International (ICI) where he developed, during an internship, novel taste active molecules under the supervision of Dr. C. Winkel. In 2007 he obtained the master degree and in that same year he started his PhD research project at the Inorganic Chemistry and Catalysis group at Utrecht University under the supervision of Prof. B.M. Weckhuysen. The thereby obtained results are described in this thesis and were presented at several (inter)national conferences. At the Operando 2009 conference, his poster presentation was awarded with the Physical Chemistry Chemical Physics (PCCP) Poster Prize. Throughout this academic period he was active in several extracurricular activities, such as representative at the co-administration council of the Bèta Science Faculty (2002-2009), chairman of the chemistry student association U.S.S. Proton (2004-2005) and co-founder plus secretary of the NIOK PhD Platform (2008-2010). Davide Mores currently works as international trainee for Linde Gas.